



The University of
Nottingham

UNITED KINGDOM • CHINA • MALAYSIA

Towards in-vivo Grown

Bioelectronics: Utilising Bipolar

Electrochemistry

Andie Jane Robinson, BEng

Thesis submitted to the University of Nottingham for the degree of Doctor
of Philosophy

October 2021

"The only true wisdom is in knowing you know nothing"

Socrates

"Learning never exhausts the mind"

Leonardo Da Vinci

Abstract

Bipolar electrochemistry brings exciting possibilities to be able to grow electronics in situ within biological systems, thus creating electronics that seamlessly merge with biology and are on a similar scale to cellular components. This could allow the development of novel applications to tackle some of the world's greatest health burdens, such as cancer. Therefore, the aim of this thesis is to develop bioelectronic systems, utilising bipolar electrochemistry, for possible applications in cancer treatment.

State of the art bioelectronic treatment of cancer includes tumour treating fields: a novel therapy whereby high frequency electric fields are used to halt the growth of tumours. Electric fields are currently applied to target sites using external electrodes, hence the development of in-situ grown electrodes for this application could improve therapy outcomes and lower timeframes and costs. Working towards this application, this thesis has three main objectives: the development of wirelessly in situ grown microwires (MWs) in the presence of cells, the development of bipolar electrodes (BPEs) suitable for use in biological systems, and the development of a method to characterise nano-BPEs in order to better understand bipolar electrochemistry in the presence of biological systems.

Ag MWs are grown using a wireless, bipolar electrochemical method. We build on previous literature by optimising the electrode setup required to grow Ag MWs. Alternating current (AC) is then used to grow Ag MWs for the first time and proofs of concept for growing MWs in the presence of 3D cell cultures and from the addition of a metal salt are presented.

Nano-BPEs are developed using conductive metallic and polymeric nanoparticles. Bipolar electrochemical reactions are confirmed at the nanoscale BPEs using dynamic light scattering (DLS) and transmission electron microscopy (TEM) with energy dispersive X-ray spectroscopy (EDS). These BPEs are then introduced to a tumour treating fields (TTFs) research device and show promise in potentiating the cytotoxic effects of TTFs.

Finally, an impedimetric method for the characterisation of nano-BPEs is developed. This method is then used to characterise nano-BPEs in the presence of biological systems. Au Nano-BPEs are shown to be sensed when placed intracellularly, therefore showing great promise for applications in bioelectronics.

Overall, these developments will help advance the field of wireless bioelectronics and aid in the understanding of how bipolar electrochemistry performs at the nanoscale. This will have broad reaching impact in bioelectronic medicine, biosensing and nanoelectronics.

List of publications

Robinson, A. J. *et al.* Impedimetric Characterization of Bioelectronic Nano-antennae. *ACS Omega* (2021). (*in press*).

Robinson, A. J. *et al.* Toward Hijacking Bioelectricity in Cancer to Develop New Bioelectronic Medicine. *Advanced Therapeutics* **4**, (2021).

Gibney, S. *et al.* Toward nanobioelectronic medicine: Unlocking new applications using nanotechnology. *Wiley Interdiscip. Rev. Nanomedicine Nanobiotechnology* (2021).

Sanjuan-Alberte, P. *et al.* Wireless Nanobioelectronics for Electrical Intracellular Sensing. *ACS Appl. Nano Mater.* **2**, 6397–6408 (2019). (Published under A. J. Shaw)

Sanjuan-Alberte, P. *et al.* Remotely Controlled in Situ Growth of Silver Microwires Forming Bioelectronic Interfaces. *ACS Appl. Mater. Interfaces* **11**, 8928–8936 (2019). (Published under A. J. Shaw)

Acknowledgements

I want to start by acknowledging the only reason I managed to complete my PhD without going insane; my shoulder to cry on, my happy place to come home to, the only one able to reduce my stress levels: Jet, my dog! Of course, I must also thank my wonderful husband who was also enormously supportive throughout this extremely difficult time in our lives, all whilst living apart. Thank you for always believing in me and thank you for always being interested in my work (despite mistakenly believing I was developing cancer fighting robots).

Secondly, I want to acknowledge the rest of my family who have supported me throughout my entire academic career. Thank you to my mum, who was always at the end of the phone. Thank you to my dad, for being my intellectual role model, allowing me to push myself harder, as I strive to impress him. As I know he was unable to fulfil his ambition of pursuing a PhD, I hope this thesis is an achievement that he too can be very proud of.

Thank you to Dr Frankie Rawson for being the perfect supervisor, and never taking anything too seriously! Thank you for all the time, effort and knowledge you have provided me with to complete this thesis. Thank you for never giving up on me – even though I was ready to give up a number of times. I really hope I have the pleasure of working with you again in the future; I know the group

have done and will continue to do amazing things under your supervision. Thank you to my secondary supervisors Dr Ruman Rahman and Prof Richard Hague for your support and assistance in your specialist areas. Thank you to the incredible staff at the University of Nottingham, particularly Teresa and Ann, for your help and kindness.

Thank you to my fellow PhD students, who were great sounding boards and support networks. Thank you, Paola, Akhil, Dom, Mechelle, Jacqui, and the rest of the Rawson group for all of your help and contributions towards my work and for being the most amazing research colleagues.

Thank you to my best friend Abigail, who made me a PhD cake to celebrate securing a place on my CDT and has continued to support me throughout my PhD experience. Thank you to Nicole and Dean who have always been just moments away for some well needed R&R, or a glass (or three) of wine.

Last but by no means least, thank you to Ivy Leia, my beautiful daughter. Although a global pandemic meant I was unable to complete my PhD before your arrival, your presence allowed me to get over the last hurdle (despite the lack of sleep!). You have made me stronger, happier and complete. You are my greatest achievement, although I hope to say successfully defending my thesis will come a close second!

Table of Contents

Abstract	i
List of publications	iii
Acknowledgements	v
Table of Contents	vii
List of Figures	xiii
List of Tables	xxii
Abbreviations.....	xxiii
Chapter 1. Introduction.....	1
1.1. Literature Review.....	1
1.1.1. <i>Bioelectronic Medicine</i>	1
1.1.2. <i>Manufacturing Bioelectronics</i>	4
1.1.3. <i>Bioelectronics in Cancer</i>	7
1.2. Theoretical Framework.....	15
1.2.1. <i>3D Printing/ Additive Manufacturing</i>	15
1.2.2. <i>Electrochemistry</i> ^{87,88}	18

1.2.3. <i>Bipolar Electrochemistry</i>	21
1.2.4. <i>Electrochemical Impedance Spectroscopy</i>	27
1.2.5. <i>Other Characterisation Methods</i>	32
1.3. Aim and Objectives	39
1.4. Summary of Work	41
1.5. Contributions	43
Chapter 2. Microwire growth in the presence of cells.....	45
2.1. Introduction	47
2.2. Methods.....	51
2.2.1. <i>Electrode manufacture</i>	51
2.2.2. <i>3D Printing characterisation</i>	53
2.2.3. <i>Electrochemical wire growth</i>	54
2.2.4. <i>Cell culture – monolayers and 3D cell cultures</i>	55
2.3. Results and Discussion	57
2.3.1. <i>3D printing optimisation and characterisation</i>	59

2.3.2.	<i>Harnessing BPE geometry</i>	62
2.3.3.	<i>Can wire growth be controlled using geometries/orientation of BPEs?</i>	66
2.3.4.	<i>Satellite BPEs</i>	68
2.3.5.	<i>AC MW growth</i>	70
2.3.6.	<i>Developing 3D proof of concept</i>	73
2.3.7.	<i>Microwire growth from a metal salt</i>	77
2.4.	Summary and Conclusions.....	79
Chapter 3.	Development of Nano Bipolar Electrodes	83
3.1.	Introduction	85
3.2.	Materials and Methods	89
3.2.1.	<i>NP Synthesis and Characterisation</i>	89
3.2.2.	<i>In Vitro Bipolar Electrochemistry</i>	93
3.3.	Results and Discussion.....	95
3.3.1.	<i>NP Synthesis Optimisation</i>	95
3.3.2.	<i>NP Characterisation</i>	97

3.3.3.	<i>Bipolar Electrochemical Deposition on NP BPEs</i>	105
3.3.4.	<i>Application in Cancer Treatment</i>	115
3.4.	Summary and Conclusions	117
Chapter 4.	Impedimetric Characterisation of Nano-Bipolar Electrodes	
	119	
4.1.	Introduction	121
4.2.	Methods	129
4.2.1.	<i>Electrode Manufacture</i>	129
4.2.2.	<i>EIS Measurements</i>	130
4.2.3.	<i>Surface Functionalization of Gold Nanoparticles:</i>	131
4.2.4.	<i>Cell Culture and Cell Experiments</i>	131
4.3.	Results and Discussion	135
4.3.1.	<i>Theoretical Framework</i>	135
4.3.2.	<i>Nano BPE systems</i>	137
4.3.3.	<i>Living Cells with Nano BPEs</i>	145
4.4.	Summary and Conclusions	159

Chapter 5. Conclusions and Future Work.....	161
5.1. Final Discussion and Conclusions	161
5.2. Future work	171
5.2.1. <i>In Vivo Wire growth proof of concept.....</i>	<i>171</i>
5.2.2. <i>In Vivo bipolar electrochemistry proof of concept.....</i>	<i>178</i>
5.2.3. <i>Electric Field Enhancement for Tumour Treating Fields (TTFs)</i>	<i>184</i>
5.2.4. <i>Impedimetric Characterisation of Bipolar Electrochemistry</i>	<i>187</i>
5.2.5. <i>Understanding Nano-Bipolar Electrochemistry.....</i>	<i>187</i>
References	189

List of Figures

- Figure 1-1 Possible use of bipolar electrochemistry to grow conductive structures at tumour sites. Au NP BPEs are injected to a tumour site and external EFs are then used to grow conductive structures in and around the tumour site. Standard TTFs may then be applied to the tumour site, with EFs being enhanced at the cell/conductive structures interface.13
- Figure 1-2 Schematic of piezoelectric drop on demand print head with corresponding waveform for ink droplet formation.18
- Figure 1-3 Simplified schematic representation of the double layer that forms between an electrode and electrolyte interface, made up of the Outer Helmholtz Layer (OHP) and Nernst Diffusion Layer.21
- Figure 1-4 Schematics of a bipolar electrochemical system (BES), with feeder electrodes (FEs), bipolar electrodes (BPEs) and aqueous electrolyte solution.23
- Figure 1-5 Schematic showing magnetic field that forms around a solenoid causing an impedance to the flow of current.28
- Figure 1-6 Schematic of an ideal capacitor, electrons (-) build up and repel like charges from flowing to the plate. This also repels like charges on the opposing plate (+), forming positively charged atoms. The more charge that builds up, the more current is impeded.29
- Figure 1-7 Phase diagram showing inductive reactance X_L , capacitive reactance X_C , resistance R and resulting impedance Z . Phase angle is denoted as ϕ30

Figure 1-8 Lissajous plot showing excitation potential plotted against resulting current of an alternating current source.....	31
Figure 1-9 Scattered light intensity fluctuation of small (A) and large (C) particles with the corresponding correlograms (B and D). Figure taken from Carvalho et al. ¹⁵⁴	34
Figure 1-10 SEM vs TEM setup.....	37
Figure 2-1 Jetting waveforms for printing TPGDA and Silver using piezoelectric drop-on-demand printer (Dimatix).	52
Figure 2-2 Patterns used to print varying BPEs, used to study the effect of BPE geometry (A) and orientation (B and C).	53
Figure 2-3 Wire growth set up, using optical microscope and high voltage stimulator (HVS), Ag paint contacts and needle electrodes.....	54
Figure 2-4 Wire growth set up with cells for 2D monolayers (left), and 3D spheroids (right). BPEs consisted of single ink drops of ~50 μm . Ibidi sticky-slides were used to contain media in 10 x 10 mm areas around cells. Distance between FEs was equal to 1 mm.	56
Figure 2-5 Wire growth mechanism using Ag as a simple proof of concept. For end application, BPEs model electrodes that would be <i>in vivo</i> (red) whilst FEs would be <i>ex vivo</i> (blue).	58
Figure 2-6 Silver (Ag) and TPGDA ink droplet diameter on varying substrates: Silver (Ag), Glass (G) and polymer adhesion layer (TPGDA). Error bars represent standard error mean (SEM), n = 25.....	60

Figure 2-7 3D printing variation, characterised by FE resistance variations. A: Resistance of pairs of FEs. B: Measured samples were then categorised based on their highest resistance electrode of the pair. C: Number of wires grown for 3 samples from each category. D: wire growth examples for low (I), medium (II), high resistance (III) and non-conductive (IV).61

Figure 2-8 Optical microscopy images of Ag MW connections to and from a BPE in the shape of (I) square, (II) circle, (III) triangle and (IV) diamond (as per Figure 2-2 geometries). Imaged at 4x magnification with Nikon fluorescent microscope (ECLIPSE TE300), scale bars read 250 μm64

Figure 2-9 Modelled electric field and electronic potential of 90 V applied using different geometries of FEs (contour: electric potential (V), arrow surface: electric field).64

Figure 2-10 Diameter, no of connections and resistance of wires established for each geometry BPE. Error bars represent standard error of the mean (SEM), further statistical analysis was performed using one-way ANOVA with Tukey's HSD post hoc analysis ($n=9$; $p\leq 0.01$).66

Figure 2-11 Optical microscopy images of Ag MW growth with varied geometry of BPEs and pattern demonstrating direction control of wire growth. Scale bars represent 250 μm67

Figure 2-12 Comparison of a high quality (A) vs low quality (B) print of Ag BPEs. Scale bars represent 250 μm68

Figure 2-13 Comparison of no. of MWs grown using samples with and without satellite BPEs. Multiple geometries were used in pairs, of with and without satellite BPEs. Examples of those without (A-B) and with (C-D) satellite BPEs can be seen. Mean \pm SEM of no. of MWs grown is plotted ($n = 20$).69

- Figure 2-14 AC MW growth attempted at varying frequencies and potentials. Characteristic wires for varying frequencies at 100 V (or 50 V at 1 MHz) can be seen in images I-VI. 72
- Figure 2-15 Optimisation of spheroid growth comparing rotational speeds of 12 (A), 15 (B) and 18 rpm (C). Initial experiments were performed at 10 days, 15 rpm was then repeated for 7 days..... 74
- Figure 2-16 Optical images of MW growth using 50 V at 1 MHz in the presence of 2D monolayers. Arrows highlight MWs. Scale bars represent 100 μm 75
- Figure 2-17 Optical images of Ag MW growth in the presence of spheroids. Green dotted outlined shows the main bulk of the spheroid. 76
- Figure 2-18 Optical images showing Au MW growth initiating from AuCl. Electrodes were inkjet printed with dH₂O used as an electrolyte. 78
- Figure 3-1 Synthesis of PPy NPs using FeCl₃ as an oxidising agent and PVA as a surfactant. PVA, FeCl₃ and deionised H₂O are combined under stirring and heat (100°C) before pyrrole monomer is added dropwise. The reaction is stirred for 10hrs in a cold room before NPs then being washed using hot water..... 89
- Figure 3-2 Schematic of Au NP synthesis. HAuCl₄ in dH₂O is heated and stirred until a rolling boil is achieved. Sodium citrate is then rapidly added and solution is boiled for a further 10 minutes before filtering..... 90
- Figure 3-3 Schematic of bipolar electrochemical deposition of a metal onto the surface of NPs. Needle electrodes are used to apply an electric field to NP and metal salt solutions in a culture dish. 93

Figure 3-4 PPy NP characterisation using UV-Vis (A), DLS (B) and SEM (C and D). NPs were synthesised using an altered method. Liquid dispersions were used for UV-Vis and DLS measurements, whilst SEM samples were dried onto carbon substrates on aluminium stubs.	96
Figure 3-5 PPy reaction supernatant retrieved after sequential washes in hot water (left to right).....	97
Figure 3-6 SEM of PPy NPs using an adapted method with hot water washes.	97
Figure 3-7 Characterisation of NP size and absorbance using DLS (A) and UV-Vis (B). For DLS measurements n = 3.....	98
Figure 3-8 TEM images of PPy NPs and Au NPs. Scale bars represent 200 and 100 μm (left and right).	99
Figure 3-9 Characterisation of NP conductivity, carried out using electrical impedance spectroscopy EIS of varying PPy (A), Au (B), ScreenMag (C) and ScreenCore (D) NP concentration solutions. Error bars denote mean +/- SEM, n = 3.	100
Figure 3-10 Characterisation of NP biocompatibility using live/dead assay (left/right respectively, Calcein AM/Ethidium Homodimer) for Au NPs (A/B), PPy NPs (C/D), ScreenMag NPs (E/F), and ScreenCore NPs (G/H). Cells were incubated with NPs for 4 (blue), 24 (red) and 48 (green) hours. Fluorescence was normalised using positive and negative controls.....	104
Figure 3-11 Biocompatibility of NPs assessed using WST-8 metabolic assay for Au NPs (A), PPy NPs (B), ScreenMag NPs (C), and ScreenCore NPs (D). Varying concentrations of NPs were suspended in media and incubated with	

cells for 4 (blue), 24 (red) and 48 (green) hours. Absorbance was normalised to a live control to provide metabolic activity %. 105

Figure 3-12 Evaluation of NPs application as BPEs through the measurement of the size distribution of NPs using DLS. NP dispersions in deionised water were measured before and after electrical stimulation, with and without the presence of a metal salt (PdCl_2). 106

Figure 3-13 SEM images of Au NPs in the presence of PdCl_2 , with (B) and without (A) electrical stimulation of 10 V for 10 minutes. Energy dispersive x-ray spectroscopy was used to create elemental maps of Au, Pd and Cl. 109

Figure 3-14 TEM images of single NPs (A/B) with corresponding energy dispersive x-ray (EDS) spectra (C/D/E). NPs were suspended in deionised water with 1mM PdCl_2 , with sample B and inset also being subjected to 10 minutes of electrical stimulation at 10 V. 110

Figure 3-15 TEM with elemental mapping (EDS) of PPy NPs and PdCl_2 with (B) and without (A) electrical stimulation. Nitrogen, Palladium and Chlorine can be seen in i, ii, and iii respectively. 111

Figure 3-16 TEM images of PPy NPs in the presence of PdCl_2 with (C/D) and without (A/B) electrical stimulation. Control of PPy NPs with electrical stimulation alone can also be seen in (E/F). 113

Figure 3-17 The effect of TTFs on cells with and without selected NPs. Fluorescence emitted from the conversion of a metabolic substrate using a Presto Blue assay is plotted to evaluate cell viability at 0-, 4- and 24-hours. Mean ($n = 3$) and SEMs are plotted. Statistical significance was determined using Tukey's multiple comparison test. 116

Figure 4-1: Interaction of electric fields with nanoscale bioelectronic systems. Schematic showing a bipolar electrochemical cell (A); applications of optimising bipolar electrochemistry in vivo (B) and the experimental set-up used herein to evaluate nano and nano-bioelectronic bipolar systems (C). .122

Figure 4-2 Au FE setup. FEs were approximately 2 mm in width, with a 1 mm gap between them. 20 μ L of electrolyte was used to bridge the gap between electrodes, the approximate boundary of this droplet can be seen in blue. Samples with cells were produced using Ibidi[®] sticky slides, creating an approximate area of cell coverage of 1 cm², this can be seen in red. 20 μ L of electrolyte was also added, however, this spread across the entire cell surface.130

Figure 4-3 Basis of EIS method to evaluate BESs, by evaluating the ratio of BPE impedance and electrolyte impedance. Total BES impedance (Z_T), normalized by BPE impedance (Z_B), is plotted against efficiency parameter η (defined in Equation (4-2)) (B). An equivalent circuit can be seen in the inset, with impedance components relating to the FEs Z_F , the electrolyte Z_E , and the BPEs Z_B . Dotted lines show the three distinct areas (I – III) where current flows mostly through the BPEs, is split between BPE and electrolyte, and mostly flows through the electrolyte (A).135

Figure 4-4 Varying PBS concentrations were tested in systems with (B) and without (A) Au NP BPEs. Real impedance was normalized to allow Nyquist plots to be overlaid. Insets show expanded lower frequency portion of graphs. ...139

Figure 4-5 Electrical characterization plots and example circuit fittings of Au FEs with Au NP BPEs in water (A) and PBS (B). Circuit diagrams can be seen in the inset. Warburg impedance was also included in series with the FE to account for diffusion in the system and to allow for better fitting. With Z_E being

modelled as a resistor (R_E) and Z_B modelled as a capacitor (C_B), (C) and (D) show the average magnitudes of R_E and C_B respectively in samples using water (blue) and PBS (red). C_F averages can be seen in Figure 4-6. Error bars show standard error of mean ($n = 3$). Efficiency parameter (η) of 125 nm Au NP BPEs in PBS (blue) and deionized water (red) can be seen in (E)..... 140

Figure 4-6 Average magnitudes of FE capacitance in water (blue) and PBS (red), from circuit fittings used in Figure 4-5..... 143

Figure 4-7 Raw data of bipolar system with Au NP BPEs in PBS. Fitting lines show fitting with (red) and without (green) the BPE component..... 144

Figure 4-8 Cellular uptake analysis of Au NP BPEs comparing two concentrations of Au NPs and two incubation times. Confocal microscopy was used to image U251 cells incubated with Au NPs conjugated with Zn porphyrin (A). All scale bars represent 50 μm . Mean cell fluorescent intensity as a function of cellular uptake and SD was plotted for at least 20 cells (B) & (C). All the values were normalized with fluorescent intensity obtained with Au NP concentration of 50 $\mu\text{g}/\text{ml}$ (B) or Au NP incubation time of 24 hours (C). 50 $\mu\text{g}/\text{ml}$ Au NP concentration was taken forward from B to perform the incubation time study in C..... 147

Figure 4-9 Fluorescent emission spectrum of Au NPs functionalized with zinc porphyrin monitored upon excitation with a wavelength of 422 nm.... 147

Figure 4-10 Inductively coupled plasma mass spectrometry (ICP-MS) results for 25, 50 and 500 $\mu\text{g}/\text{ml}$ of Au NPs incubated with U251 cells for 6 or 24 hours..... 148

Figure 4-11 Analysis of toxicity effects of varying concentrations of Au NPs (from 12.5 $\mu\text{g}/\text{ml}$ to 500 $\mu\text{g}/\text{ml}$) on U251 cells. Fluorescence microscopy images

of U251 cells treated with Au NPs at different concentrations. Blue: represents Hoechst staining (blue, all cells); White arrows: represent PI staining (red, membrane damaged cells). Scale bar is 50 μm (A). Corrected total cell fluorescence of red PI fluorescence (membrane damaged cells) quantified in the area of the cells using imageJ. Statistical significance was calculated using a one-way ANOVA test ($n = 100$; error bar represents SD; triplicate) (B). Metabolism of U251 using WST-8 assay (Cell Counting Kit Sigma Aldrich). Metabolic activity was normalized as a percentage of a control well without Au NPs (C).....150

Figure 4-12 Example data of samples with Au NPs and cells present, using water as an electrolyte. Nyquist plots (A) and Phase angle (B) are plotted, with fitting data overlaid in black. (C) and (D) show circuits fitted to water and PBS respectively.....153

Figure 4-13 Comparison of fitting values from samples with cells and Au NPs at two concentrations: 50 and 500 $\mu\text{g}/\text{ml}$. Capacitance (C) and resistance (R) values from circuit fittings can be seen using water (blue) and PBS (red) as electrolytes. FE capacitance values can be found in Figure 4-15. Circuits used can be seen in Figure 4-12. Error bars show standard error of the mean ($n = 3$). Significant differences (*) were assessed using two-way ANOVA and Tukey's multiple comparison test.....155

Figure 4-14 Graphs showing sample fitting of raw data of systems with living cells, in water (A) and PBS (B). Such fitting was used to determine resistance and capacitance values seen in Figure 4-13.156

Figure 4-15 Average magnitudes of FE capacitance in water (blue) and PBS (red), from circuit fittings used in Figure 4-13.....156

Figure 5-1 Pattern for inkjet printing of 3D structures showing varying height BPEs, produced by printing 10, 20 or 30 layers of TPGDA, followed by three layers of Ag.....	173
Figure 5-2 Ag MW growth using 3D structures.	173
Figure 5-3 Attempted AC wire growth with cells, images showing BES before (A), during (B) and after (C and D) electrical stimulation.	175
Figure 5-4 Impedance measurements during wire growth, set up (A) and example bode plot in galvanostatic mode (B).	178
Figure 5-5 Impedance measurements before and after wire growth (C). Example wire growth samples can be seen in A and B, scale bars show 100 μm	178
Figure 5-6 Schematic of bipolar electrochemical deposition of a metal onto the surface of NPs, whilst incorporated in <i>C. elegans</i>	179
Figure 5-7 TEM images of <i>C. elegans</i> cross-sections. Scale bars represent 2 μm	181
Figure 5-8 Anatomy of an adult <i>C. elegans</i> Image created by K.D. Schroeder.	182
Figure 5-9 Micro-injection of <i>C. elegans</i> (A) and fluorescent image of <i>C. elegans</i> with fluorescent nanoparticles (B).....	183

List of Tables

Table 1-1 Types of additive manufacturing as per ASTM standard F2791 – 13 (2019), with examples of their applications in manufacturing electronics	16
--	----

Table 3-1 Coefficient of variance of NP impedance measurements at 100 Hz, supporting data presented in Figure 3-9 (n = 3).....102

Abbreviations

η_{an}	Overpotential at the Anode
η_{cat}	Overpotentials at the Cathode
<i>2D</i>	Two-dimensional
<i>3D</i>	Three-dimensional
<i>AC</i>	Alternating Current
<i>AFM</i>	Atomic Force Microscopy
<i>Ag MW</i>	Silver Microwire
<i>AgNP ink</i>	Silver Nanoparticle Ink
<i>ASTM</i>	American Society for Testing Materials
<i>ATCC</i>	American Type Culture Collection
<i>Au NPs</i>	Gold Nanoparticles
<i>BES</i>	Bipolar Electrochemical System
<i>BPE</i>	Bipolar Electrode
<i>C</i>	Capacitance (F)
<i>C. elegans</i>	Caenorhabditis Elegans
<i>CAD</i>	Computer-Aided Design
C_B	Bipolar Electrode Capacitance

C_E	Electrolyte Capacitance
C_F	Feeder Electrode Capacitance
C_O	Concentration of oxidised electroactive species at the surface of the electrode (mol)
C_R	Concentration of reduced electroactive species at the surface of the electrode (mol)
<i>CTCF</i>	Corrected Total Cell Fluorescence
d	The length or diameter of the BPEs
D	Diffusion Coefficient ($\text{cm}^2 \text{s}^{-1}$)
<i>DBS</i>	Deep Brain Stimulators
<i>DC</i>	Direct Current
<i>dH2O</i>	Deionized Water
<i>DLS</i>	Dynamic Light Scattering
<i>DMEM</i>	Dulbecco's Modified Eagle Medium
<i>DNA</i>	Deoxyribonucleic Acid
<i>DOD</i>	Drop-on-demand
E	Potential (V)
e	Electron
<i>E. coli</i>	Escherichia coli
<i>ECIS</i>	Electrical Cell-Substrate Impedance Sensing
<i>ECT</i>	Electric Convulsive Therapy
<i>EDC</i>	1-Ethyl-3-(3-dimethylaminopropyl)carbodiimide

<i>EDMA</i>	Electromotive Drug Administration
<i>EDS</i>	Electron Dispersive Spectroscopy
<i>EF</i>	Electric Field
<i>EIS</i>	Electrochemical Impedance Spectroscopy
<i>EM</i>	Electron Microscopy
E°	Standard Potential (V)
<i>EON</i>	EIS on a Needle
<i>EPR</i>	Enhanced Permeability and Retention Effect
<i>EthD-1</i>	Ethidium Homodimer 1
E_x	Potential at a given point x on the surface of a particle (V)
F	Faradaic constant (F)
f	Frequency
<i>FBS</i>	Fetal Bovine Serum
<i>FDA</i>	Food and Drug Administration
<i>FE</i>	Feeder Electrode
G	Glass
<i>HBSS</i>	Hank's Balanced Salt Solution
<i>HOMO</i>	Highest Occupied Molecular Orbital
<i>HVS</i>	High Voltage Stimulator
i	Current (A)
<i>ICP-MS</i>	Inductively Coupled Plasma Mass Spectrometry

<i>ITO</i>	Indium Tin Oxide
<i>KK</i>	Kronig-Kramer
<i>KOH</i>	Potassium Hydroxide
<i>L</i>	The distance between the FEs
<i>LED</i>	Light Emitting Diode
<i>Ln</i>	Natural Log
<i>LUMO</i>	Lowest Unoccupied Molecular Orbital
<i>MUA</i>	11-Mercaptoundecanoic Acid
<i>n</i>	Number of moles of electrons
<i>NHS</i>	N-hydroxysuccinimide
<i>NICE</i>	National Institute for Health and Care Excellence
<i>NP</i>	Nanoparticles
<i>OCD</i>	Obsessive Compulsive Disorder
<i>PAH</i>	Poly(Allylamine Hydrochloride)
<i>PBS</i>	Phosphate Buffer Saline
<i>PCB</i>	Printed Circuit Board
<i>PDD</i>	Poly(Sodium 4-Styrenesulfonate)
<i>PDI</i>	Polydispersity Index
<i>PDT</i>	Photodynamic Therapies
<i>PEDOT</i>	Poly(3,4-ethylenedioxythiophene)
<i>PLA</i>	Polylactic Acid

<i>PPy</i>	Polypyrrole
<i>PPy NPs</i>	Polypyrrole Nanoparticles
<i>PTT</i>	Photothermal Therapy
<i>PVA</i>	Polyvinyl Acetate
<i>R</i>	Electrical Resistance (Ω)
<i>R</i>	Gas constant ($\text{J mol}^{-1} \text{K}^{-1}$)
<i>RC</i>	Resistor, Capacitor Circuit
<i>RCCS</i>	Rotary Cell Culture System
<i>R_E</i>	Electrolyte Resistance
<i>Redox</i>	Reduction and Oxidation
<i>rpm</i>	Revolutions Per Minute
<i>RT</i>	Room Temperature
<i>SD</i>	Standard Deviation
<i>SEM</i>	Standard Error of the Mean
<i>SEM</i>	Scanning Electron Microscopy
<i>SMase</i>	Sphingomyelin Phosphodiesterase
<i>ssDNA</i>	Single Stranded DNA
<i>T</i>	Temperature (K)
<i>TEM</i>	Transmitted Electron Microscopy
<i>TPGDA</i>	Tri(propylene) Glycol Diacrylate
<i>TTF</i>	Tumour Treating Field

<i>UK</i>	United Kingdom
<i>UV</i>	Ultraviolet
<i>UV Vis</i>	UV Visible Light Spectroscopy
<i>V</i>	Potential difference (V)
<i>WST-8</i>	Water-Soluble Tetrazolium salt
X_C	Capacitive Reactance
X_L	Inductive Reactance
<i>z</i>	Valence of ionic species
<i>Z</i>	Impedance
Z_B	Bipolar Electrode Impedance
Z_E	Electrolyte Impedance
Z_F	Feeder Electrode Impedance
Z_T	Total Impedance
ΔE	Potential difference between the two extremities of the bipolar electrode (V)
θ	Angle relative to the direction of the electric field
ρ	Resistivity (Ω cm)
\varnothing	Diameter

Chapter 1. Introduction

1.1. Literature Review

1.1.1. Bioelectronic Medicine

The coupling of electronics with biology is termed bioelectronics and allows for a diverse range of applications such as the generation of energy¹, sensing of biomolecules², to restore physical disabilities^{3,4}, and, most relevant to this thesis, for treatment of disease⁵.

Bioelectronic medicine is an emerging, yet fast-growing field; with a market of nearly \$20 billion today, it is expected to hit \$60 billion by 2029¹. This value is mostly divided between the bioelectronics for retinal, cochlear implants, cardiac solution, and peripheral and central nervous system stimulation².

Electrical stimulation to influence neurons is no new exploit, with electric convulsive therapy (ECT) dating back to 1934 for the treatment of epilepsy⁶. Despite its controversy, ECT played a huge part in the treatment of psychiatric diseases for many years and was greatly improved upon⁷. However, as it was developed from clinical observations in mental institutes and not research laboratories, and its mechanism of action was not known, it was described as ‘unscientific’⁶ and anecdotal. Nonetheless, this highly controversial therapy

forms the basis of clinically utilising electrical stimulation to modulate biological activity.

The first pacemaker was implanted in a human in 1958⁸, and this technology has advanced majorly since then, with devices becoming smaller and the procedure now routine. Deep brain stimulators (DBS) are now used in therapies for various brain disorders such as Parkinson's⁹, epilepsy¹⁰ and Obsessive Compulsive Disorder (OCD)¹¹. Other avenues of research for using DBS include depression¹², obesity, addiction and cluster headaches^{10,13,14}. Cochlear implants are used to restore hearing loss with great success for both children and adults. Once analogue, single electrode, percutaneous transmission devices now incorporate digital, multi-electrode transcutaneous transmission with complex feature extraction processing¹⁵⁻¹⁷. Retinal implants begin to restore basic sight, with the Argus II device gaining both FDA approval and CE marking^{3,18}. Other devices are close to adoption that better mimic normal eye movement in order to see (Alpha-IMS¹⁸). Bionic noses and tongues are being developed that also mimic human sensory functions to be used for food quality and safety applications¹⁹⁻²¹.

Semiconductor technology has advanced greatly (as per Moore's Law²²), allowing us to produce smaller, more efficient electrical devices for implantation. Harnessing electrical communication over chemical signalling has the capability of providing better spatial and temporal resolutions due to its

fast and targeted nature^{5,23}. This, along with our ever-increasing understanding of biology, brings new and exciting possibilities to bioelectronics. However, a number of limitations currently exist.

Most traditional bioelectronic therapies can be simplified to an electronic device, a power source, and the surgery required to implant these. Currently, this combination can produce dramatic clinical benefits, in spite of the fact that they do not target specific cells⁵. This inability to target specific cells is due to the low spatial resolution of devices caused by the size difference between electrodes on devices and the cells they are targeting. This means, for example, cochlear implants do not provide perfect hearing, retinal implants allow only the vision of blurred shapes and shadows, and bionic arms controlled by thought can only be moved in limited ways.

In addition to device performance, the size difference means they may activate, or inhibit, large populations of cells in an area of tissue involved in diverse and unrelated functions, thereby leading to adverse side effects. Furthermore, a device may be rejected due to biofouling²⁴ and has a limited lifetime, therefore requiring periodical replacement. A device needing implantation is also invasive, and may not be feasible, nor ethical, in certain areas of the body.

Further limitations of current bioelectronics are the electronics themselves. Standard manufacturing processes for electronics produce hard, brittle

structures, not suitable for integration with biology. Hence, new manufacturing processes and materials are required to allow the production of nanoscale, flexible components that merge seamlessly with biological systems.

1.1.2. Manufacturing Bioelectronics

Electronic devices are a set of components connected together to manipulate the flow of electrical current into doing something useful. Such manipulation is accomplished using electrical components that resist, carry, switch, store and exploit the electron. These components could be passive, such as those discussed in section 1.2.4; resistors; capacitors and inductors; or active. Examples of active electrical components are Light-Emitting-Diodes (LEDs) and transistors, which require a power source to function and have the ability to introduce more energy into a circuit.

Basic electrical components, both passive and active, are made of functional materials that can then be connected or added to various substrates to regulate the flow of electrons and form a circuit. These functional materials could be in the form of solids, pastes and inks etc. and hence are either placed or printed onto substrates.

Traditional electronics often consist of printed circuit boards with electronic components soldered to them. Copper coated glass fibre reinforced epoxy resin printed circuit boards (PCBs) are produced using photoresists to map a circuit design onto the PCB, followed by etching of the unwanted copper.

Precision holes are then drilled and plated to allow for the placement of electronic components. More complex PCBs can be created using a layering process to layer multiple circuits on top of each other. This manufacturing process has greatly improved in the last few decades, moving from through-hole manual component soldering to automated surface mount technology. Despite great throughput and complexity advances, this manufacturing process is still extremely wasteful and carries great environmental impacts. Printing technology is now used to create complex patterns for PCBs, however, these processes are used to create masks rather than to directly print PCBs. This means many additional processes and a high volume of harmful chemicals are needed to then plate and etch PCBs using the printed masks. This also requires great amounts of water for washing processes and has the associated costs of processing such chemicals and water for re-use.

As we progress into a more technology-dependent era, we require more complex electronics with higher information processing capabilities without compromising on size²⁵. Therefore, processes required to manufacture micro-scale electronics are of great importance. As with all electronics, micro-scale electronics are manufactured from a bottom-up or top-down approach, outside of the body. 3D printing is a novel fabrication method that allows production of micro-scale electronics. With multiple 3D printing techniques capable of printing a wide range of materials with varying properties, from polymers and metals to biological material, 3D printing allows for the

manufacture of complex electronic circuits and integrated components. This will be discussed further in section 1.2.1.

Although further developing nanoscale electronics would allow for better integration *in vivo*, this would still not create unified bioelectronics. Hence, novel approaches are required to manufacture bioelectronics that seamlessly merge with biology.

With bioelectronic therapies dating back many decades, original bioelectronic devices consist of traditional electronic devices/components housed in a biocompatible casing. Examples include pacemakers and cochlear implants, whose robust design has barely altered for years. As we learn more about bioelectricity and its link to organ, tissue and cellular functions²⁶, innovative bioelectronics are required to sense and actuate bioelectricity. Many areas of the body are not accessible to large bioelectronic devices and implanted electrodes and hence, to fully exploit electricity as a therapeutic pathway, we require new ways of thinking when approaching the design and manufacture of bioelectronics. Liu et al. highlighted the need for bioelectronics to be redesigned: being 3D rather than planar, with micro/nanoscale feature sizes and comparable or softer mechanical properties than biological tissue²⁷.

Microfabrication methods, such as inkjet and screen printing, have been adapted using novel biomaterials to create soft, flexible electronics²⁸. This has allowed skin-like electronics to be produced for novel applications such as

tattoo sensors^{29–31}, neural interfaces³², and *in vivo* monitoring³³. This brings exciting possibilities for biosensing and wearable technology, however for *in vivo* bioelectronics, soft electronics would still require implantation and provide only a 2D interface with biology.

In order to fully exploit our new understanding of bioelectricity and its effect on cell functions in all types of cells, a novel approach to the design and manufacture of bioelectronics is required. This may allow for not only the improvement of existing bioelectronic therapies, but also the addition of innovative therapies. For example, could electroceutics ‘coax insulin from cells to treat diabetes, regulate food intake to treat obesity, correct balances in smooth-muscle tone to treat hypertension and pulmonary diseases’⁵, or specifically target tumour cells and program their cell death?

1.1.3. Bioelectronics in Cancer

Advances in neuroscience have shown that both central and peripheral nervous systems play a key role in diseases with the highest mortality, such as cancer³⁴. Together with these advances, researchers have realised the potential of capturing, analysing and mediating bioelectrical signals from the body for the detection and treatment of tumours using bioelectronic devices. Dysfunctional neural circuits give rise to defective signals that promote the growth of cancers of the brain, prostate, stomach, pancreas, and skin and which offer a novel therapeutic window³⁵. Moreover, ion channels that define

cellular bioelectricity are abnormally expressed and active in both cancer patient biopsy tissues and cancer cell lines^{36–39}. Other key phenotypic changes that underpin cancer progression include membrane potentials, cell metabolism (the warburg effect), trans-plasma membrane electron transport activity, and cellular pH (Figure 1-1). This altered cellular bioelectricity is highly intertwined⁴⁰ and modulates the process of metastasis⁴¹, including degradation of basement membranes, cancer cell invasion, migration, extravasation and colonisation^{42–46}. Due to this, bioelectronic medicine could prove to be a breakthrough in preventing cancer progression. Moreover, these altered bioelectronic circuits could also be targetted in novel diagnosis methods.

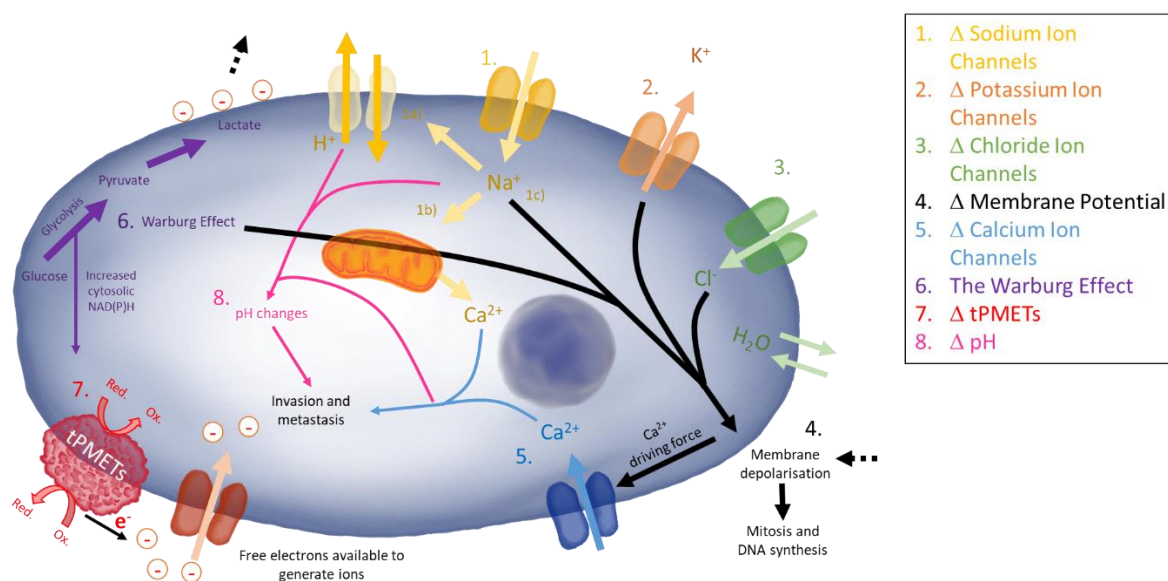


Figure 1-1 Complex bioelectrical interactions present in cancer cells between ion channels (1, 2, 3, and 5), membrane potential (4), cell metabolism (6), faradaic processes (7), and cellular pH (8). These interactions are discussed in detail by Robinson et al.⁴⁰

Researchers are now interested in developing various bioelectronics-based therapeutic devices for the stimulation and neural modulation of the tumour microenvironment. This could allow us to regulate cancer signalling pathways, to restore healthy patterns of electrical impulses, and to stop cancer progression. Recent innovations and progress in the field of bioelectronic medicine could prove to be a more natural and safer approach for treating cancer compared to chemotherapy and surgery, which are associated with various deleterious side effects, which may even persist for a lifetime.

In today's world, electric field therapies are provided alongside chemotherapy to patients with certain types of cancer to achieve improved survival and safety benefits. For instance, Byrne *et al.* demonstrated that a high concentration of localized drug can be forced deep inside the tumours by using low DC electric current, referred to as "iontophoretic chemotherapy"⁴⁷. Several laboratories have pioneered the use of delivering neurotransmitters using electrophoretic-based bioelectronics⁴⁸ and shown that neuronal firing can be controlled *in vivo*. To our knowledge, this has not been applied to cancer systems, despite the fact that recent landmark studies have shown that glial cancer cells can cross-communicate functionally with neuronal cells to aid cancer progression⁴⁹⁻⁵¹. There is clear scope here to impact with such devices. Electrochemotherapy, which involves electric pulses to send the chemotherapy into the cancer cells, has been approved by the National Institute for Health and Care Excellence (NICE) for the treatment of skin cancer⁵²⁻⁵⁴. The clinical

trial outcomes of these studies have suggested that electrical current appears to improve the efficacy of the adjuvant chemotherapy. Encouraged by this, researchers are now trying to develop new electricity-driven cancer therapies for more advanced cancers such as high-grade bladder cancer. These treatments are deemed “electrically stimulated intravesical chemotherapy” or “electromotive drug administration (EMDA)”^{55,56}. Another well-known bioelectronic device is “Optune”, which uses alternating electric fields (also known as tumour treating fields or TTFs) to halt the growth of cancer cells. This device is currently used adjuvant to standard-of-care chemotherapy in patients with newly diagnosed glioblastoma (grade IV astrocytic brain tumour) after treatment with surgery and radiation therapy⁵⁷. This battery-powered bioelectronic device “Optune”, launched by Novacure, has shown encouraging results in improving the survival and quality of life in patients suffering from glioblastoma and has been approved for clinical use by the US Food and Drug Administration.

Bioelectronic approaches to treating cancer are lacking in current clinical practice. However, as the field advances, it can be expected that such an approach could improve treatment across several cancer types. To aid in this advancement, we must understand how bioelectricity underpins the cancer phenotype. This includes not only ionic currents, which have been extensively reviewed^{26,58}, but also faradaic currents and the key links between them that we have postulated^{59,60}. As we develop a higher understanding of the

bioelectricity of cancer cells, novel methods are required to sense and actuate these bioelectronic circuits, in order to exploit them for cancer diagnosis and treatment; this thesis will address this need.

1.1.3.1. *Tumour treating fields (TTFs)*

One bioelectronic cancer therapy, mentioned above, that is particularly relevant to this thesis is tumour treating fields (TTFs). TTFs involve the use of high-frequency electric fields, applied *ex vivo*, to disrupt cell division. This form of therapy is currently licensed in the US for the treatment of brain tumours (Optune); however, other cancer cell types have also shown promising responses to this treatment in pre-clinical research⁶¹, and further clinical trials are being performed such as for the treatment of childhood glioma and ependymoma⁶². Theory suggests that the mechanism of action is due to electric fields causing disruption to cell division in the metaphase and telophase/cytokinesis steps of the cell cycle. During metaphase/anaphase, tubulin dimers align with the electric field and therefore the formation of the mitotic spindle is disrupted^{63,64}. During telophase/cytokinesis, non-uniform electric fields formed within the dividing cells, drive charged and polar macromolecules and organelles towards the cleavage furrow and hence lead to errors in cell division and cell death^{61,65}. As it has been postulated that electric fields within this range should not penetrate the highly resistive cell membrane⁶⁶, these effects may be downstream to EF effects on the cell membrane. This requires further investigation, but understanding EF effects on

the cell membrane, and how these alter cell functions, could lead to efficacious EF therapies being developed.

TTFs offer a new avenue for the treatment of newly diagnosed glioblastoma, with clinical trials showing moderately increased overall survival rates compared to chemotherapy alone⁶⁷. Further clinical trials are also taking place to assess the application of TTFs in treating non-small cell lung cancer, brain metastases, pancreatic cancer, ovarian cancer, liver cancer and mesothelioma⁶⁸. As well as identifying other cancer types that may benefit from TTFs, current research is also assessing the application of TTFs adjuvant to other treatment modalities such as chemotherapies⁶⁹⁻⁷². Despite the broad interest and proven efficacy, TTFs have not been widely approved for the treatment of glioblastoma; for example, the UK Medicines and Healthcare Products Regulatory Agency are yet to approve due to the cost-benefit ratio. Further improvements to reduce high costs will likely result in wider uptake.

One possible avenue for reducing high costs and optimising this therapy is through the use of in-situ grown electronics. Current treatment involves the application of *ex vivo* stimulation; however, by introducing *in vivo* electronics, EFs could be enhanced at the tumour site. This could allow for shorter treatment times, lower electrical inputs and therefore potentially lower costs.

1.1.3.2. Wireless Bioelectronics

The work within this thesis could provide a novel method to grow *in vivo* electronics at tumour sites as discussed above. This concept is suggested in Figure 1-2 and would involve the introduction of metal salts or a conductive monomer at a tumour site, along with BPEs likely in the form of NPs. Upon the application of *ex vivo* applied EFs, conductive structures could be grown. These conductive structures would become polarised within an EF and hence will generate their own local EFs. This will enhance EF effects at the tumour site during traditional TTF application, and hence potentially allow for improved treatment outcomes.

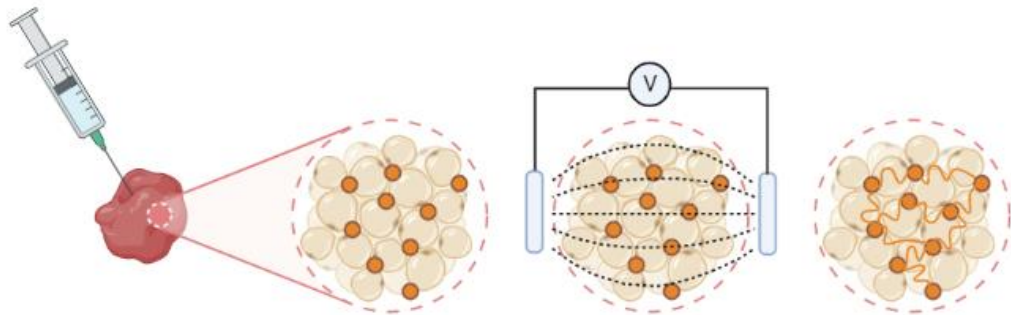


Figure 1-2 Possible use of bipolar electrochemistry to grow conductive structures at tumour sites. Au NP BPEs are injected to a tumour site and external EFs are then used to grow conductive structures in and around the tumour site. Standard TTFs may then be applied to the tumour site, with EFs being enhanced at the cell/conductive structures interface.

This concept could also aid in the diagnosis and treatment of cancer in novel ways. As aforementioned, cancer cells possess multiple different bioelectronic properties in comparison to healthy cells, and these differences may be

exploited for both diagnosis and treatment. The development of a wireless system that is able to probe or actuate these varying bioelectronic properties could greatly alter the current clinical framework for treatment and diagnosis. By targeting unique biomarkers present in cancer cells, wireless NP systems could be used to sense bioelectricity to inform diagnosis, or to actuate bioelectronic pathways to aid in treatment by halting progression, proliferation, invasion, and metastasis.

1.2. Theoretical Framework

Due to the highly interdisciplinary nature of bioelectronic medicine, multiple fields are combined in this thesis, working towards optimising a novel bioelectronic medicine approach. These fields are discussed below and include 3D printing/additive manufacturing, electrochemistry/bipolar electrochemistry, and electrochemical impedance spectroscopy.

1.2.1. 3D Printing/ Additive Manufacturing

The first instance of creating a three-dimensional object utilising computer-aided-design (CAD) was developed in the 1980's as a 'rapid prototyping' tool to quickly realise a 3D model of a design⁷³. This layer-by-layer methodology has since been developed into seven different forms of 'additive manufacturing' or '3D printing' as defined by ASTM Standard F2791 (Table 1-1). Such methods now allow us to 3D print a vast range of materials from polymers⁷⁴, metals⁷⁵ and ceramics⁷⁶ to living cells⁷⁷. This has allowed 3D printing to aid in industries such as aerospace⁷⁸, automotive⁷⁹, biomedical⁸⁰ and electronics²⁵.

Table 1-1 Types of additive manufacturing as per ASTM standard F2791 – 13 (2019), with examples of their applications in manufacturing electronics

		Method Description	Electronics Examples
<i>Powder</i>	Binder Jetting	Liquid bonding agents are selectively printed to bind together layers of powdered material. Parts are then cured in a furnace	Conductive graphene/polyvinyl alcohol composites for flexible electronics ⁸¹
	Direct Energy Deposition	Wire or powder is fed into a melt pool, on the surface of a part, where it is adhered to the below part using a laser or electron beam	Hybrid manufacturing of conductive parts with embedded sensors ⁸²
	Powder Bed Fusion	Powdered material is selectively consolidated by melting it together using a laser or electron beam heat source	Integration of powder bed fusion printed parts with electronic components ⁸³
<i>Solid</i>	Material Extrusion	Material is extruded through a nozzle or orifice and combined layer by layer	3D printed quantum dot LEDs ⁸⁴
	Sheet Lamination	Sheets of material are laminated together, using adhesive, welding or brazing, to form a 3D object	Sheet laminated sensors and integrated circuits for health monitoring ⁸⁵
<i>Liquid</i>	Material Jetting	Droplets of material are deposited layer by layer to create a 3D part, either by UV polymerisation or molten material solidification	Flexible electronics printed using inkjet printing ⁸⁶
	Vat Photo-polymerisation	Vat of liquid resin is cured layer by layer through selective exposure to light, which initiates polymerisation	Electric switches, piezoelectric devices, and sensors ⁸⁷

With 3D printing being capable of printing a wide range of materials, in great complexity at micro/nanoscale precision, it is very attractive to the

electronics industry. All seven printing methods have previously been applied to manufacture electronics either wholly or in part, as detailed in Table 1-1.

For the purpose of this thesis, simple near-two-dimensional electronics are required for use as feeder electrodes (FEs) and hence the most-simple 3D printing technique, that is capable of printing metals, was chosen: material jetting.

Material jetting creates objects in a similar fashion to a traditional inkjet printer, whereby 'ink' is jetted onto a build platform using either a continuous or Drop on Demand (DOD) approach. DOD printers, such as that used in this project, hold a reservoir of ink that is deposited 'on demand' as opposed to the continuous ejection of material. DOD printers can then be sub-divided into how they eject their material. This can be either through thermal activation, by heating an ink to generate a bubble used to displace ink, or by using a piezo electric material. A piezoelectric material is that which deforms under the application of a voltage. Piezoelectric DOD printing uses such materials in the ink reservoir to decrease the reservoir volume and therefore generate the pressure needed to eject a droplet of ink (Figure 1-3). Using Piezoelectric DOD over thermal DOD allows more volatile solvent inks to be used as well as higher viscosity inks, therefore allowing a wider range of materials to be printed.

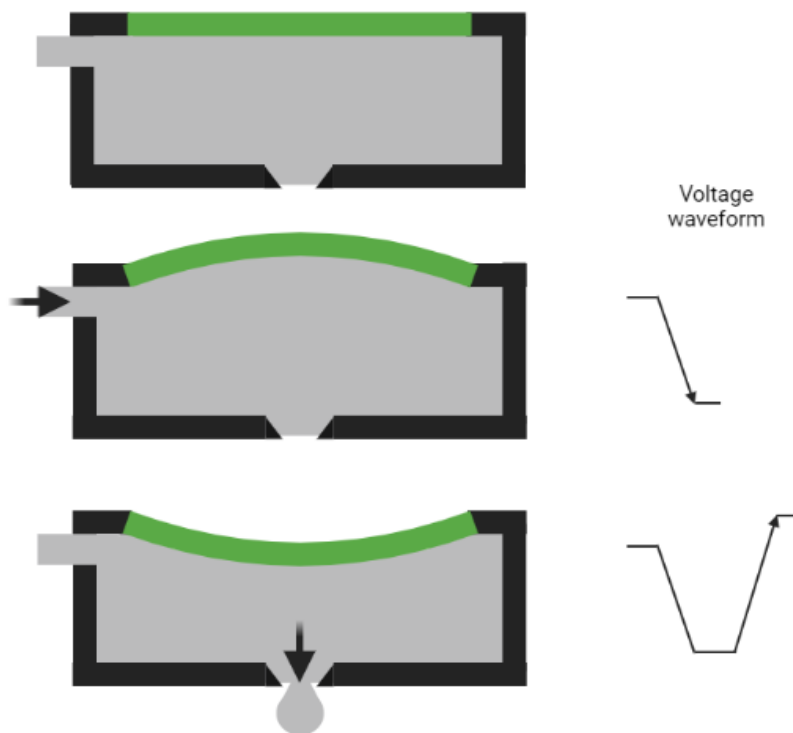


Figure 1-3 Schematic of piezoelectric drop on demand print head with corresponding waveform for ink droplet formation.

Here-in a Dimatix DOD Inkjet printer is used with silver nanoparticle ink (AgNP) to create simple electronics to be used as electrical stimulators/feeder electrodes (FEs). This method is discussed in detail in section 2.2.1.

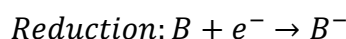
1.2.2. Electrochemistry^{88,89}

Electrochemistry is a branch of chemistry that deals with the relations between electrical and chemical phenomena. This is largely the study of chemical processes caused by the movement of electrons. These movements of electrons, from one element to another in a reaction, are deemed reduction and oxidation reactions or 'redox' reactions: whereby a reduced species gains an electron, and the oxidised species will lose an electron as seen in Equation

(1-1) – (Equation (1-3)). Redox reactions can be spontaneous, such as in a galvanic cell, or controlled by the application of a potential, such as in an electrolytic cell. Within this thesis, we consider electrolytic cells, whereby we will apply an external potential in order to drive a desired redox reaction.



Equation (1-1)



Equation (1-2)



Equation (1-3)

The ease of gain/loss of electrons in redox reactions is dependent on the energy levels of the two species. If the lowest unoccupied molecular orbital (LUMO) of one species is at a lower energy than the highest occupied molecular orbital (HOMO) of another species, then the transfer of electrons takes place. With the application of a potential, one can drive the oxidation or reduction of species. The potential at which reduction or oxidation takes place is unique for each system and is related to the standard redox potential (E°) of the species involved.

Standard redox potentials are the potentials at which a species can be reduced or oxidised under standard conditions (at 25 °C, 1 atm, using 1 M solutions, using a standard hydrogen electrode as a reference). To calculate potentials required at non-standard conditions, and predict the concentration

of oxidised and reduced species at a given potential, the Nernst equation can be used (Equation (1-4))⁸⁸.

$$E = E^{\circ} - \frac{RT}{nF} \ln \frac{C_R}{C_O}$$

Equation (1-4)

Where E = potential, R = gas constant, T = temperature, n = number of moles of electrons involved in the redox exchange, F = faradaic constant and C_O/C_R = concentrations of the oxidised/reduced species at the surface of the electrode.

Electrochemical reactions can either be limited by chemical kinetics or mass transport to the electrode. There are three forms of mass transport which can influence electrochemical reactions. These include migration, convection and diffusion. Migration relates to the electrostatic forces generated from the application of a potential, convection results from the action of a force on the solution (such as stirring) and diffusion occurs when there are uneven concentration gradients and entropic forces act to even out the concentration of species. Diffusion is particularly significant in electrochemical reactions as the reaction takes place at an electrode surface and therefore uneven concentrations arise between the electrode surface and the bulk solution.

When an electrode or charged particle is immersed into a liquid, such as an aqueous electrolyte solution, an electrical double layer forms to balance charge

at the surface of the electrode or particle. As seen in Figure 1-4, this double layer consists of two regions of ion distribution: a compact layer and a diffuse layer. In the compact layer, ions are strongly adsorbed by the electrode surface, whilst in the diffuse layer ions are distributed with a concentration gradient. For simplicity, ions from the supporting electrolyte are not shown. Due to the ability of the electrical double layer to hold charge, it may be modelled as a capacitive element. The thickness of this double layer may be described by the Debye length (k) and decreases with increasing electrolyte concentration.

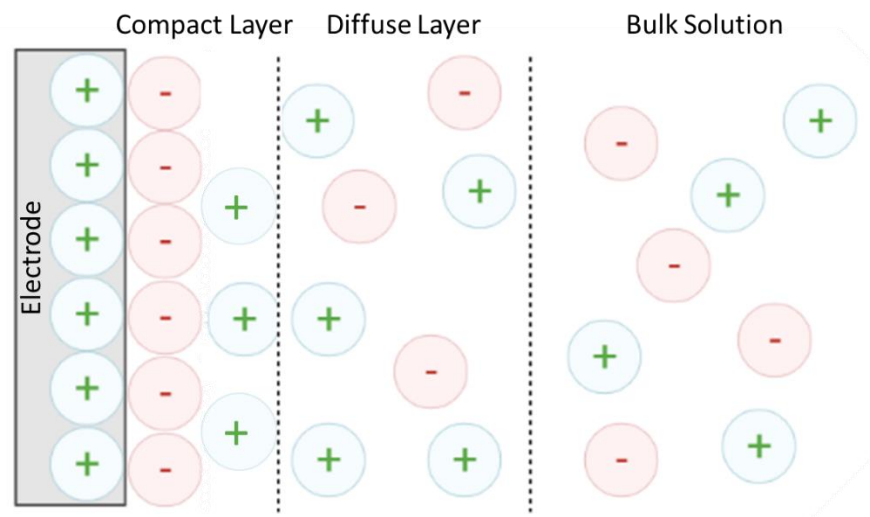


Figure 1-4 Simplified schematic representation of the double layer that forms between an electrode and electrolyte interface, made up of the compact layer and diffuse layer.

1.2.3. Bipolar Electrochemistry

Bipolar electrochemistry is a concept within electrochemistry, which forms the basis of this thesis. Figure 1-5 shows a typical set up of an open bipolar electrochemical cell. Closed systems are also possible, in which the solutions in

contact with the anode and cathode are separated, however these will not be discussed here. An open system seen in Figure 1-5 includes: feeder electrodes (FEs) (positive and negative), which are attached to a power source; one or many bipolar electrodes (BPEs), which are not attached to a power source; and an aqueous electrolyte solution. FEs are used to apply a uniform electric field across the electrolyte solution. This electric field (E_{tot}) will polarise conductive objects within it, and hence the bipolar electrode (BPE) will then possess two poles (δ^+ and δ^-) that can act as an anode and cathode in electrochemical reactions⁹⁰. Due to the BPE being conductive, its potential (E_{elec}) is in equilibrium across its surface. However, the presence of the electric field means the interfacial potential difference between the BPE and the solution varies along the BPEs length. It is these varying overpotentials (η_{an} and η_{cat}) that can drive electrochemical reactions at the poles of the BPE^{91,92}. The poles of the BPE are orientated in the opposite polarity to the FEs⁹³, with the highest overpotentials being generated at the extremities of the BPE. The location on the BPE at the boundary between the two poles has zero overpotential with respect to the solution (x_0). Although this is in the centre of the BPE in Figure 1-5, its actual location depends on the faradaic processes taking place at the poles of the BPE⁹², as well as the geometry of the BPE⁹⁴.

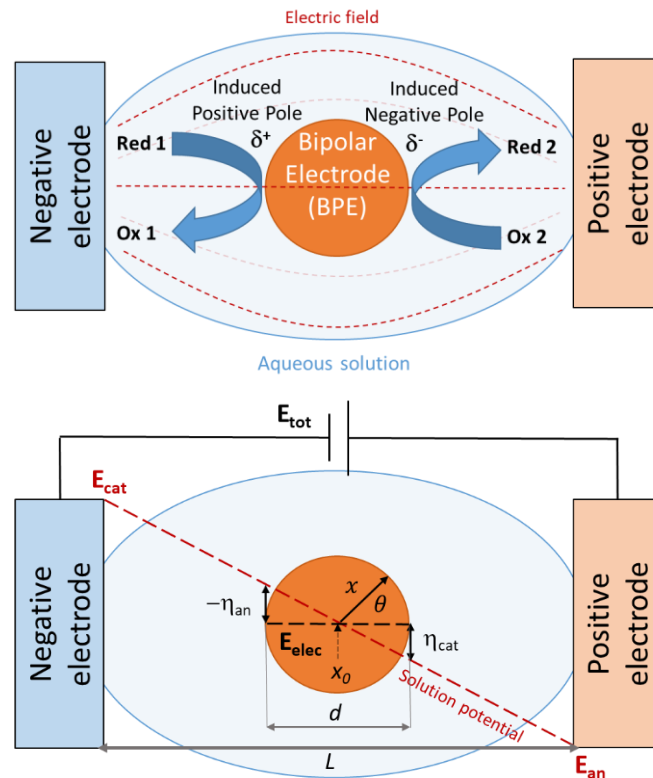


Figure 1-5 Schematics of a bipolar electrochemical system (BES), with feeder electrodes (FEs), bipolar electrodes (BPEs) and aqueous electrolyte solution.

Many design parameters are responsible for controlling bipolar electrochemical processes. These include the potential applied to the system (E_{tot}), the distance between the FEs (L), the length or diameter of the BPEs (d), the resistance of electrolyte used, and the cell setup.

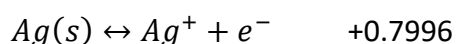
The proportion of E_{tot} that is dropped over the BPE can be described as E_{elec} . This can be calculated using Equation (1-5). It is important to note that this assumes a linear electric field: meaning the geometry of FEs is the same and that the BPE is not significantly affecting the electric field. As seen in Equation (1-5), the applied potential drop is dependent on the distance between FEs (L)

and the diameter of BPEs (d). This means that theory expects smaller BPEs to require larger potentials to drive a redox reaction.

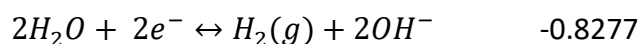
$$\Delta E_{elec} = E_{tot} \left(\frac{d}{L} \right) = \eta_{an} - \eta_{cat}$$

Equation (1-5)

In order for an electrochemical reaction to take place, this potential drop ΔE_{elec} must exceed the difference between standard redox potentials of the anodic and cathodic reactions. An example present in this thesis is the redox of Ag to generate Ag microwires (Ag MWs). As seen in Equation (1-6) and Equation (1-7), to drive this reaction ΔE_{elec} must exceed ~ 1.63 V.



Equation (1-6)



Equation (1-7)

1.2.3.1. Applications of Bipolar Electrochemistry

First applications of bipolar electrochemistry^{90,95-97} in the 1960's⁹⁸, include electrosyntheses⁹⁹⁻¹⁰¹, photoelectrochemical cells^{102,103} and batteries¹⁰⁴. In the last decade, the field has been revitalised with the number of publications almost quadrupling¹⁰⁵. This has brought a host of novel applications in diverse areas, particularly at the micro and nano-scale^{95,106,107}.

Bipolar electrochemistry is a promising alternative to traditional electroless techniques for selectively modifying micro- and nano-scale objects. The

technique has been used to create solid state and molecular gradients¹⁰⁷, as well as to create 'Janus' particles¹⁰⁸. Such techniques may have interesting applications in sensing and characterisation. As well as surface modification, bipolar electrochemistry may also be used to fabricate micro wires^{109–112} or functionalise pores¹¹³, which could have applications in creating integrated circuits.

BPEs are also favourable in microfluidic applications and have been paired with a technique termed dielectrophoresis in order to sort and separate particles and biological cells. This technique is especially interesting in cancer applications as it may be used to sort healthy cells from cancer cells¹¹⁴.

Due to both reduction and oxidation reactions occurring at the BPEs poles, bipolar electrochemistry has also been used to propel micro and nano-sized objects^{115,116}. Termed 'micro-swimmers', these particles are propelled forwards by the deposition and dissolution of metals. Again, this could have useful applications in fabricating electronics, or surface patterning.

Bipolar electrochemistry is an attractive technique in sensing and screening due to its ability to evaluate a large number of electrodes simultaneously. This allows for multiple detections to be carried out at once using a single pair of FEs. Such analytical applications make up a large area of the field and have been developed for both chemical and biological analytes. Examples have been recently extensively reviewed^{105,117}.

Biological applications of BPEs have been used for the detection^{118,119}, imaging¹²⁰, capture^{114,121,122} and lysis¹²³ of living cells or cellular content. Examples include enzymatic systems, which exploit enzymes to convert target analytes into redox active or optically active species^{124–126}, and DNA based sensors, which harness single-stranded DNA (ssDNA) to detect the complementary sequence through DNA hybridization^{127–131}. Many of these biological applications use closed bipolar systems, in order to separate the sensing and reporting reactions. Most applications focus on the surface of cells or require the lysis of cells in order to analyse the intracellular content. One less invasive example of probing the intracellular space involves piercing individual cells in order to sense hydrogen peroxide, glucose or SMase¹³². An advantage of bipolar electrochemistry is its capability to wirelessly probe electrodes; hence it is an obvious next step to develop intracellular BPE sensors (open systems) that are capable of wirelessly probing the intracellular space. By exploiting both the wireless nature, and high throughput capabilities of bipolar electrochemistry, we may develop novel non-invasive intracellular sensors¹³³, that could create the new sensing paradigm needed to advance modern medicine and the field of bioelectronics¹³⁴.

Many sensing and analysis applications of bipolar electrochemistry rely on light-based readouts such as electrochemiluminescence^{125,135,136} and fluorescence^{137,138}. These readouts may be visualised using microscopes, cameras¹³⁹ or even smart phones^{140,141}. Alternatives include a change of

colour^{118,142}, potential/current measurements^{143–145}, electromechanical actuation^{146–148}, or the dissolution of metals^{149–152}. The manufacture of electrode arrays for these high-throughput sensing and analysis applications may be performed using photolithography^{125,135}, screen printing^{153,154} and inkjet printing¹¹² as shown here-in.

1.2.4. Electrochemical Impedance Spectroscopy

Electrochemical impedance spectroscopy (EIS) is a tool used to measure impedance. The relationship between voltage (V) and current (I) in an ideal conductor can be described by Ohms Law. Ohms Law states that the potential difference is proportional to the current through it. This proportionality constant is resistance in direct current and impedance in alternating current. Hence, we can state that impedance is a resistive component, which takes frequency variation into consideration. To understand this further, we can consider three ideal circuit components: a resistor, an inductor and a capacitor.

A Resistor

An ideal resistor is purely resistive, giving a real impedance and therefore does not introduce any phase shift to the applied voltage. This means it follows Ohms Law with resistance being V/I .

An Inductor

An ideal inductor consists of a 'solenoid' or coiled wire as seen in Figure 1-6. The flow of current through the wire generates a magnetic field around the wire; these small magnetic fields create a larger magnetic field within the solenoid from one end to the other. When current alternates this causes a change in the magnetic field which in turn causes an induced current to flow, opposing the main current and therefore generating a resistive component deemed Inductive Reactance (X_L). Hence, an inductor again follows ohms law, but with the proportionality constant being inductive reactance. An ideal inductor is purely reactive, giving an imaginary impedance, which therefore introduces a phase shift to the applied voltage.

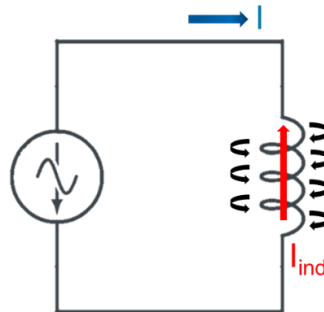


Figure 1-6 Schematic showing magnetic field that forms around a solenoid causing an impedance to the flow of current.

A Capacitor

An ideal capacitor consists of two conductive plates facing one another, with a resistive or dielectric material between them. Electrons flow to one of the plates, consequently repelling electrons on the other plate. As electrons build

up on the negative plate, they will also repel further electrons from joining them over time, causing a resistance to the flow of current deemed Capacitive Reactance (X_C). Due to this, capacitive reactance behaves in the opposite manor to inductors as a function of frequency i.e., as frequency increases capacitive reactance decreases due to there not being enough time for electrons to build up and repel one another. Again, an ideal capacitor is purely reactive and hence introduces a phase shift.

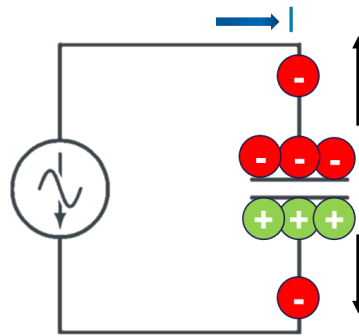


Figure 1-7 Schematic of an ideal capacitor, electrons (-) build up and repel like charges from flowing to the plate. This also repels like charges on the opposing plate (+), forming positively charged atoms. The more charge that builds up, the more current is impeded.

As inductors and capacitors introduce a phase shift to the applied voltage, in order to calculate their impedance their reactance cannot simply be added to resistance. Instead, considering the phase diagram in Figure 1-8, the following equations stand due to the Pythagoras theorem:

$$Z = \sqrt{R^2 + X^2}$$

$$\text{where } X = X_L - X_C \text{ and } \tan\phi = \frac{X}{R}$$

Equation (1-8)

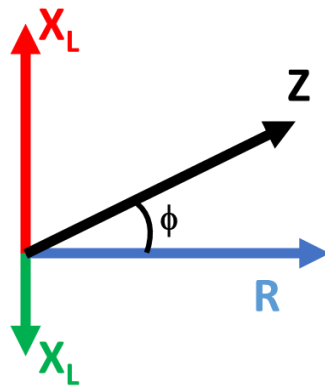


Figure 1-8 Phase diagram showing inductive reactance X_L , capacitive reactance X_C , resistance R and resulting impedance Z . Phase angle is denoted as ϕ .

Electrochemical Impedance Spectroscopy (EIS) is a technique used to probe the impedance of a sample within a specified frequency range. A small sinusoidal excitation potential is applied, so that the cell's response is pseudo linear, and a sinusoidal current response is produced. The excitation potential, expressed as a function of time, can be seen in Equation (1-9), where E_t is the potential at time t , E_0 is the amplitude of the signal and ω is the radial frequency (expressed in terms of frequency - f). In a linear system, the response signal I_t is also a sinusoidal wave, but shifted in phase by the angle ϕ and hence expressed in Equation (1-10). Using Ohms Law, we can then calculate Impedance (Z) in terms of a magnitude Z_0 and phase shift ϕ as seen in Equation (1-11).

$$E_t = E_0 \sin(\omega t)$$

$$\text{Where } \omega = 2\pi f$$

Equation (1-9)

$$I_t = I_0 \sin(\omega t + \phi)$$

Equation (1-10)

$$Z = \frac{E_t}{I_t} = \frac{E_0 \sin(\omega t)}{I_0 \sin(\omega t + \phi)} = Z_0 \frac{\sin(\omega t)}{\sin(\omega t + \phi)}$$

Equation (1-11)

As stated earlier, we assume the cell's response to be pseudo-linear meaning the system is stable, with no reactions taking place. In order to test this, we can plot the excitation potential against the response current as seen in Figure 1-9. The sinusoidal signals produce an oval shape known as the Lissajous Figure. If the oval is not symmetrical, in the diagonal plane, then the system is not stable. Conclusions can still be drawn from non-stable measurements; however equivalent circuit fittings cannot be considered accurate. An alternative method to check the stability of a system is to use the Kronig-Kramers statistical test. Kronig-Kramers (KK) relations are used to relate real and imaginary parts of a complex transfer function, such as impedance. The KK test fits experimental data to a model circuit that satisfies KK relations; if the data can be represented by said circuit, then the data set should also satisfy KK assumptions.

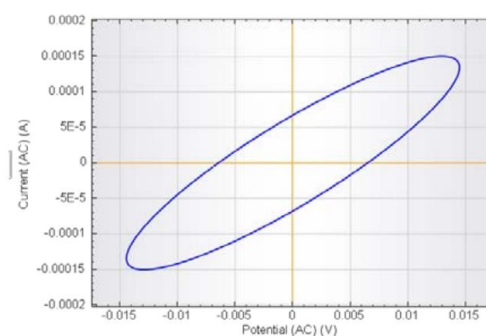


Figure 1-9 Lissajous plot showing excitation potential plotted against resulting current of an alternating current source.

1.2.5. Other Characterisation Methods

1.2.5.1. *UV visible light spectroscopy (UV-Vis)*

UV visible light spectroscopy (UV-Vis) is a non-destructive technique that can measure the interaction of a sample with light across the UV and visible regions of the light spectrum¹⁵⁵. Light is passed through a sample and a detector is used to measure the wavelength-dependant attenuation. UV-Vis is a useful tool for quality control in order to compare samples to assure they do not differ from one another. UV-Vis is also particularly useful for ‘plasmonic’ materials such as gold and silver as they have distinctive absorbance spectra that allow the determination of the size and quality of the nanoparticles from the spectra.

An Agilent Cary 60 UV-Vis spectrophotometer is used herein to confirm the synthesis of nanoparticles, comparing those synthesised with those from the protocols used. As Au NPs are also used, it may also give an idea of size of these NPs.

1.2.5.2. *Dynamic light scattering (DLS)*

Dynamic light scattering (DLS) is a non-destructive technique used to assess the size and size distribution of particles and molecules in the submicron region. The technique does this by measuring Brownian motion: the random movement of particles in a fluid due to their collisions with other atoms or molecules. The velocity of Brownian motion can then be used to determine the

size of particles: with small particles diffusing quickly and large particles diffusing slowly. The velocity of the Brownian motion is defined by the translational diffusion coefficient (D). This translational diffusion coefficient can be converted into particle size using the Stokes-Einstein Equation (Equation (1-12)).

$$d_H = \frac{kT}{3\pi\eta D}$$

Equation (1-12)

Where d_H = hydrodynamic diameter, k = Boltzmann's constant, T = absolute temperature, η = viscosity and D = translational diffusion coefficient

It is important to note that, as per the Stokes-Einstein Equation, this technique measures the diameter of a particle in relation to how it diffuses within a fluid. This 'hydrodynamic diameter' defines the diameter of a spherical particle that has the same translational diffusion coefficient (D) as the particle in the sample. This means that the exact particle size may vary slightly as other factors may alter the translational diffusion coefficient, such as particle shape, surface structure and ionic strength of the medium.

DLS measures the speed at which particles are diffusing due to Brownian motion by measuring the rate at which scattered light fluctuates. Using a suitable optical arrangement (90 or 173° detection angle), the intensity fluctuations are measured over time, with small particles causing more rapid

fluctuations than larger ones (Figure 1-10:A and C). A digital auto correlator then compares the intensity signal with itself at particular timepoints in order to plot the decay of correlation. As larger particles will move more slowly, the signal will change less rapidly than smaller particles, leading to a slower decay in the correlation of the signal (Figure 1-10:B and D). Various algorithms are then used to provide particle size from the correlogram. Other information that can be gathered from the correlogram are the mean size of the sample from the time at which the signal starts to significantly decay, and the polydispersity index (PDI) from the steepness of the decay line.

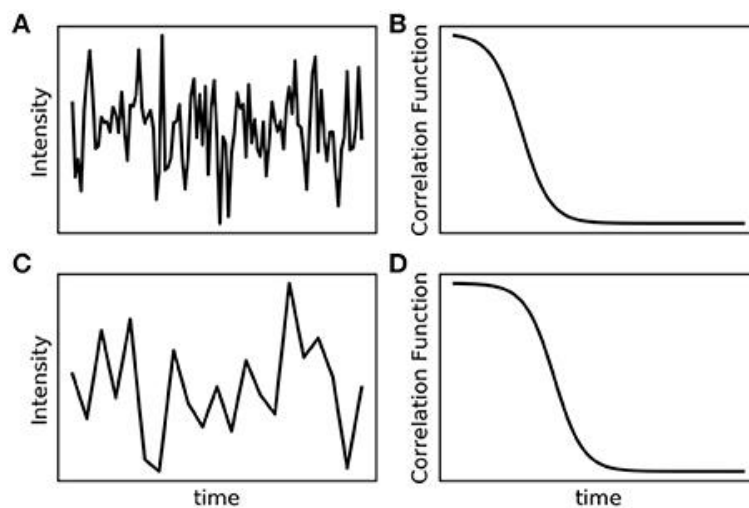


Figure 1-10 Scattered light intensity fluctuation of small (A) and large (C) particles with the corresponding correlograms (B and D). Figure taken from Carvalho et al.¹⁵⁶

DLS is an extremely useful tool for characterising nanoparticles as it is a non-destructive technique and only requires a small sample size; It also allows for a wide range of temperatures, concentrations and sample buffers to be used¹⁵⁷. DLS is a useful tool, not only concerning size characterisation, but also

confirming functionalisation, determining aggregation profiles, and characterising long-term NP stability in varying media¹⁵⁶. We used the technique here-in to characterise the size and PDI of in-house synthesised NPs, and as a quick way to confirm the functionalisation of NPs with Pd after electrical stimulation (before performing TEM studies).

For all DLS measurements within this thesis, a Malvern Zetasizer was used. Nanoparticles were suspended in dH²O in concentrations between 1 and 10 mg/ml, with 70 μ l of suspension placed into a cuvette for analysis. Samples were filtered using 0.24 μ m filters and sonicated prior to measurements.

1.2.5.3. Inductively Coupled Plasma Mass Spectroscopy (ICP-MS)

Inductively coupled plasma mass spectroscopy (ICP-MS) is an analytical technique used to measure trace elements in liquids¹⁵⁸. Elements are led through a plasma source, where they become ionised. These ions are then sorted based on their mass-to-charge ratio in order to characterise the sample's makeup. As ICP-MS can measure specific isotopes of an element, the ratio of two or more isotopes can be determined. This makes ICP-MS very useful in a wide range of applications such as biological tracer studies. ICP-MS is used herein to assess cellular uptake of Au nanoparticles (NPs).

1.2.5.4. Electron microscopy (TEM and SEM)

Electron microscopy (EM) is an imaging technique capable of imaging samples exponentially smaller than what can be seen with a standard light

microscope. Unlike light microscopy, EM uses electrons to allow us to visualise samples; a stream of electrons is focussed on a sample using various lenses, the measured interactions between the electron and the sample are then used to create an image. The two common types of EM are scanning electron microscopy (SEM) and transmission electron microscopy (TEM). The two techniques vary slightly, with SEM being thought of as providing external morphology and TEM being capable of probing internal structures¹⁵⁹.

Scanning electron microscopy (SEM), as stated in the name, produces an image of a sample by scanning an electron beam across it and measuring back scattered and secondary electrons. This technique allows for the visualisation of approximately the top 1 μm ¹⁶⁰ of many surfaces from metals to biological cells¹⁶¹. SEM is used here-in to characterise the size of nanoparticles, as it is a fast technique requiring little sample preparation.

Transmission electron microscopy differs in that a broad beam of electrons is transmitted through a sample in order to create an image. It does so by measuring electrons that are able to pass through samples, therefore samples are required to be less than ~ 100 nm thick¹⁶². TEM enables internal structures to be examined, with resolutions reaching atomic scale. Here-in we used TEM to assess electrochemical deposition onto nanoparticles, to allow for higher magnification and the visualisation of cross sections of nanoparticle BPEs. TEM was also used to image tissue sections of *Caenorhabditis elegans* (*C. elegans*).

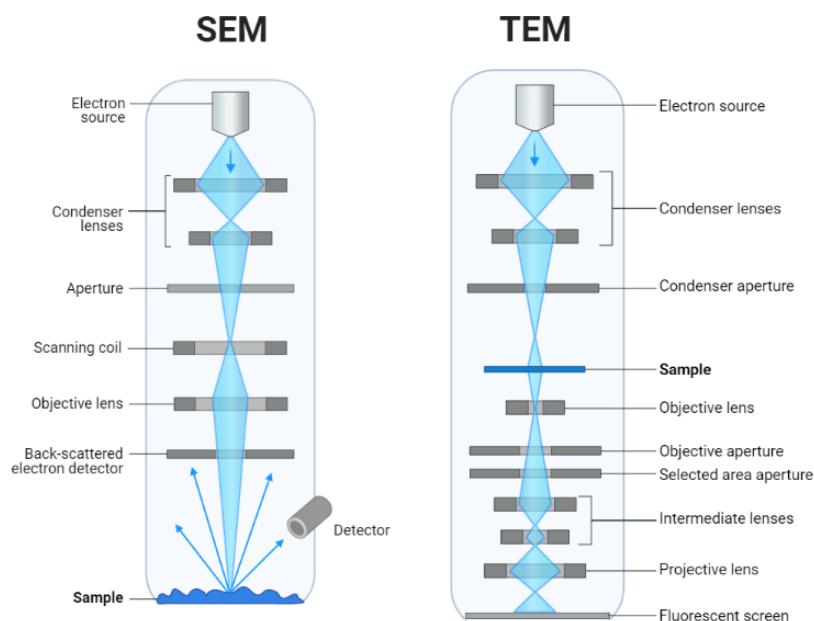


Figure 1-11 SEM vs TEM setup.

Within this thesis, SEM and TEM have been used to image nanoparticles (NPs). NP solutions were sonicated and filtered (0.24 μm filters), before being dropped and dried onto aluminium stubs or carbon grids for SEM and TEM respectively.

1.2.5.5. *Energy Dispersive X-Ray Spectroscopy (EDS)*

To further assess electrochemical deposition onto nanoparticle BPEs, EM was paired with another technique: electron dispersive spectroscopy (EDS). EDS is an analytical technique used to analyse the elemental make-up or chemical characterisation of an area of interest on a sample.

When a sample interacts with an electron it becomes ionised, this ionisation results in the production of an X-ray. EDS captures and characterises

these X-rays, producing a spectrum of X-ray intensity peaks. These X-ray intensity peaks are characteristic for each element and so can be used to determine the elements present in a sample. Elemental maps can also be produced illustrating the position of specific elements in the area analysed.

1.3.Aim and Objectives

This project aims to develop an understanding of the use of bipolar electrochemistry for growing conductive structures at the micro/nanoscale. This technique is something that has previously been discussed as having promising applications in growing nanoelectronics, however, this has yet to be merged with biology. The focus of this work is to develop a technique compatible with biology for future applications in cancer treatment. In order to do so, there are three main objectives:

- 1) Understand and optimise the wireless growth of conductive structures using bipolar electrodes, particularly with biological systems
- 2) Develop a bipolar electrochemical system that is compatible with biology
- 3) Develop understanding of bipolar electrochemistry at the nanoscale, in order to be able to develop bipolar systems for use in novel biological applications

1.4. Summary of Work

In order to address the above objectives, this thesis includes three experimental chapters, and a future work chapter as follows:

Chapter 2. Microwire growth in the presence of cells

This chapter addresses the first aim and optimises the growth of conductive structures using BPEs. The effects of BPE geometry and orientation, satellite BPEs, direct vs alternating current, and FE resistance on the growth of micro-wires is investigated. Furthermore, a 3D proof of concept is presented, growing micro-wires in the presence of 3D cell cultures.

Part of this chapter was published in Sanjuan-Alberte, P. *et al.* Remotely Controlled in Situ Growth of Silver Microwires Forming Bioelectronic Interfaces. *ACS Appl. Mater. Interfaces* **11**, 8928–8936 (2019). (Under A. J. Shaw)

Chapter 3. Development of Nano Bipolar Electrodes

This chapter develops nano BPEs that are biocompatible, therefore addressing the second aim. Multiple materials were tested for use as BPEs. Conductivity and biocompatibility were characterised, before nano particles were tested as BPEs in a simple redox reaction. Finally, NPs are assessed in conjunction with TTFs to determine whether conductive structures may be used to improve the TTF therapy.

Part of this chapter was published in Sanjuan-Alberte, P. et al. *Wireless Nanobioelectronics for Electrical Intracellular Sensing. ACS Appl. Nano Mater.* **2**, 6397–6408 (2019). (Published under A. J. Shaw)

Chapter 4. Impedimetric Characterisation of Nano Bipolar Electrodes

This chapter addresses the final aim of further understanding bipolar electrochemistry at the nanoscale. Au nanoparticles (Au NPs) are investigated using electrochemical impedance spectroscopy. Au NPs are probed with and without the presence of cells in order to determine how they behave.

This chapter was published as: Robinson, A. J. *et al.* Impedimetric Characterization of Bioelectronic Nano-antennae. *ACS Omega* (2021). (*in press*).

Chapter 5. Discussion and Future Work

This chapter discusses the entirety of this thesis and details the opportunities and limitations associated with this work. It also addresses future work, including that which wasn't completed due to the impacts of Covid-19, and long-term future work.

1.5. Contributions

[Chapter 1. Introduction](#)

Parts of this chapter have been published in Robinson, A. J. *et al.* Toward Hijacking Bioelectricity in Cancer to Develop New Bioelectronic Medicine. *Advanced Therapeutics* **4**, (2021), and Gibney, S. *et al.* Toward nanobioelectronic medicine: Unlocking new applications using nanotechnology. *Wiley Interdiscip. Rev. Nanomedicine Nanobiotechnology* (2021); hence, I would like to thank all authors for their contributions to this work.

[Chapter 2. Microwire growth in the presence of cells](#)

I would like to thank Nicola Lacalendola and Geoff Willmott from The MacDiarmid Institute for Advanced Materials and Technology, Department of Physics and Chemistry, The University of Auckland, for their contributions towards mathematical modelling included in Figure 2-9.

[Chapter 3. Development of Nano Bipolar Electrodes](#)

I would like to thank Dr Akhil Jain and Dr Craig Stopiello for their contributions in SEM and TEM imaging of Au and PPy NPs.

Chapter 4. Impedimetric Characterisation of Nano Bipolar Electrodes

I would like to thank Dr Akhil Jain for his contribution towards AuNP cellular uptake studies as seen in Figure 4-8. I would also like to thank both Dr Akhil Jain and Dr Saul Vazquez Reina for their contribution towards performing ICP-MS.

Chapter 5. Discussion and Future Work

I would like to thank and acknowledge Dr Veeren Chauhan for his contribution towards all nematode work. Additionally, Dr Zubair Nizamudeen and Dr Christopher Parmenter for their contributions towards imaging *Caenorhabditis elegans*.

Chapter 2. Microwire growth in the presence of cells

Aim: Understand and optimise the wireless growth of conductive structures using bipolar electrodes, particularly in the presence of biological systems

The ability to grow conductive structures in the presence of biological systems could have great impacts in sensing and actuating biological behaviour. Additionally, there is scope to improve TTF based therapies by targeting the electric fields to a tumour site. A previous example exists of growing Ag microwires (MWs) in the presence of 2D monolayers of cells¹¹². This chapter expands on this method to improve understanding and control of MW growth using BPEs.

Initially, bipolar electrochemical system (BES) design is studied, showing that BPE geometry and orientation can be harnessed to control wire growth direction. Wire growth with alternating current is then pursued; this allows for lower potentials to be used (as low as 50 V, 0.5 V/cm) and finer wires to be grown (as low as 0.5 μm). Finally, novel proofs of concept are presented, showing Ag MW growth in the presence of 3D cancer cell spheroids (U251 glioblastoma cells) and Au MWs grown using a metal salt (AuCl). These show promise for using this method to wirelessly grow electronics *in vivo*.

2.1. Introduction

The manufacture of micro and nanoscale electronics holds great promise for a wide range of applications, in particular bioelectronic medicine¹⁶³. The ability to easily manufacture electronics of an equivalent scale to cellular components could not only allow for better integration between the electronics and biological structures, but also permit innovative applications requiring the targeting of specific electrical relays in tissue¹⁶³. Furthermore, there is scope to improve existing electrical stimulation therapies, such as tumour treating fields (TTFs), by targeting the electric field to a tissue site.

Current micro and nanoscale electronics are mostly manufactured using complex layering processes or 3D printing techniques: primarily extrusion printing or direct ink writing^{84,164}. Although these processes can now provide flexible electronics to be wrapped onto biological material¹⁶⁵, by pre-assembling electronics before their incorporation with biology the interface between both systems is poor¹⁶⁶: only providing a 2D connection across a surface. The ability to self-assemble 3D electronics in-situ not only increases the information processing density of the electronics, but may also greatly improve the integration with biological tissue.

Self-assembly of 3D electronics has previously been shown using a range of materials and techniques such as: assembly of colloidal particles^{167–169}, electrodeposition¹⁷⁰ and electrochemistry^{109,111,171–176}. In order to be able to

merge such techniques with biology, a wireless, and therefore less invasive, approach is desirable. This is possible using bipolar electrochemistry^{90,106}. Bipolar, or wireless, electrochemistry has been used previously to grow microwires (MWs)^{109,111} without the presence of biological systems. We have shown wireless MW growth in the presence of cells (2D monolayers) to be possible using micro-BPEs stimulated under direct current (DC) at ~ 90 V (0.9 kV/cm)¹¹². However, only $\sim 50\%$ of cells were viable after MW growth with this increasing to 100% at the negative electrode. No other research group has merged this method with biological systems due to high potentials or harmful solvents being used. One other example exists using electrochemistry to grow MWs to interface with individual cells¹⁷⁷. Nevertheless, the method is not wireless, with the distance between electrodes being <30 μm and so having limited applications in *in vivo* bioelectronics.

A number of challenges must be overcome in order to use this method to grow conductive structures for *in vivo* bioelectronics. These include improving the control of MW growth (particularly in a 3D space) and reducing the aforementioned cytotoxic effects. This chapter aims to address these challenges by optimising and understanding MW growth and the effect of BES design (i.e., geometry, orientation and size of BPEs) on MW growth and optimising MW growth using AC current. The first 3D proof of concept model with cells is then presented, along with a proof of concept for wireless MW growth from an injected metal salt.

The hypothesis is that MW growth may be somewhat controlled or directed by harnessing BPE geometries and orientation. Our previous study highlights the effect of FE geometry on MW growth¹¹²; however, to our knowledge, no other research group has investigated the effect that BPE design may have on MW growth. Thus, herein we assess the effects of BPE geometry and orientation, as well as the inclusion of micro- 'satellite BPEs'.

A second hypothesis is that using alternating current may allow for varying electrical inputs to be used to grow MWs; this may allow for wire growth to be more compatible with biological systems. A number of studies exist using AC to elicit electrochemical MW growth^{172,176}, with only one being wireless¹¹¹. This study grows polymer MWs with the application of 18 V (~60 V/cm) at 5 Hz; hence, herein a broader study of varying frequencies is performed.

Other systems grow MWs from the addition of metal salts^{172,175}, however these methods are not wireless. Wireless MW growth has been performed using a monomer, or using metal BPEs that partake in oxidation and reduction reactions to provide the material for MWs^{109,112}. In order for FEs to be *ex vivo*, it is necessary that the constituents needed to grow MWs are not sourced from the FEs. Hence, the final section of this chapter presents a wireless proof of concept growing Au MWs from the addition of AuCl.

2.2. Methods

2.2.1. Electrode manufacture

Simple feeder electrodes were required to develop self-assembled electronics. Inkjet printing was chosen to produce these simple electrodes, as the technique allows for microscale resolution and the pattern can be easily altered. A piezoelectric drop on demand Dimatix Materials Printer (Model DMP-2800, FUJIFILM, Dimatix, Inc. Santa Clara, CA) was used, as described in Section 1.2.1. Glass substrates were used, either in the form of glass slides (76 x 26 mm Cole-Parmer) or glass coverslips (for Innovitro™ studies, Ø22mm Agar Scientific). Inks were filtered using HPLC Nylon 5 µM syringe filters (Cole-Parmer), before being injected into print head reservoirs. Glass substrates were cleaned using Piranha solution (1:3 ratio of hydrogen peroxide to sulphuric acid, H₂O₂:H₂SO₄) before printing.

To allow for optimal wetting of the inks and stability in aqueous solutions, a polymer was first printed onto the glass as an adhesion layer¹¹². A tri(propylene) glycol diacrylate (TPGDA) ink was used, which had been modified to polymerise under UV light¹⁷⁸. For this purpose, a UV light was mounted onto the print head (365 nm and 6000 mJ cm⁻², Printed Electronics Ltd.). To prevent any unwanted polymerisation inside the cartridge, the reservoir was covered in duct tape. Ag nanoparticle (AgNP) ink (Advanced Nano Products Ltd.) with an approximate solid content of 30% was used for printing

conductive tracks, which sinters under heat. An in-house heated substrate was used to heat the ink to 100°C during printing. Full sintering was then performed afterwards using an oven at 200°C.

Five layers of TPGDA were printed to allow for a flat surface. Three layers of AgNP ink were printed to improve conductivity, yet still allow for a short print time. To allow optimal resolution of electrodes, between one and three nozzles were used for printing Ag. However, to reduce print time, up to seven nozzles were used when printing simple square TPGDA adhesion layers.

Waveforms used for each ink were previously optimised and can be seen in Figure 2-1. Print resolution was 846.67 drops per inch, corresponding to a drop spacing of 30 μm . The firing voltage varied over a range of 24–30 V.

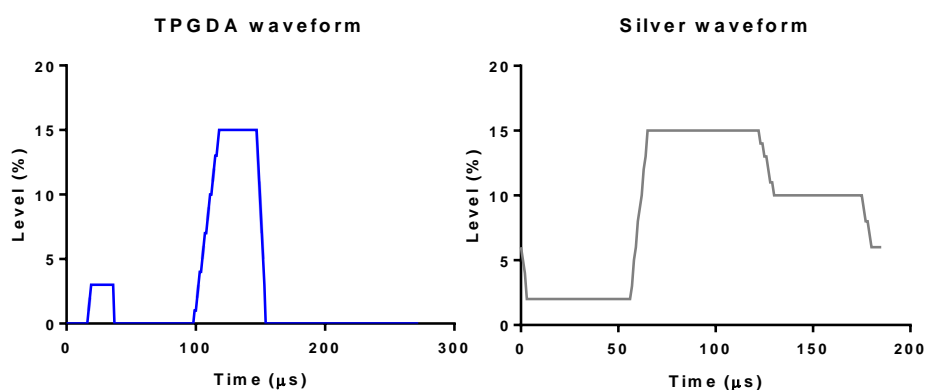


Figure 2-1 Jetting waveforms for printing TPGDA and Silver using piezoelectric drop-on-demand printer (Dimatix).

To determine whether geometry could be harnessed to control MW growth, BPE geometry and then orientation was varied. As seen in Figure 2-2:A,

four geometries of BPEs were studied, prior to six geometries being used to study the control of wire growth (Figure 2-2:B). All electrode patterns were designed using GNU Image Manipulation Program (version 2.8.16).

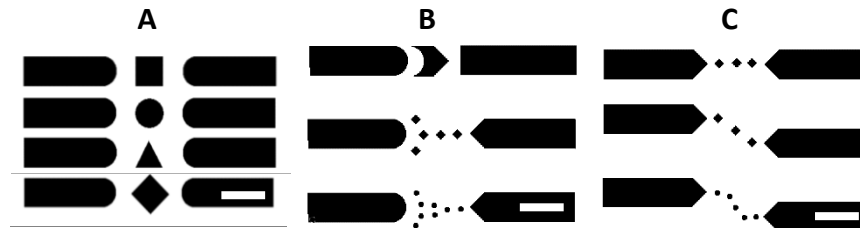


Figure 2-2 Patterns used to print varying BPEs, used to study the effect of BPE geometry (A) and orientation (B and C). FEs are 1.5 mm thick, with a 3 mm gap between them. BPEs seen in (A) have an approximate area of 1.5 mm². Scale bars represent 2.5 mm.

2.2.2. 3D Printing characterisation

3D printing conditions were optimised and characterised using light microscopy (Nikon ECLIPSE TE300 fluorescent microscope). Individual ink droplets were characterised on glass substrates and on top of layers of other inks. Dot arrays were printed for each condition, with 25 drops measured for analysis.

2.2.3. Finite element modelling of electric fields

Finite element method modelling was carried out using COMSOL Multiphysics 5.2 with the Electrostatics package. In each simulation, electrodes were separated by 1 mm, and each electrode was 1.5 mm (side length or diameter), to match printed BPEs seen in Figure 2-2:A. A positive potential of 90 V was applied to the left electrode, and the right acted as a ground.

2.2.4. Electrochemical wire growth

Ag wire growth was carried out in deionized water by applying varying electrical inputs with a high voltage stimulator (HVS – EC100SA NF Instruments). As seen in Figure 2-3, wire growth was imaged in real time using a Nikon ECLIPSE TE300 fluorescent microscope equipped with QImaging optiMOS Scientific CMOS camera. To improve electrical contact between the power source (a high voltage stimulator - HVS) and printed electrodes, silver paint (RS components) was applied to the 3D printed samples and disposable needles (20 gauge, Merck) were used to attach samples to crocodile clips.



Figure 2-3 Wire growth set up, using optical microscope, high voltage stimulator (HVS), Ag paint contacts and needle electrodes.

Au wires were grown using the same set up, however the addition of AuCl was required to provide the wire material. 10 mM AuCl in dH₂O was used.

Wires were characterised using a wireless TRMS multimeter (Extech Instruments) to measure resistance and imageJ to measure wire diameter from microscopy images (ten random measurements were taken from each sample).

2.2.5. Cell culture – monolayers and 3D cell cultures

Due to the relevance of cancer to this thesis, human glioblastoma cells (U251's, ATCC) were cultured in T-75 flasks in 15 ml of Dulbecco's modified Eagles high glucose medium (supplemented with 10% FBS) for 2-3 days at 37°C and 5% CO₂ and passaged when 70-80% confluent.

To culture monolayers onto 3D printed electrodes, Ibidi sticky slides were cut up and attached to electrodes to create cell culture wells of 1cm² in growth area (Figure 2-4). Electrodes intended for cell culture were plasma cleaned and silanized to increase adhesion of printed structures and prevent them from detaching when immersed in an aqueous solution. Glass slides were soaked in ethanol for 10 minutes prior to O₂ plasma cleaning. Glass slides were then placed into the plasma chamber between two copper band electrodes connected to a power source (Coaxial Power Ltd.). The chamber was evacuated, and needle valves (BOC Edwards) were used to control the oxygen pressure. Pressure was monitored with a Pirani gauge (Kurt J. Lesker Ltd.) and a glow-discharged plasma was initiated when the pressure was stabilised to 9x10⁻² Mbar (50 W for 3 minutes). Next, salinisation was performed using 1% 3-(Trimethoxysilyl) propyl methacrylate (TMSPMA) (Sigma-Aldrich) in toluene for an hour, before washing with dH₂O. Cells were seeded at approximately 5 x 10⁵ cells per well in 300 µL of culture media. Immediately before wire growth

media and sticky slides were removed, samples were washed with PBS and substituted with a droplet of deionized water.

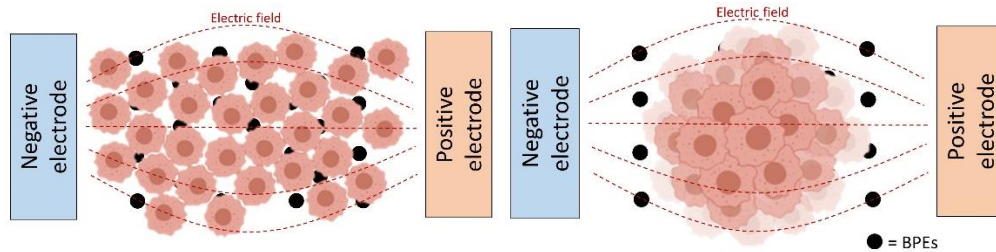


Figure 2-4 Wire growth set up with cells for 2D monolayers (left), and 3D spheroids (right). BPEs consisted of single ink drops of $\sim 50 \mu\text{m}$. Ibidi sticky-slides were used to contain media in $10 \times 10 \text{ mm}$ areas around cells. Distance between FEs was equal to 1 mm.

3D spheroids were cultured using a Rotary Cell Culture System (RCCS, Synthecon). Cells were introduced into the disposable 10 ml culture vessels for 3-4 days and rotated at varying speeds to ensure spheroids were in a constant state of free-fall (i.e., balancing the forces of gravity and Coriolis). Spheroids were then characterised using light microscopy (Nikon Diaphot 300). In order to perform wire growth, cultured spheroids were washed in PBS and placed between 3D printed electrodes. Deionized water was then added, covering the spheroid.

2.3. Results and Discussion

With the aim of producing a bipolar electrochemical system (BES) that enabled the growth of nano-electronics in combination with living cells, 2D FEs and BPEs were designed. Silver nanoparticle (AgNP) ink is widely characterised for research purposes¹⁷⁹ and allows for reproducible 3D printing of electrodes^{180,181}. Silver (Ag) electrochemistry also allows for simple reduction and oxidation in deionised water, with the application of potential as the driver (Figure 2-5). Previous studies have also shown Ag to be suitable for wirelessly growing electronics with cells¹¹². Due to this, Ag was chosen for all proof of concept studies. As seen in Figure 2-5, these simple BESs are used to model electrodes for future *in vivo* applications; BPEs model electrodes that would be *in vivo*, whilst the FEs model stimulation electrodes that would be *ex vivo*.

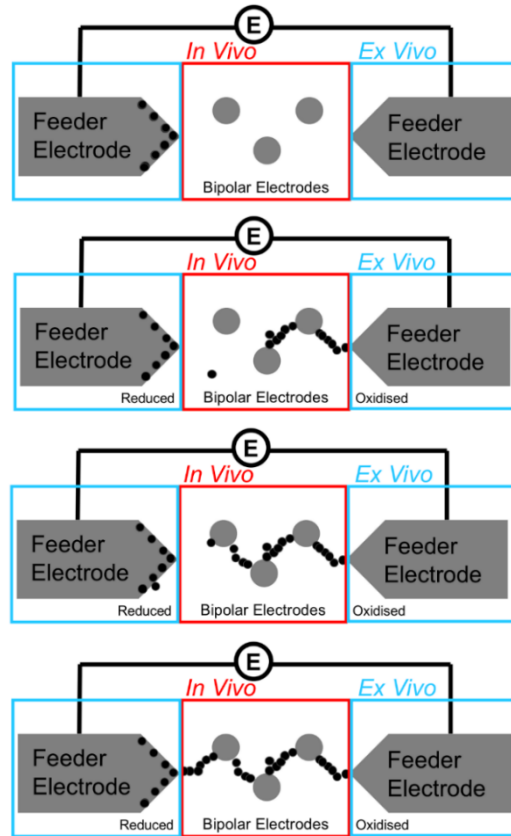
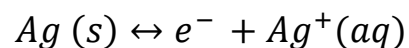


Figure 2-5 Wire growth mechanism using Ag as a simple proof of concept. For end application, BPEs model electrodes that would be *in vivo* (red) whilst FEs would be *ex vivo* (blue).

As noted in Equation (2-1), the application of potential causes the printed Ag solid to lose an electron, and therefore form an ion in solution. This ion then regains an electron and deposits to form wires. This process can be seen in Figure 2-5 and continues to form complete wires from FE to FE. Although this system relies on the printed Ag structures to form wires, the ultimate goal is that the FEs will be *ex vivo*, whilst BPEs would be *in vivo*, and hence the addition of a metal salt or conductive monomer would be necessary; this will be discussed in section 2.3.7. It is important to note that Ag would not be used for future *in vivo* applications due to its toxicity.



Equation (2-1) Silver redox equation

2.3.1. 3D printing optimisation and characterisation

Before studying the BESs design, it was necessary to optimise 3D printing to produce high resolution electrodes. A previously published method provided a starting point for this, printing TPGDA as an adhesion layer and then multiple Ag layers¹¹². The waveforms used for printing can be seen in Figure 2-1.

To confirm the above method was appropriate, ink droplet size was characterised for both inks on varying substrates. Ag ink was printed with and without a heated substrate on glass, Ag and TPGDA. TPGDA was also printed on glass, Ag and TPGDA. A smaller droplet size is desirable to allow for better resolution printing. As seen in Figure 2-6, the heated substrate allowed some solvent to be evaporated during printing and therefore provides a smaller droplet of ~50 μm instead of ~70 μm . Due to this, the heated substrate was also used to print the droplets on varying substrates. Printing Ag on Ag increases the droplet size slightly to ~60 μm . As this was only a 20% increase, future prints included multiple Ag layers to increase conductivity. Samples are to be submersed in liquid for later experiments, hence an adhesion layer is required. Droplet size confirms TPGDA is suitable for this application as it also allowed for a low droplet size of ~40 μm on glass and ~50 μm on TPGDA. TPGDA was also printed onto Ag to determine if it could be used to print insulating

layers. A great increase in droplet size to $\sim 130 \mu\text{m}$ suggests TPGDA cannot be used for this purpose, as it will not allow for accurate printing of patterns.

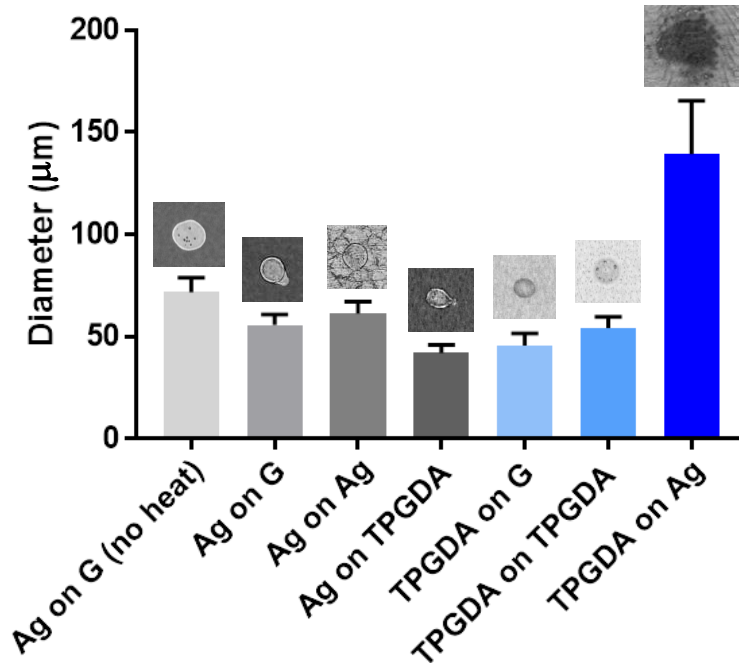


Figure 2-6 Silver (Ag) and TPGDA ink droplet diameter on varying substrates: Silver (Ag), Glass (G) and polymer adhesion layer (TPGDA). Error bars represent standard error mean (SEM), $n = 25$.

Despite using printing parameters (firing voltages, waveforms, sintering temperatures, print head height etc.) that had been previously optimised¹¹², print quality differs due to multiple avenues of variation. These may include: varying printing environment, such as fluctuations in temperature and humidity; ink variation, such as contaminants or stability changes; print head degradation, such as nozzle blockages and sintering variation, due to inconsistent heating of samples or different equipment being used. Despite quality control checks performed regularly, variation in prints was still prevalent. Visual quality issues were easily identified allowing samples to be

removed from experimental use; however, non-visual issues were easily missed, causing inconsistent experimental results. The most impactful outcome of poor-quality prints was presented in the electrode's conductivity.

To study this effect nearly 100 electrodes, printed using the same parameters, were evaluated for their conductivity and ability to grow MWs. As seen in Figure 2-7:A and B, approximately 80% of electrodes were of satisfactory quality: possessing a FE resistance of less than 100 Ω .

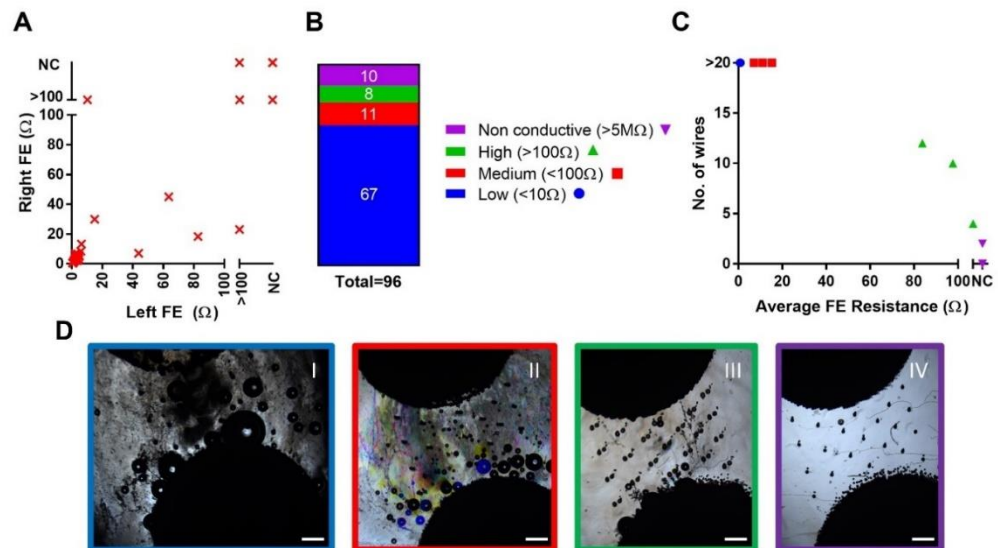


Figure 2-7 3D printing variation, characterised by FE resistance variations. A: Resistance of pairs of FEs. B: Measured samples were then categorised based on their highest resistance electrode of the pair. C: Number of wires grown for 3 samples from each category. D: wire growth examples for low (I), medium (II), high resistance (III) and non-conductive (IV).

These results were then correlated with the electrodes ability to electrochemically grow MWs. As seen in Figure 2-7:C and D, FE resistance directly affects wire growth, with poor quality electrodes (with resistances

greater than 100 Ω) growing less wires than those of satisfactory quality. Not only did this highlight the importance of quality checking electrode conductivity, but this also suggests the resistance of FEs could be manipulated to alter wire growth yields.

Using these optimised print conditions and quality control steps, a better understanding of the design implications of these BESs in terms of BPE geometry, size and orientation, was next explored.

2.3.2. Harnessing BPE geometry

The hypothesis states that effects of BPE geometry on wire growth may be harnessed in order to control the wire's direction of growth. This would be useful for *in vivo* applications, in order to direct the wires to an area of interest. To test this hypothesis, varying shapes of BPEs were printed to determine the effect of their geometry on wire growth. A previous study showed that round FEs allow for wires to be grown along the entire electrode area¹¹². Therefore, to maximise the chance of wire growth, and study only the effect of varying BPE shape, rounded FEs were used in all experiments. Similar area BPEs were used, as in the previous study, of approximately 1 mm² with a 2 mm gap between FEs. Samples were printed using standard printing conditions detailed in section 2.2.1.

As seen in Figure 2-8, wire growth was possible with all shapes of BPE. Square and circular shaped BPEs grew multiple wires across their surface,

whilst triangular and diamond shaped BPEs focused wire growth at their corners. As per Equation (2-2) and Equation (2-3), this behaviour is expected because a smaller volume with higher charge density will possess an enhanced electric field at that point. This means that electrodes with points, rather than smooth/rounded edge, will possess improved MW growth due to an enhanced electric field at their points.

$$\nabla \cdot E = \frac{\rho}{\epsilon_0}$$

Where E = electric field, ρ = charge density and ϵ_0 = permittivity

Equation (2-2)

$$\rho = \frac{q}{V}$$

Where q = charge and V = volume of electrode

Equation (2-3)

To further demonstrate this, electric fields were modelled around a square, circle and triangle, as seen in Figure 2-9. This demonstrated how geometry changes affect the density of the electric field. With dark red and blue areas being those with the highest/lowest electrical potential respectively, these are the areas where we would expect wire growth to propagate from/to. As seen in Figure 2-9, this would be across the entire flat/curved surface of a square/circle electrode, or from point to point of a triangular electrode. This is

consistent with experimental data that showed wire growth across flat and curved surfaces and directly from concentrated points.

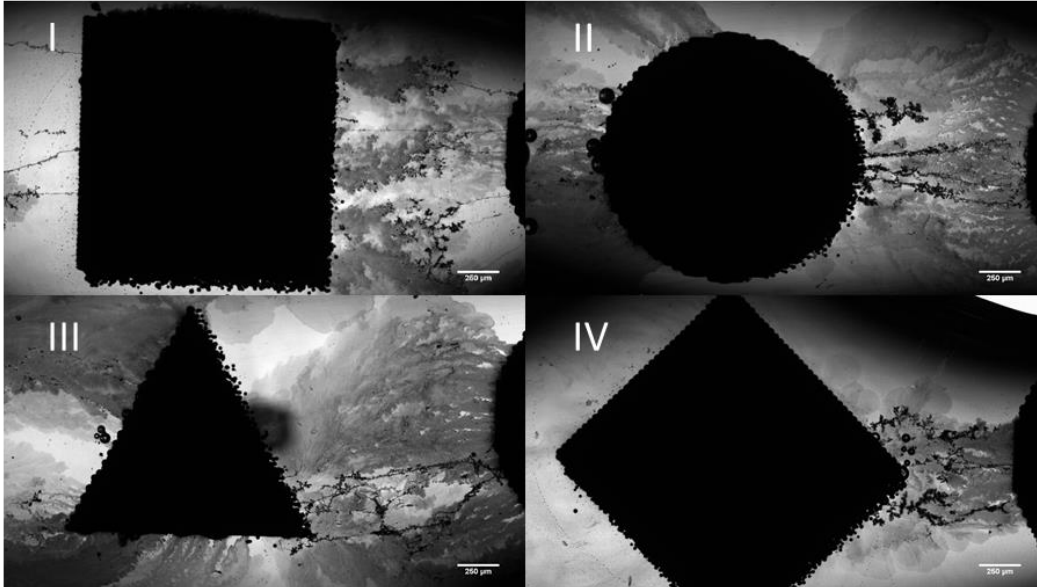


Figure 2-8 Optical microscopy images of Ag MW connections to and from a BPE in the shape of (I) square, (II) circle, (III) triangle and (IV) diamond (as per Figure 2-2 geometries). Imaged at 4x magnification with Nikon fluorescent microscope (ECLIPSE TE300), scale bars read 250 μm .

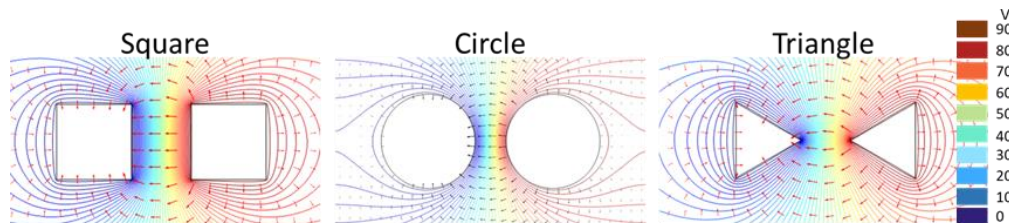


Figure 2-9 Modelled electric field and electronic potential of 90 V, applied using different geometries of FEs. Contour lines indicate the field intensity, whereas the arrows indicate the direction of the field.

It is important to characterise any effects these varying geometries have on the MWs so that they may be chosen correctly and harnessed to control MW growth in varying applications. In order to do so number of wires, resistance of

wires and wire diameter was measured. Statistical analysis was performed using one-way ANOVAs and Tukey tests. As seen in Figure 2-10, diamond shaped BPEs showed a significantly higher no. of wires than both circle and triangle BPE samples. This was likely due to the optimal orientation of high charge density areas, the two points of the diamond, across the direction of growth. This highlights the need for both geometry and orientation of said geometry to be considered when finding optimal wire growth conditions. The electrical resistance of wires showed no significant difference between most wire samples, suggesting wire formation is largely the same in each system. This important finding suggests geometry can be harnessed to direct wire growth without having detrimental effects on MW functionality (i.e., conductivity). The significant increase in resistance between circle and square geometries is thought to be due to a slight variation in the area of the circle vs. square BPEs. Wire diameter measurements also corroborated that wire growth is consistent across geometries ($\sim 3\text{--}7\ \mu\text{m}$), with no significant differences seen. If varying MW diameters are required then differing electrical inputs may be necessary, such as AC stimulation, as discussed in Section 2.3.5.

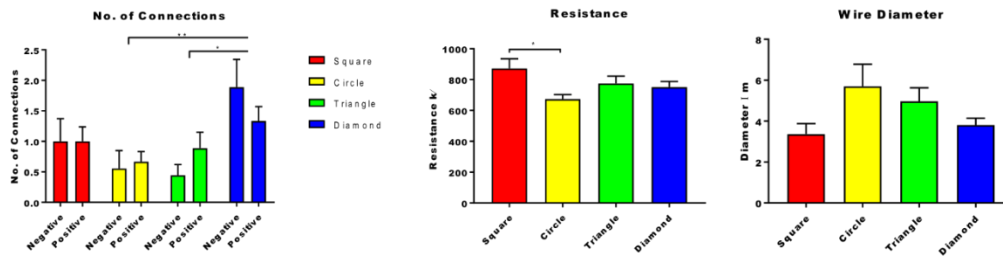


Figure 2-10 Diameter, no of connections and resistance of wires established for each geometry BPE. Error bars represent standard error of the mean (SEM), further statistical analysis was performed using one-way ANOVA with Tukey’s HSD post hoc analysis (n=9; p≤0.01).

2.3.3. Can wire growth be controlled using geometries/orientation of BPEs?

With increased knowledge of the effect of geometry on wire growth, new systems were designed to determine whether geometry could be harnessed to direct the growth of wires. As we had previously shown that wire growth is possible in the z direction¹¹², we studied the control of wire growth in the x and y direction. As seen in Figure 2-11, varying geometries and orientation does allow for some control over wire growth. Figure 2-11:A shows how curved edges could be used to fan growth across the surface, followed by a point to direct growth in a specific location. Figure 2-11:B-F show how smaller BPEs in differing orientations can be used to direct growth across the path of the BPEs rather than straight from FE to FE.

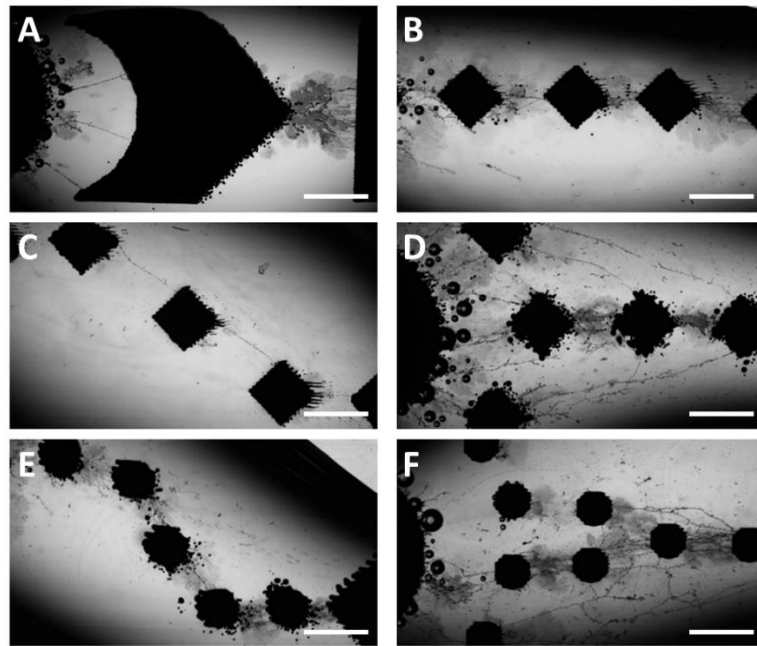


Figure 2-11 Optical microscopy images of Ag MW growth with varied geometry of BPEs and pattern demonstrating direction control of wire growth. Scale bars represent 250 μm .

From studying BPE geometry, it became apparent that samples that possessed poor quality printing, with anomalies and ink splashes, allowed for improved wire growth (Figure 2-12). These anomalies and splashes may develop when nozzles become blocked or if droplet formation is not optimal, causing the tail of a droplet to break off and form a separate droplet that collides with the initial droplet to cause splashes. Samples without the anomalies/splashes (Figure 2-12, left) provide more unstructured growth, whilst sample with the anomalies/splashes (Figure 2-12, right) appeared to provide more MWs and less unstructured growth. It is hypothesised that this is due to the smaller BPEs behaving as a point on the larger BPE¹⁸². Due to this, we then studied the impact of what we deem ‘satellite BPEs’ on wire growth.

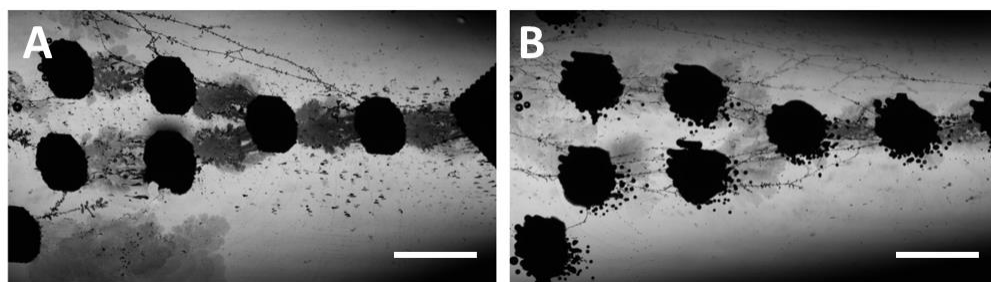


Figure 2-12 Comparison of a high quality (A) vs low quality (B) print of Ag BPEs. Scale bars represent 250 μm .

2.3.4. Satellite BPEs

In a previous study¹¹², we have shown that diamond BPEs, or rather those with a point towards the FEs, out-perform round or triangular BPEs when comparing no. of connections. An electrode point is mathematically modelled by two spherical electrodes connected by a wire¹⁸². Due to this, we hypothesise we may enhance MW growth by incorporating smaller BPEs, close to the larger BPEs, that will behave as a point off the larger BPE.

To study this hypothesis, we repeated Ag MW growth with smaller scale BPEs incorporated. The smallest BPEs possible with our electrode fabrication method (inkjet printing) are that of single ink droplets. These are approximately 30-50 μm in size. As seen in Figure 2-13:A-D, satellite BPEs were incorporated surrounding the larger BPEs, and compared to the larger BPEs alone. This study showed that incorporating satellite BPEs significantly increased the number of wires grown nearly two-fold (4 ± 1 to 7 ± 1). This finding will impact the design

of systems for the wireless growth of MWs and suggests that multiple sized electrodes should be incorporated.

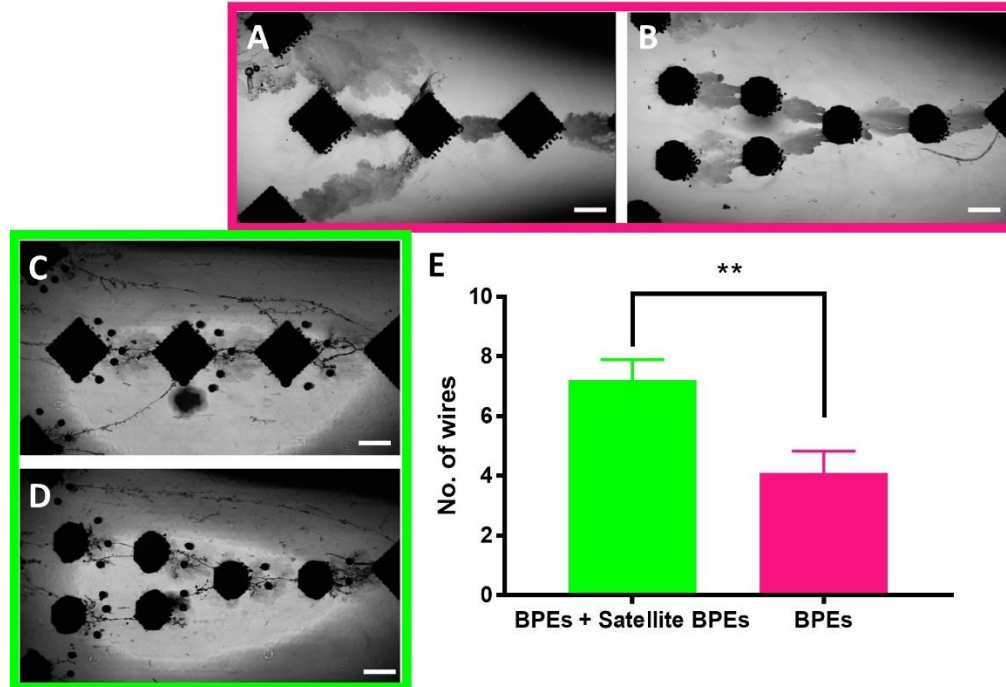


Figure 2-13 Comparison of no. of MWs grown using samples with and without satellite BPEs. Multiple geometries were used in pairs, of with and without satellite BPEs. Examples of those without (A-B) and with (C-D) satellite BPEs can be seen. Mean \pm SEM of no. of MWs grown is plotted (n = 20).

It is important to note that, while the smaller BPEs concentrate charge to act as nucleation sites for the MW growth to initiate at, the larger scale BPEs are still required to lower the overall impedance of the system and allow for lower potentials to be used to grow MWs¹⁰⁷. This, along with the above geometry and orientation studies is an important finding which could impact using this method to grow MWs out of many materials, as no other group¹¹² has investigated the effects of the FE and BPE geometries on MW growth.

2.3.5. AC MW growth

As mentioned in Section 2.1, further control over MW characteristics may be possible by using alternating current to grow the MWs. As we have previously shown, AC current may also improve cell viability¹¹² in a BES as the introduction of a frequency component may allow for alternative electrical inputs that are less harmful to cells. Tissue damage often results from water electrolysis and noxious by-products from chemical reactions¹⁸³; utilising AC stimulation may reduce this due to less charge building up. This will be important for future *in vivo* applications. AC stimulation has been used previously to grow MWs, although these also require the use of harmful agents that would not be suitable for use with biology^{172,176}. In order to optimise Ag MW growth utilising AC current, we first do so in a simple system without cells. Small single drop BPEs were incorporated between two FEs (1 mm apart), replicating previous DC studies¹¹², before then using varying potential and frequency stimulation to attempt to elicit MW growth. A high frequency bipolar amplifier was used to generate AC stimulation. As previous Ag MW growth was possible at 90 V (0.9 kV/cm), a potential range of 10 to 100 V (0.1 – 1 kV/cm) was chosen. The entire frequency range capable with this equipment was investigated (1 Hz to 1 MHz).

As seen in Figure 2-14, MW growth was not possible using 10 V at any frequency. MW growth was also not possible using 1 kHz frequency at any potential, the reason for this is still unknown. As seen in Figure 2-14, insets I to

VI, varying frequencies produce markedly different MWs. At frequencies ≤ 100 Hz, broken MWs form that are of low diameters of 0.5-1 μm : these MWs form when using 100 V, or if applying 100 V for 2 seconds before then lowering to 50 V. They radiate from both FEs but break off before meeting in the middle, reaching lengths of between 100 and 300 μm . This is most likely due to the extremely fine nature of the MWs, and the forces caused by the slow alternating of the current.

Higher Frequencies ≥ 10 kHz initially produce thicker MWs, with large amounts of unstructured growth. Thicknesses gradually decrease, becoming less unstructured to ~ 1 μm at 1 MHz. This proportionality of decreasing thickness at higher frequencies is comparable to AC MW growth using other materials^{175,176}, although wire thickness is magnitudes larger. These MWs can be described as complete, rather than broken, in that they grow to span the entire space between the FEs. Similar to lower frequencies, those between 10 and 100 kHz allowed for MWs to be grown at 50 V when applying 2 seconds of 100 V to initiate the MW growth. Additionally, increasing the frequencies allowed for MWs to be grown using the application of lower potentials, with 1 MHz producing fine MWs at 50 V, 100 kHz growing MWs between 60 and 70 V, and 10 kHz growing MWs between 80 and 90 V.

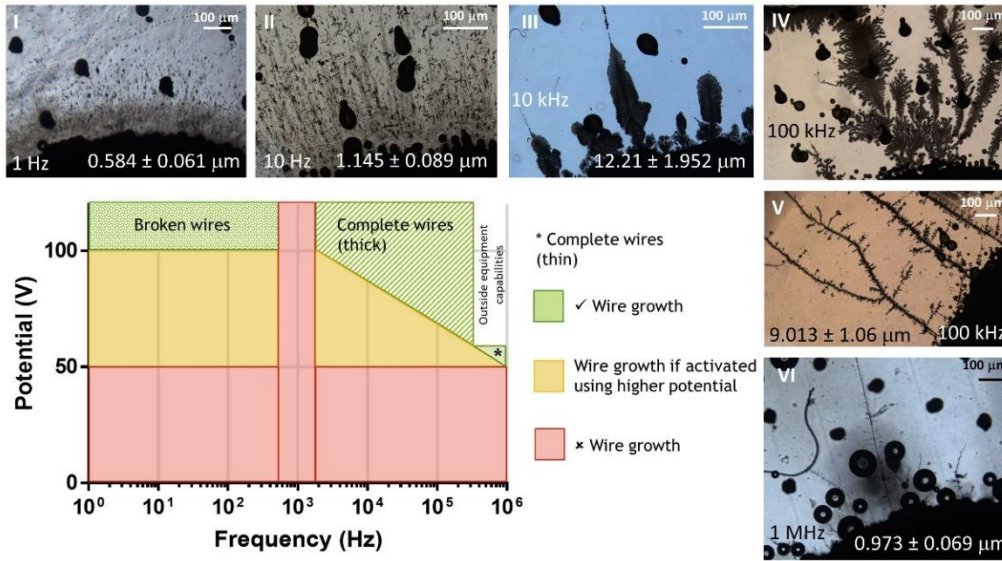


Figure 2-14 AC MW growth attempted at varying frequencies and potentials. Characteristic wires for varying frequencies at 100 V (or 50 V at 1 MHz) can be seen in images I-VI.

These results are useful for future bioelectronic applications, whereby choice of wire diameter (\varnothing) may be important to interface with specific cells or cellular populations. Wire \varnothing also determines electrical resistance, and hence specific wire sizes may be needed depending on the eventual electrical inputs to be used with them. As well as \varnothing , higher frequencies also affect wire branching, with higher frequencies appearing to have less branches; again, this will be a useful consideration dependent on the intended application of the MWs. For example, high branching wires may be used when contact with a large number of cells within a tissue is required, whereas linear wires may be used when direct contact between two cells is required.

As AC current has the possibility of improving MW growth biocompatibility, the next step was to provide the first 3D proof of concept of in-situ grown bioelectronics.

2.3.6. Developing 3D proof of concept

In order to utilise this method for wirelessly growing in-situ bioelectronics, it is necessary to control MW growth in the presence of biological systems.

We have previously shown MW growth to be possible in a 2D space; hence the next step was to grow MWs in a 3D cell culture model. To facilitate this, 3D spheroids were grown using U251 glioblastoma cells in a rotary cell culture system (RCCS). Glioblastoma cells were chosen due to possible future brain tumour applications of *in vivo* grown bioelectronics with TTFs. 3D cell spheroids provide an easy way to model 3D cellular environments; this is particularly true in cancer research as they may behave as a tumour with proliferating/quiescent/necrotic zones and mimic tumour physiological responses and drug resistance mechanisms¹⁸⁴. A number of methods exist to grow cell spheroids; however, the use of RCCS is beneficial as it allows the cells to secrete their own extracellular matrix (ECM) and therefore create more robust spheroids suitable to be prepared for wire growth.

In order to grow spheroids, 1×10^6 U251 cells were introduced to RCCS flasks with standard culture media (DMEM). Spheroid growth was optimised by varying the rotary speed in revolutions per minute (rpm) of the RCCS. Rotary

speeds included 12, 15 and 18 rpm. Initial studies were performed at 10 days for all three speeds, with 50% media changes being performed every 3 days. As seen in Figure 2-15:A and C, a large amount of cell debris was present, and no spheroids could be collected at 15 rpm due to an infection. A study at 15 rpm was repeated with spheroids harvested at 7 days to limit risk of infection. The slower speed of 12 rpm produced significantly higher number of spheroids, although they were smaller in diameter than the higher speeds. As seen in Figure 2-15:D, 15 rpm at 7 days provided significantly larger spheroids than 10 days at 12 or 18 rpm. This shorter time frame also allowed for less cell debris. Due to Covid-19 impacts shorter studies were not repeated for the alternative speeds and, as a high number of spheroids was not crucial, the parameters that provided largest spheroids were chosen: 15 rpm for 7 days.

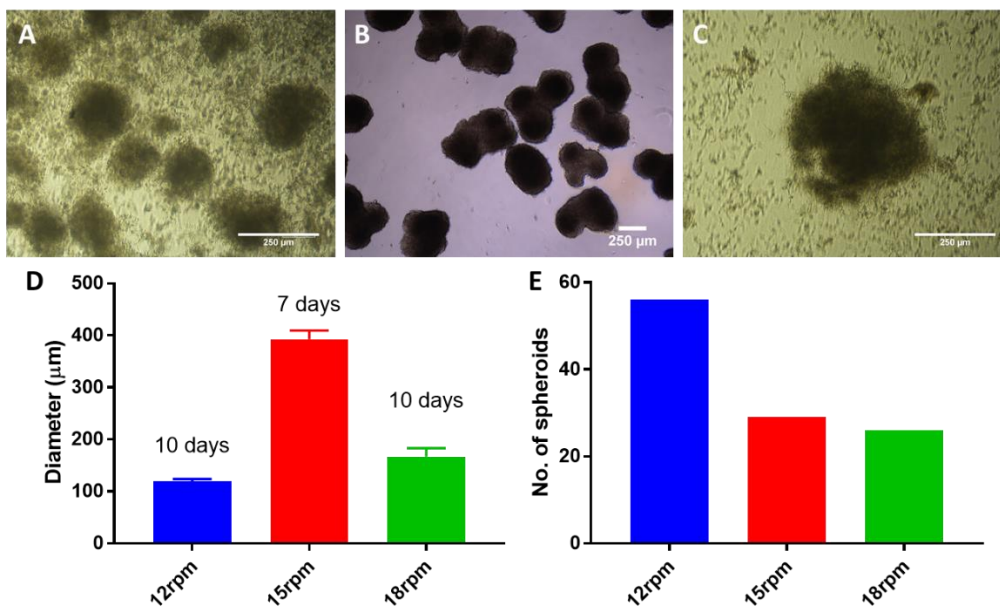


Figure 2-15 Optimisation of spheroid growth comparing rotational speeds of 12 (A), 15 (B) and 18 rpm (C). Initial experiments were performed at 10 days, 15 rpm was then repeated for 7 days.

Following their growth, spheroids were attached to BPEs between two FEs (1 mm apart) using a coating of poly-d-lysine. This allowed them to stay between electrodes, rather than be influenced by flux in the electrolyte. As seen in Figure 2-15, average spheroid diameter ranged from $\sim 100\text{-}400\ \mu\text{m}$ and so 2-3 spheroids were attached between FEs that were 1mm apart. AC electrical stimulation was then used to attempt wire growth in the presence of the spheroids; identical electrical inputs as in section 2.3.5 were used. As seen in Figure 2-16, MW growth was possible at 50 V (0.5 kV/cm), 1 MHz; however, only a very small wire grew, of approximately $50\ \mu\text{m}$ in length and the high potential meant that large clumps of cells broke off of the spheroid. It is expected that wire growth was not possible at any other inputs due to the spheroids introducing a high impedance to the BES. It is possible these increased impedances could be overcome by using higher frequencies, although this was outside of capabilities during Covid-19.

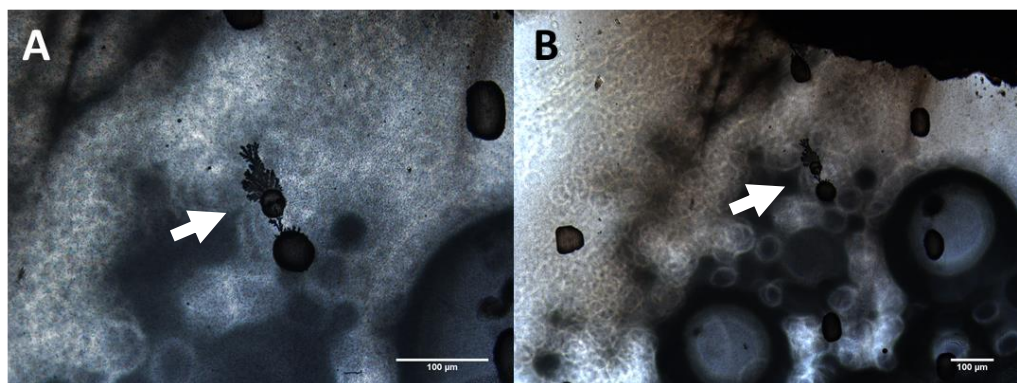


Figure 2-16 Optical images of MW growth using 50 V at 1 MHz in the presence of 2D monolayers.

Arrows highlight MWs. Scale bars represent $100\ \mu\text{m}$.

As AC stimulation was not capable of growing MWs in the presence of cell spheroids, DC stimulation was then pursued. As seen in Figure 2-17, MW growth was successful when using 50 V (0.5 kV/cm) of DC applied to a single spheroid of approximately 800 μm in diameter. Due to the 3D nature of the cell spheroids they were challenging to image, with wires growing through different focus planes; however, it can be seen that MWs successfully grew around and underneath spheroids. Wire diameter was $7.89 \pm 0.6 \mu\text{m}$ (from 50 measurements), which is similar to when these electrical inputs are used without cells (Figure 2-10). This suggests that wire structure is similar to studies without cells: formed from Ag NPs. Further study of these wires using SEM and EDS would be beneficial to determine this.

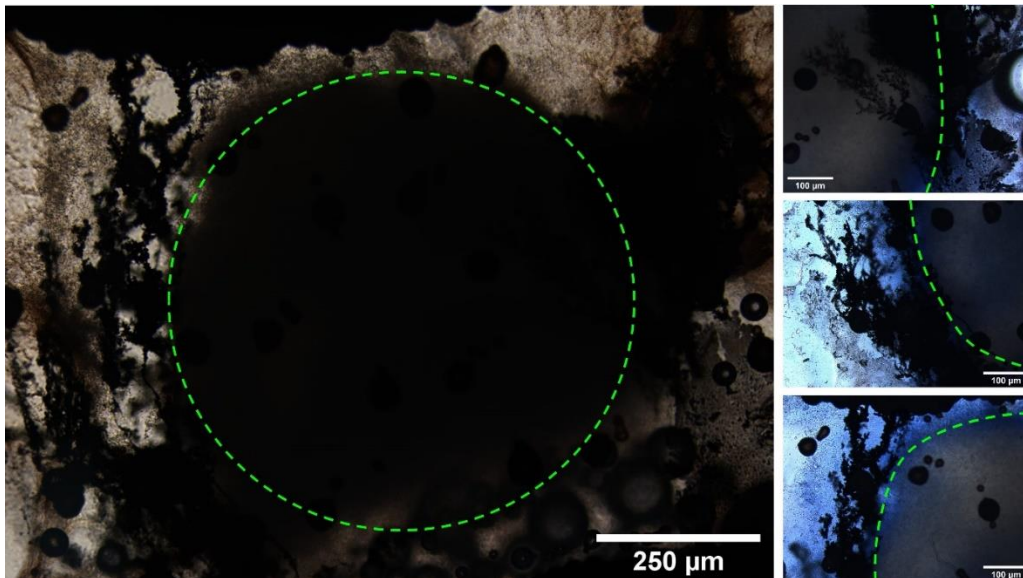


Figure 2-17 Optical images of Ag MW growth in the presence of spheroids. Green dotted outlined shows the main bulk of the spheroid.

Due to limitations during the Covid-19 pandemic, fluorescence viability assays applied to the spheroids could not be imaged. To approximate the effect of MW growth on the cell viability trypan blue was applied to spheroids. This suggested that a small population of cells had broken away from the surface of the spheroid and were not viable; although, the main cell population's membranes appeared still intact.

This is the first 3D proof of concept using wireless electrochemistry to grow conductive structures with biological systems and hence is an exciting addition to the existing literature. This shows promise that we may utilise the above and similar electrochemical methods to grow conductive structures *in vivo*. As 3D cell spheroids are often used to model tumours, this suggests we may be able to grow MWs around tumours for the study of cancer. Further optimisation may allow for these conductive structures to be grown around tumours sites *in vivo* for enhancing TTFs to treat cancer.

2.3.7. Microwire growth from a metal salt

In order to allow for wireless growth *in vivo* the elements needed for MW growth cannot be sourced from the FEs: as is the case with the above Ag proof of concept studies. As mentioned in section 1.1.3.1, this would be possible with the use of a metal salt or conductive monomer injected into the body, with *ex vivo* FEs. In order to show the efficacy of this, Au MWs were grown using AuCl in dH₂O. FEs were manufactured by printing an experimental Au ink, and hence

sample print quality is low. However, as seen in Figure 2-18, Au MW growth was possible using 80 V (0.8 kV/cm) of DC stimulation. MW \varnothing was 5.49 ± 0.45 μm (mean and SEM of 50 measurements) and appeared to be a similar structure to Ag MWs: being made up of NPs. Further characterisation of MWs and their make-up is required using SEM and EDS.

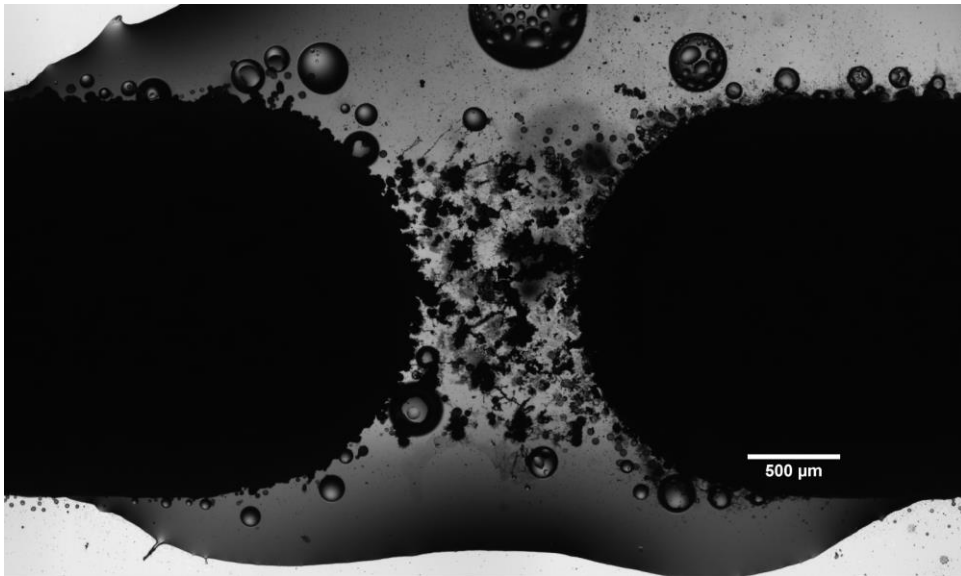


Figure 2-18 Optical images showing Au MW growth initiating from AuCl. Electrodes were inkjet printed with dH₂O used as an electrolyte.

These results are the first wireless example of metal MWs grown using the addition of a metal salt. This shows promise for using this method *in vivo*, as MWs may be grown wirelessly using *ex vivo* FEs with injected BPEs and metal salt. Further studies are required using cells and insulated FEs to simulate MW growth using *ex vivo* FEs.

2.4. Summary and Conclusions

These results show great promise for growing bioelectronics in-situ using bipolar electrochemistry. The hypothesis that we will be able to direct wire growth in the x and y directions by using BPE geometry and orientation is accepted. Wire growth direction can be focused at a BPE point, whilst curved and flat edges allow for MW growth across their entire edge. Varying geometry has little effect on MW diameter and resistance, suggesting that geometry and orientation of BPEs can be harnessed to control wire growth without affecting the functionality of wires. This is a key finding as no other studies investigate the design of BPEs and how they may be exploited to control wire growth.

Results also show that the incorporation of micro-satellite BPEs improve the number of MWs grown, suggesting that future BESs for wireless MW growth should incorporate a mixture of sized BPEs; Large BPEs are required to reduce impedance and therefore potentials needed to grow MWs, whilst smaller BPEs are useful for creating nucleation points for MW growth. Again, this is a key finding that highlights design implications useful for microfabrication applications of wireless electrochemical wire growth.

Next, a study using AC electrical stimulation to wirelessly grow MWs is performed. This is the first wireless study of varying frequency to assess the effects on MW growth. Low frequencies, <1 kHz, provide broken MWs that reach lengths of ~100-300 μm , without connecting the two FEs. This is due to

the large flux in the electrolyte at low frequencies, causing the very fine MWs (0.5-1 μm \varnothing) to break. Higher frequencies ≥ 10 kHz produce complete wires that span between the FEs. Unstructured growth and wire \varnothing are reduced with increasing frequencies. Increasing frequency also allowed for lower potentials to be used, with 50 V (0.5 kV/cm) growing MWs successfully at 1 MHz.

Following further optimisation of MW growth parameters, the first 3D proof of concept for wirelessly growing MWs in the presence of cells is presented. 3D cell spheroids were grown using a RCCS, before then being attached between FEs and stimulated for MW growth. MW growth was successful, with wires growing around and under cell spheroids. Viability of the main body of the spheroids appeared to be intact, although some cell death was experienced in the outer layer of the spheroids. This success was achieved using DC electrical stimulation, as AC parameters were only capable of growing small MWs at the extremities of equipment capabilities. This proof of concept is an important step towards developing *in vivo* grown bioelectronics and suggests that further optimisation could lead to MWs being grown in and around tumour sites for the treatment of cancer.

Finally, we present a proof of concept for wireless MW growth using the addition of a metal salt. This is the first example of wirelessly growing metal MWs using material that is not sourced from the FEs or BPEs^{109,112}. Au MWs were successfully grown using AuCl with 80 V (0.8 kV/cm) of DC stimulation.

This success suggests wireless growth of metals could be possible *in vivo* using the injection of BPEs and metal salts (Figure 1-2); the next step required is to develop appropriate BPEs for this application.

Chapter 3. Development of Nano Bipolar Electrodes

Aim: Develop a bipolar electrochemical system that is compatible with biology

In order to merge bipolar electrochemistry with biology, suitable BPEs are required. Nanoparticles (NPs) are an excellent solution due to their equivalent scale (≤ 100 nm) to cellular components, widely known biocompatibility and ease of functionalisation for tuning of properties. Hence, in this chapter we assess the application of four NPs as BPEs with biology, therefore addressing the second aim of this thesis.

A conductive polymer (polypyrrole, PPy), a conductive metal (Au), a semiconductive material (silica coated iron, ScreenMag) and a non-conductive control (silica, ScreenCore) were characterised for their suitability as BPEs. This consisted of initial size characterisation, conductivity, biocompatibility and bipolar electrochemistry studies. ScreenMag and ScreenCore proved to have some toxicity at higher concentrations, were both non-conductive, and unable to partake in bipolar electrochemical reactions. However, both Au NPs and PPy NPs were shown to be biocompatible and capable of performing as BPEs (characterised through DLS and TEM/EDS). Due to this, Au NPs and PPy NPs were then assessed in the presence of cells and tumour treating fields (TTFs). Results suggest that both NPs are capable of enhancing the effects of TTFs on U251 cells and therefore could be used to improve patient outcomes or lower timeframes/electrical inputs/costs of TTF therapies.

3.1. Introduction

In order to translate BESs to *in vivo* use, it is essential to design appropriate BPEs. It is likely these would take the form of NPs, which are both conductive and biocompatible, as they can be easily injected into the body. NPs are of an equivalent scale to cellular components such as receptors, channels, ligands and nucleic acids¹⁸⁵. They are also advantageous as they may be easily functionalised for additional properties such as fluorescence and specific site targeting.

NPs are used for a wide range of applications *in vivo* where, in cancer therapy in particular, this includes drug delivery^{186,187}, enhancing imaging and diagnostics¹⁸⁸ and photothermal/photodynamic therapies¹⁸⁹ (PTT/PDTs). NPs within the range of 10 – 100 nm are preferred due to the enhanced permeability and retention effect (EPR), which means they are likely to accumulate in tumour sites rather than normal tissue¹⁹⁰. A wide range of NPs have been used *in vitro* including: organic NPs, such as lipids¹⁹¹ and polymers¹⁸⁶; inorganic NPs, such as gold¹⁹² and magnetic NPs¹⁹³; and hybrid NPs, such as cell membrane coated NPs¹⁹⁴.

NPs have been previously shown to act as BPEs, with bipolar electrochemistry being used to create Janus particles¹⁰⁸: particles with two opposing sides of differing features/chemistry. However, they have not been integrated with biology due to the expected high voltages required to actuate

reactions at a nanoscale electrode (Equation (1-5)). This may not be the case, as it has been observed that nano-BPEs behave contrary to theory in practice, with nano-BPEs partaking in redox reactions at much smaller potentials than predicted necessary^{133,195}.

Although NPs have been used as BPEs and also in a wide range of applications with cells, few of these applications require the particles to be both electrically conductive *and* biocompatible. Therefore, this chapter is dedicated to developing NPs for this unique application. To do so, a range of NPs were characterised for their conductivity, biocompatibility and ability to perform as BPEs. Three classes of conductive NPs were chosen: conductive metal NPs, conductive polymer NPs and semi-conductive NPs.

Au NPs were chosen as a metal NP example as they have previously been reported to be taken up by cells without causing cell death¹⁹⁶. They have also been used for multiple *in vivo* applications including cancer treatments¹⁹². Varying sizes of Au NPs were used: 40 nm Au NPs could be easily synthesised in house and so were initially used, 125 nm Au NPs were later used, to be compatible with techniques that may be pursued in the future (assessing plasmonic effects).

PPy NPs were chosen as a conductive polymer example. It was expected that when moving to *in vivo* applications, conductive polymers would be ideal for BPEs as they can be created to be biocompatible and biodegradable¹⁹⁷; They

may also provide flexibility properties that are more similar to biological materials than metals. PPy NPs of around 100 nm were synthesised in house.

ScreenMag particles were purchased as semi-conductive NPs. These particles have previously been used with biological systems *in vitro*¹⁹⁸. ScreenCore NPs are a non-conductive control of these particles – i.e., without the iron core. These NPs are larger in size (1 μm) and fluorescent to allow them to be visualised in *in vivo* studies using light microscopy. This increased size, outside the EPR effect, may have significant effects on NP applications with cancer cells, as well as altering bipolar electrochemical properties and the potentials required to drive electrochemical reactions. This may also impact how the NPs are up-taken by cells¹⁹⁹. However, this is not of concern at this proof-of-concept stage.

The aim of this chapter was to assess which class of NP would be most suitable for use as BPEs within biology.

3.2. Materials and Methods

3.2.1. NP Synthesis and Characterisation

Four nanoparticles were tested for their application as BPEs: ScreenMag and ScreenCore NPs (Chemicell GmbH), Au NPs (40 nm synthesised in-house/125 nm NanoPartz Inc.) and PPy NPs (synthesised in-house).

PPy NPs were synthesised in-house using an adapted method²⁰⁰ as seen in Figure 3-1. A stock of 84 μl pyrrole in dH_2O (0.1M) was added dropwise at 10 μl every 10 seconds to FeCl_3 in dH_2O (heated at 100°C , 0.23M) with 7.5wt% PVA (M_w 31,000, Sigma Aldrich). The mixture was stirred in a cold room (4°C) for 10 hrs, and then washed with boiling hot water, using a centrifuge at 12,000 rpm, as described in the following section.

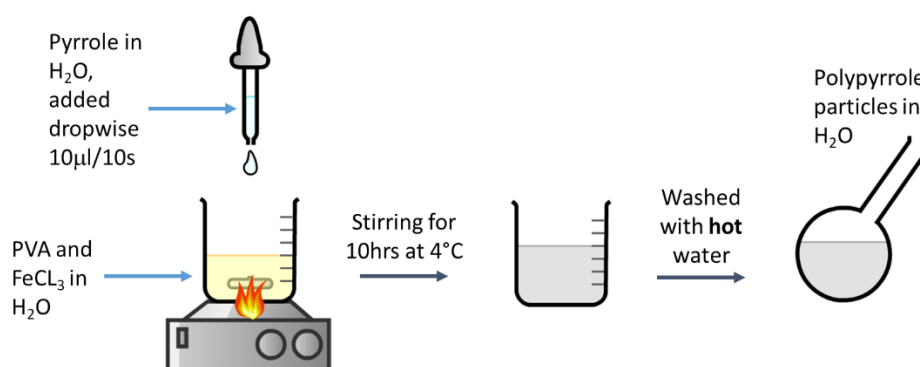


Figure 3-1 Synthesis of PPy NPs using FeCl_3 as an oxidising agent and PVA as a surfactant. PVA, FeCl_3 and deionised H_2O are combined under stirring and heat (100°C) before pyrrole monomer is added dropwise. The reaction is stirred for 10hrs at 4°C before NPs then being washed using hot water.

Citrate capped Au NPs of 40 nm \varnothing were synthesised in-house using the method illustrated below (Figure 3-2)²⁰¹. 100 ml of H_{AuCl}₄ in dH₂O (1 mM) is stirred and heated until a rolling boil is reached. 10 ml of Na₃C₆H₅O₇ in dH₂O (38.8 mM) is rapidly added to the solution and boiled for a further 10 minutes. The solution is then filtered using 0.22 μ m millipore membrane filters (Sigma Aldrich).

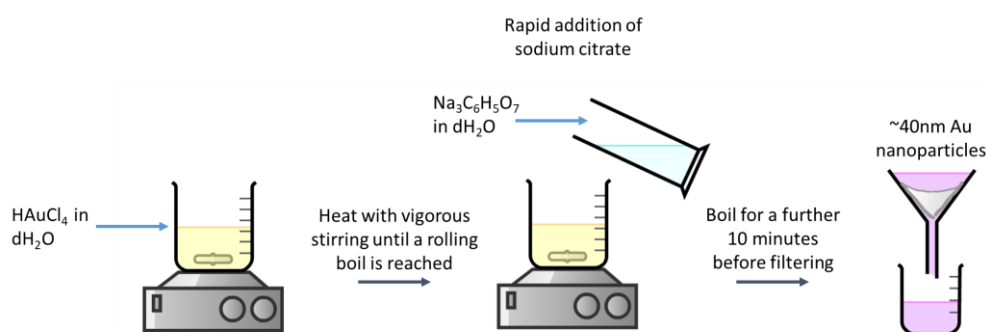


Figure 3-2 Schematic of Au NP synthesis. H_{AuCl}₄ in dH₂O is heated and stirred until a rolling boil is achieved. Sodium citrate is then rapidly added and solution is boiled for a further 10 minutes before filtering.

Particles were characterised using multiple methods described in Section 1.2.5: UV-Vis, DLS and SEM/TEM. For all characterisation studies, NP solutions were sonicated (5 minutes) and filtered (0.4 μ m filters) beforehand. Approximately 1 ml of NP solutions, suspended in dH₂O, were placed into cuvettes for UV-Vis and DLS. For SEM/TEM droplets of NP solutions were dried

onto aluminium SEM studs or carbon TEM grids respectively. Equipment and parameters used can be found in section 1.2.5.

3.2.1.1. Conductivity

NP conductivity was characterised using impedance spectroscopy of NP dispersions in dH₂O. Varying concentrations of NPs were used to determine if the addition of NPs reduced impedance, therefore suggesting they are conductive. An Autolab Potentiostat was used to measure impedance in potentiostatic mode (0.01 V_{RMS}). Impedance was recorded at 100 Hz.

3.2.1.2. Biocompatibility

Biocompatibility was assessed by incubating U251 cells with NPs for 4, 24 and 48 hours. A plate reader and two fluorescence assays were used to assess cell proliferation and metabolic activity: Calcein Acetoxymethyl (Calcein AM)/Ethidium homodimer (EthD-1) live/dead stain (Thermo Fisher Scientific) and WST-8 Cell Counting Kit (CCK-8, Sigma Aldrich). Calcein AM and EthD-1 live/dead cytotoxicity kit provides an easy two-colour assay to determine the viability of a population of cells based on plasma membrane integrity and esterase activity. Calcein AM stains the cell membrane green showing viable cells, where as EthD-1 stains the nucleus red, when the cell membrane is not intact, showing non-viable cells. CCK-8 is a metabolic viability assay using WST-8 (2-(2-methoxy-4-nitrophenyl)-3-(4-nitrophenyl)-5-(2,4-disulfophenyl)-2H-tetrazolium, monosodium salt) which is bio-reduced by cellular dehydrogenases

to an orange formazan product. The amount of this orange product is directly proportional to the number of living cells allowing an alternative colorimetric viability assay. The detection of the formazan product can be performed using absorbance or fluorescence measurements.

Six concentrations of NPs were added to wells (96 well plate) seeded with 10,000 cells. For PPy, ScreenMag and ScreenCore, 0.005, 0.01, 0.05, 0.1, 0.5 and 1 $\mu\text{g}/\text{ml}$ of NPs were added. Higher concentrations could not be reached with Au NPs and therefore 0.0025, 0.005, 0.01, 0.025, 0.05, and 0.1 $\mu\text{g}/\text{ml}$ were added. Controls included a HBSS blank, assay with NPs, cells alone, cells with assay (live control), and cells incubated in 15% ethanol in HBSS for 15 minutes with assay (dead control). Separate plates were used for the 4-, 24- and 48-hour timepoints.

For proliferation studies, 100 μl of 2 μM Calcein AM and 4 μM EthD-1 in HBSS were added to cells. Fluorescence readout was acquired using one measurement per well (Calcein AM λ ex: 486 nm em: 530, EthD-1 λ ex: 530 nm em: 645 nm) and mean \pm SEM was plotted. Fluorescence for live and dead stains were normalised to the live and dead control wells.

For metabolic studies, 10 μl of WST-8 Cell Counting Kit with 90 μl of media was added to wells and incubated for 1 hour at 37°C. Absorbance (450 nm) was measured using 25 flashes per well. Absorbance was normalised using live and dead control wells.

3.2.2. *In Vitro* Bipolar Electrochemistry

In vitro bipolar electrochemistry experiments were carried out using a high voltage stimulator (EC100SA NF Systems) applying DC stimulation at 10 V (20 V/cm). NP solutions were combined with 1 mM PdCl₂ in dH₂O solution, in a 1:1 ratio per well, before being electrically stimulated using needle electrodes (Figure 3-3). Electrodes were placed 5 mm apart and samples were stimulated for 10 minutes.

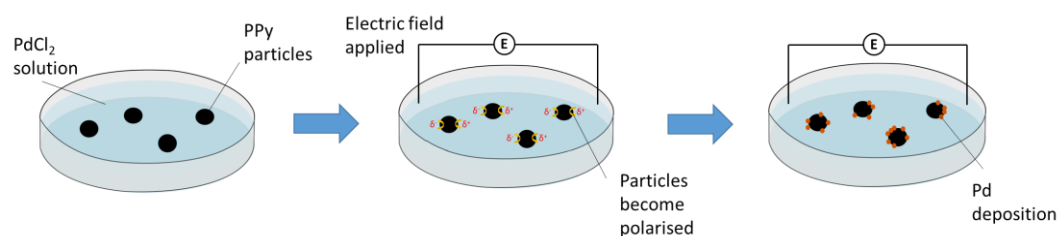


Figure 3-3 Schematic of bipolar electrochemical deposition of a metal onto the surface of NPs.

Needle electrodes are used to apply an electric field to NP and metal salt solutions in a culture dish.

The success of the electrochemical reaction was determined by measuring size, before and after, using DLS (described in section 1.2.5). For further confirmation, Au NPs and PPy NPs were also imaged using SEM (JEOL 7100F FEG-SEM) and TEM (FEI Tecnai G2 12 Biotwin) with EDS.

3.3. Results and Discussion

3.3.1. NP Synthesis Optimisation

To first assess the amenability of a conductive polymer for use as BPEs, PPy nanoparticles (PPy NPs) were synthesised using an existing method²⁰⁰. To confirm the success of the reactions, particles were characterised using UV-Vis and DLS. Despite UV-Vis confirming the synthesis of PPy with a characteristic peak at ~420 nm, DLS data showed a larger average size of 120 nm as opposed to ~80 nm reported in the literature²⁰⁰ (Figure 3-4). SEM was then performed to confirm NP size and shape. As seen in Figure 3-4, particles appeared to agglomerate into large surfaces, even when NP concentration was lowered. It was expected that this was due to remaining surfactant, that causes the particles to be adhesive. This highlighted the necessity for a more thorough washing approach.

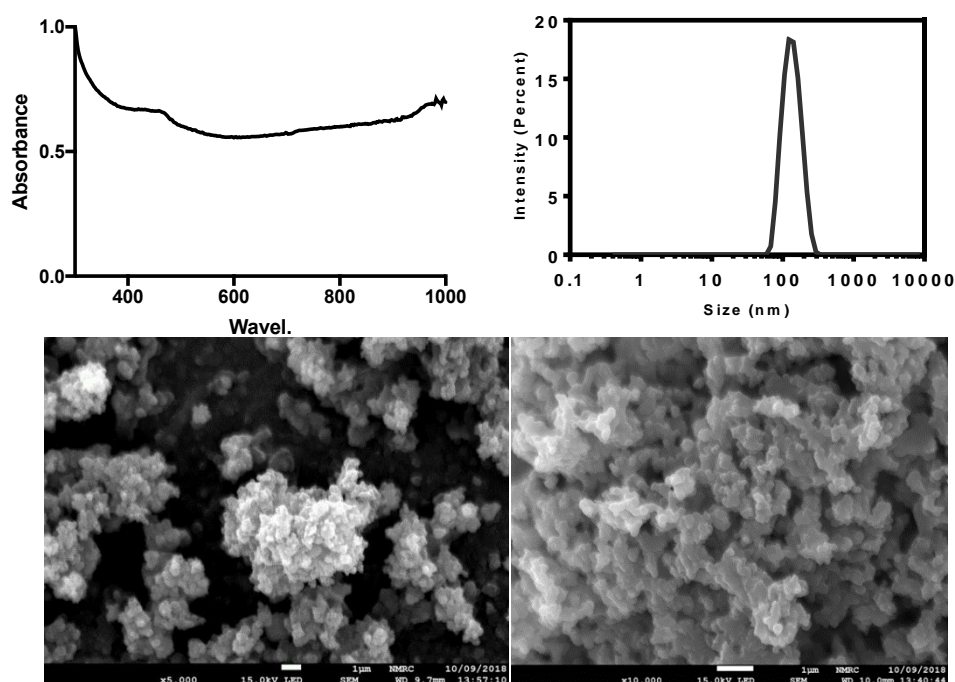


Figure 3-4 PPy NP characterisation using UV-Vis (A), DLS (B) and SEM (C and D). NPs were synthesised using an altered method. Liquid dispersions were used for UV-Vis and DLS measurements, whilst SEM samples were dried onto carbon substrates on aluminium stubs.

As it was expected that NP solutions were agglomerating due to excess surfactant not being washed away, the synthesis method was adapted to use hot water washes instead of room temperature water. It is known that any remaining PVA produces bubbles upon shaking the solution, therefore samples were washed until the removed supernatant produced little to no bubbles. This can be seen in Figure 3-5: where after four hot water washes the bubbles are greatly reduced. As seen by the colour of the supernatants, some PPy NPs are lost during washes; however, high yields mitigated this concern. To limit the amount lost and allow for fewer washes, the reaction solution was immediately diluted in boiling dH₂O (1:7) before subsequently performing the necessary

washes. This allowed for reproducible NPs to be synthesised, which did not agglomerate, as seen in Figure 3-6. The final produced PPy NPs had an average diameter of ~ 80 nm (characterised by SEM, discussed in the following section) and polydispersity of 0.1 (characterised by DLS): values now consistent with literature²⁰⁰.



Figure 3-5 PPy reaction supernatant retrieved after sequential washes in hot water (left to right).

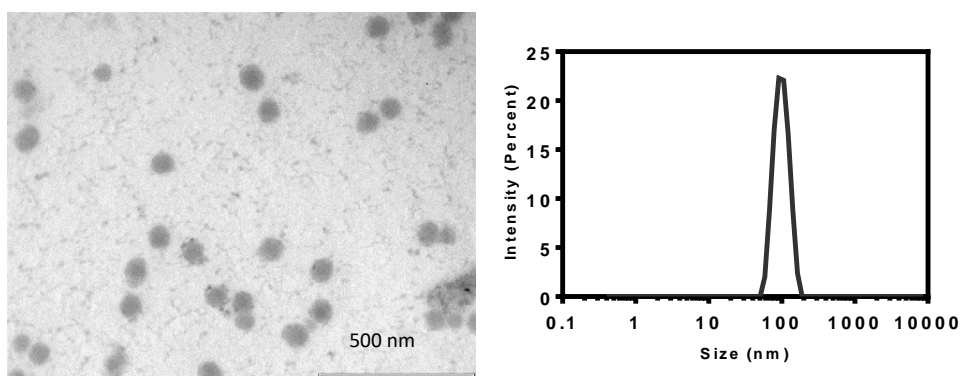


Figure 3-6 SEM of PPy NPs using an adapted method with hot water washes.

3.3.2. NP Characterisation

All four NPs were characterised using DLS and UV-Vis (section 1.2.5). As seen in Figure 3-7, sizes of NPs were reasonably consistent with specifications and previous synthesis characterisation: ~ 100 nm PPy NPs, ~ 40 nm Au NPs

(with agglomerates) and ~ 1000 nm ScreenMag and ScreenCore NPs. UV-Vis confirmed the synthesis of PPy with a broad absorption band, characteristic of the bipolaronic metallic state of doped PPy²⁰⁰. Peaks were present at approximately 420 nm, and >800 nm, coinciding with NPs from the synthesis protocol. Absorption spectra for Au NPs is also comparable to that published in the synthesis protocol²⁰¹, with a peak at 520 nm; this is consistent with Au NPs of approximately 40 nm in diameter²⁰². ScreenMag and ScreenCore particles had not been previously characterised using this method for comparison, although ScreenMag possessed a peak at ~ 420 nm, unlike ScreenCore, whereby this is expected to be due to the Fe₂O₃ core.

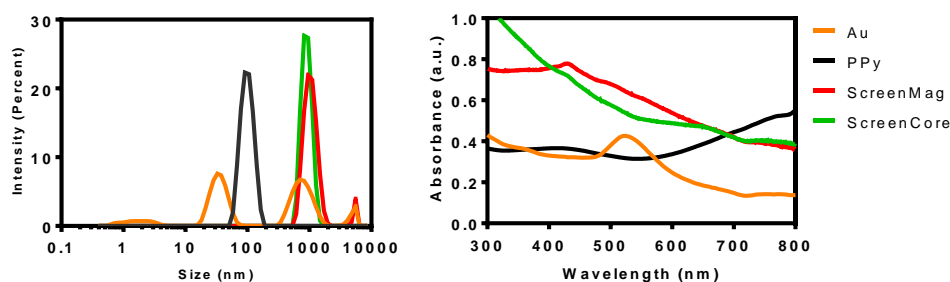


Figure 3-7 Characterisation of NP size and absorbance using DLS (A) and UV-Vis (B). For DLS measurements $n = 3$.

As DLS measures the hydrodynamic diameter of particles this technique usually provides a larger particle size²⁰³, and therefore for NPs synthesised in-house (PPy NPs and Au NPs) particle size was also confirmed using TEM. These results were in agreement with DLS data, with PPy NPs exhibiting an average size of $81 \text{ nm} \pm 2 \text{ nm}$ (SEM), and Au NPs having an average size of $33 \pm 5 \text{ nm}$

(SEM). Size is important for both biocompatibility and BPE capabilities (Equation (1-5)). Larger particles are preferred in terms of electronics, as they allow for a higher charge density and therefore expected lower electrical inputs. However, smaller particles may allow more widespread distribution across the body²⁰⁴. Size of NPs would also impact cellular toxicity and how the NPs are uptaken/processed by cells. This is of little concern at this proof of concept stage; however, size should ultimately be optimised for specific applications in varying tissue types.

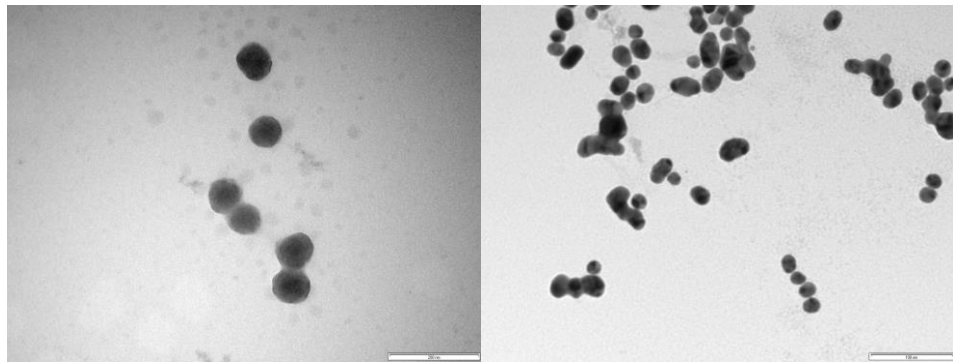


Figure 3-8 TEM images of PPy NPs and Au NPs. Scale bars represent 200 and 100 μm (left and right).

In order for NPs to behave as BPEs, they must be conductive to allow for the flow of electrons. Hence NP conductivity is a key material property when developing BPEs. Conductivity was assessed using impedance spectroscopy. It was expected that dH₂O solutions with a higher concentration of conductive NPs would have lowered impedance values. Hence, varying concentrations of NP dispersions were tested using electrochemical impedance spectroscopy

(EIS) to observe if such a relationship could be observed. Impedance values at 100 Hz were plotted for comparison (Figure 3-9).

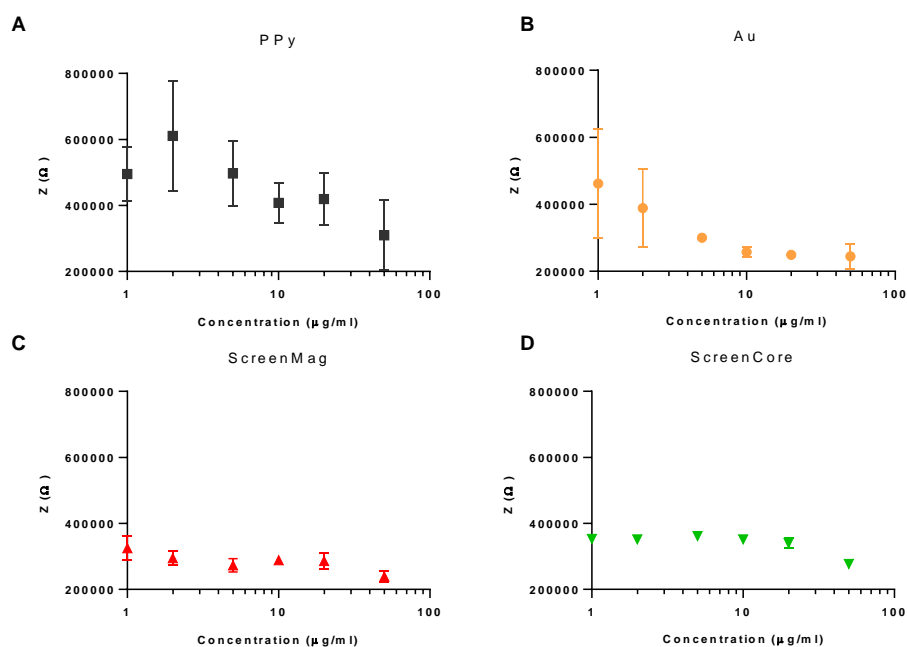


Figure 3-9 Characterisation of NP conductivity, carried out using electrical impedance spectroscopy EIS of varying PPy (A), Au (B), ScreenMag (C) and ScreenCore (D) NP concentration solutions. Error bars denote mean \pm SEM, n = 3.

PPy NPs showed a change in impedance over the concentration range, suggesting they are conductive. However, coefficients of variation ranging from 6% (20 µg/ml) to 50% (1 µg/ml) were observed (Table 3-1). This is expected to be due to large batch variation across the in-house synthesised particles. As polymer conductivity is dependent on the doping of the polymer²⁰⁵, large variations may be due to inadequate doping of PPy NPs. This could be rectified by increasing reaction temperature; however, low temperatures were used in

order to reduce PDI²⁰⁶. Further work is necessary to fully optimise the conductivity of a conductive polymer NP for this application. This could not be performed in the timeframe due to Covid-19 and hence these NPs were taken forward in their present condition for experimentation.

As expected, Au NPs also showed a decrease in impedance with increased NP concentration suggesting that they are conductive. Approximately two-fold greater errors were seen at lower concentrations for three of the NP samples (Au NPs, ScreenMag and ScreenCore). As this was consistently seen across differing NPs it was likely due to limitations of accurate pipetting when producing such small dilutions (Table 3-1). Ideally, another method was required to confirm conductivity, such as peak force AFM; however, this was not possible in the timeframe due to Covid-19. Furthermore, due to Covid-19, this characterisation was not repeated for the larger 125 nm Au NPs used later in this chapter.

As ScreenCore NPs were included as a non-conductive control, the steady impedance with varying NP concentration was anticipated. This is due to EIS measuring the impedance of the electrolyte, with no current passing through the ScreenCore particles. ScreenMag NPs with an iron centre exhibited similar behaviour, suggesting that they too are not conductive. Again, another method was ideally required to confirm exactly how these NPs are behaving.

Table 3-1 Coefficient of variance of NP impedance measurements at 100 Hz, supporting data presented in Figure 3-9 (n = 3).

$\mu\text{g/ml}$	Au	PPy	ScreenMag	ScreenCore
50	21.139	59.781	10.098	0.259
20	6.128	33.007	11.593	6.477
10	8.827	25.612	6.432	2.249
5	6.197	34.071	10.329	1.407
2	42.486	47.546	10.407	4.738
1	49.487	28.083	16.377	3.826

The biocompatibility of NPs is necessary for incorporation with biological systems, without inducing any detrimental cellular effects. A combination of multiple assays are required to sufficiently evaluate physiological responses to NPs²⁰⁷. Therefore, in order to determine limits for biocompatibility, U251 cells were incubated with varying concentrations of NPs for varying timeframes and assessed using both proliferation and metabolic assays. U251 glioblastoma cells were chosen for their relevance in future applications of these BESs with TTFs.

To study the effect of NPs on proliferation, a Calcein Acetoxymethyl (Calcein AM) and Ethidium Homodimer (EthD-1) live/dead stain was applied to cells after incubation with NPs. As seen in Figure 3-10, fluorescence was then evaluated using a plate reader and fluorescence plotted for both live and dead

cells. Live and dead fluorescence was normalised using three control wells with no NPs added. As seen in Figure 3-10: A, B, C and D, both Au NPs and PPy NPs showed little effect on proliferation. All concentrations had no effect at 4 hours and only appeared to decrease slightly over the longer time frames (although no significant difference was observed).

PPy NPs have been evaluated previously for their cytotoxicity^{208,209}. The aforementioned results are consistent with recent literature, which shows that the 100 nm particles have little effect on mammalian cells at concentrations much higher than those used herein (up to $\sim 250 \mu\text{g/ml}$)²⁰⁸. It is worth noting that lower concentrations were used for Au NP studies and hence, comparably higher concentrations could have some toxicity. However, the literature has shown smaller Au NPs to be non-toxic *in vitro* and Au NPs of 100 and 200 nm to be non-toxic *in vivo*²¹⁰. Both ScreenMag and ScreenCore NPs showed some effects on proliferation at higher concentrations. This is possibly due to the larger size of the particles.

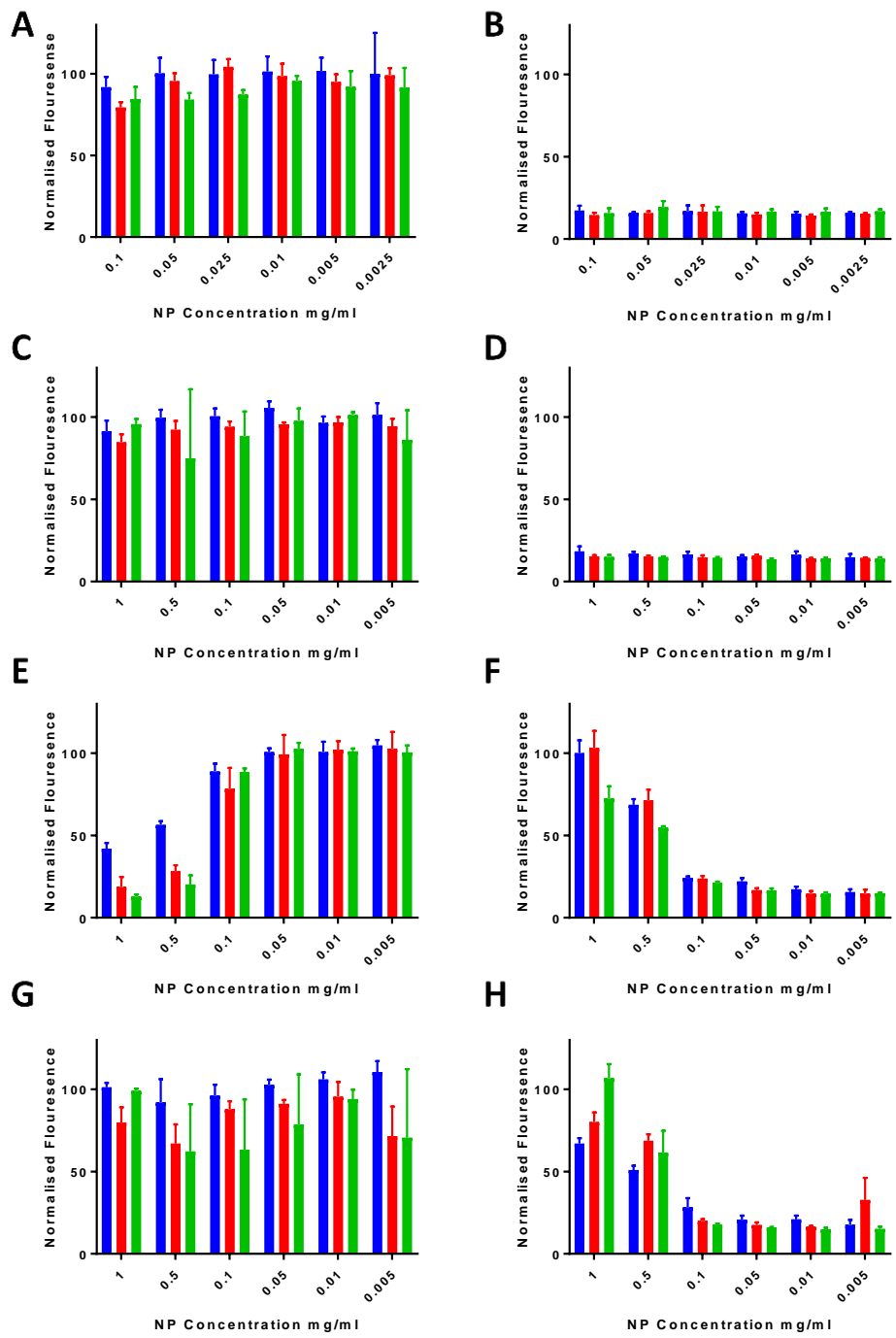


Figure 3-10 Characterisation of NP biocompatibility using live/dead assay (left/right respectively, Calcein AM/Ethidium Homodimer) for Au NPs (A/B), PPy NPs (C/D), ScreenMag NPs (E/F), and ScreenCore NPs (G/H). Cells were incubated with NPs for 4 (blue), 24 (red) and 48 (green) hours. Fluorescence was normalised using positive and negative controls.

To study the metabolic effects of NPs on cells, a WST-8 assay was applied to cells after incubation with NPs. As seen in Figure 3-11, no clear trends were seen for all NPs suggesting there is little effect on metabolic activity and hence impairment of cellular viability is not a concern at the levels of concentrations used in this study.

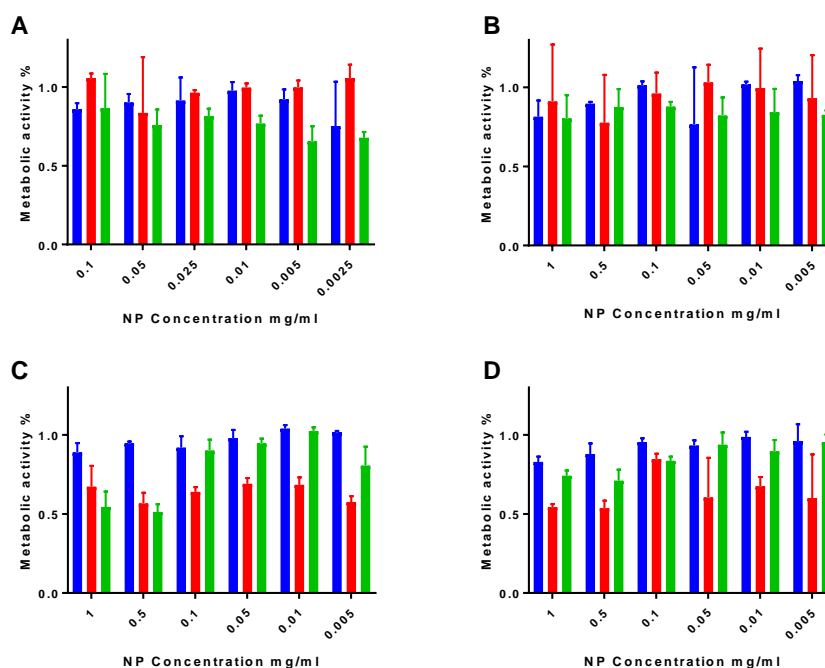
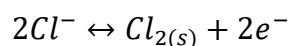
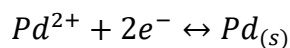


Figure 3-11 Biocompatibility of NPs assessed using WST-8 metabolic assay for Au NPs (A), PPy NPs (B), ScreenMag NPs (C), and ScreenCore NPs (D). Varying concentrations of NPs were suspended in media and incubated with cells for 4 (blue), 24 (red) and 48 (green) hours. Absorbance was normalised to a live control to provide metabolic activity %.

3.3.3. Bipolar Electrochemical Deposition on NP BPEs

To assess the capability of NPs to act as BPEs, a simple metal salt redox reaction was performed. A metal salt (PdCl_2) was added, and samples were electrically stimulated. It was expected that NPs would become polarised by an

applied electric field, thereby creating the potential difference to reduce $Pd^{2+}_{(aq)}$ and deposit $Pd^0_{(s)}$ onto the NP surface (Figure 3-3 and Equation (3-1)). The success of this metal deposition was first determined by measuring the change in the size of NPs using DLS (Figure 3-12). NPs were also electrically stimulated without the presence of a metal salt to determine whether the change was due to electrostatic attraction or metal deposition. $PdCl_2$ was also added without the presence of electrical stimulation to determine whether any increase in size was due to the presence of salt alone.



Equation (3-1) Half equations for redox reactions when depositing Pd onto NPs from $PdCl_2$.

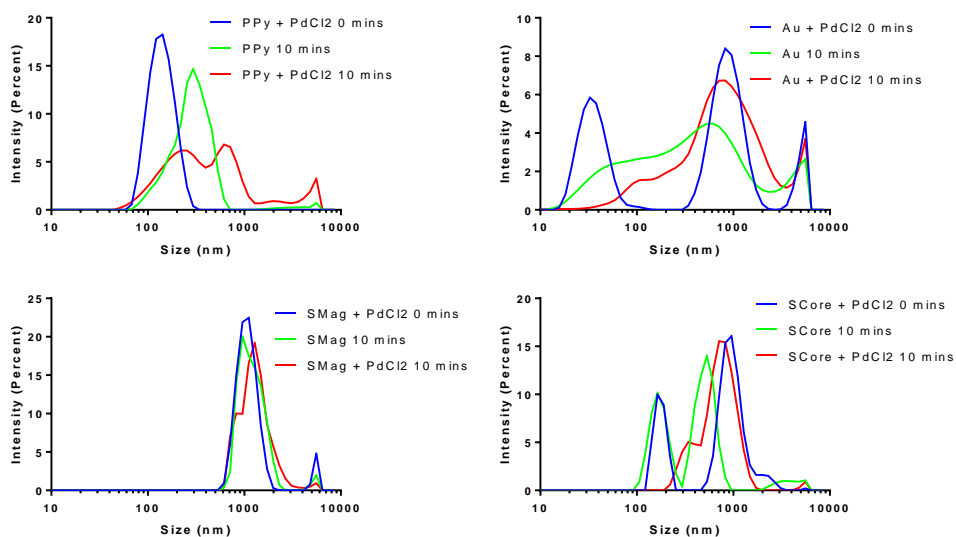


Figure 3-12 Evaluation of NPs application as BPEs through the measurement of the size distribution of NPs using DLS. NP dispersions in deionised water were measured before and after electrical stimulation, with and without the presence of a metal salt ($PdCl_2$).

PPy NPs showed a size increase with the inclusion of PdCl₂ and electrical stimulation, with peaks at ~150 and ~650 nm (PPy + PdCl₂ 10 mins). This was different from that with electrical stimulation alone, which showed a peak at ~250 nm (PPy 10 mins). No increase in size was present with PdCl₂ alone, with PPy NPs possessing an approximate size of 100 nm (PPy + PdCl₂ 0 mins). This suggests that the size increases are not caused by the presence of the metal salt and therefore metal deposition may be taking place.

Au NPs synthesised in-house were used for DLS experiments, that had an approximate size of 30 nm. As Au NPs are known to agglomerate in the presence of salts²¹¹ (unlike PPy NPs), the salt alone causes large peaks of ~1000 nm to form (Au + PdCl₂ 0 mins). Electrical stimulation also causes the formation of larger peaks at ~50 and ~500 nm (Au 10 mins). This makes it difficult to determine whether metal deposition is occurring. Samples with both electrical stimulation and metal salt presence do show different peaks compared to the controls; however, further investigation is required to confirm whether this is due to deposition or just a combination of the effects from the salt and electrical stimulation.

Both ScreenMag and ScreenCore showed no increase in size with the incorporation of metal salt and electrical stimulation (peaks at ~1000 nm). This suggests no metal deposition is taking place, as anticipated due to NPs not being conductive. ScreenCore samples possessed unknown smaller peaks at

~150 nm, which are expected to be due to contamination of the ScreenCore NP samples, as they are present both with and without electrical stimulation and with and without PdCl².

To further evaluate whether NPs had participated in a redox reaction, both Au NPs and PPy NPs were imaged using SEM and TEM with elemental mapping capabilities (EDS). For ease in imaging, and to give comparable sizes between Au NPs and PPy NPs, 125 nm Au NPs were used instead of the earlier tested 30 nm Au NPs. As seen in Figure 3-13, SEM imaging with EDS mapping of Au NPs showed that electrical stimulation concentrated the Pd and Cl around the area of the Au NP. Without electrical stimulation a large area of Pd and Cl has dried over the surface. This suggests that the Pd has deposited onto the Au NP surface; however, higher resolution images were needed for confirmation.

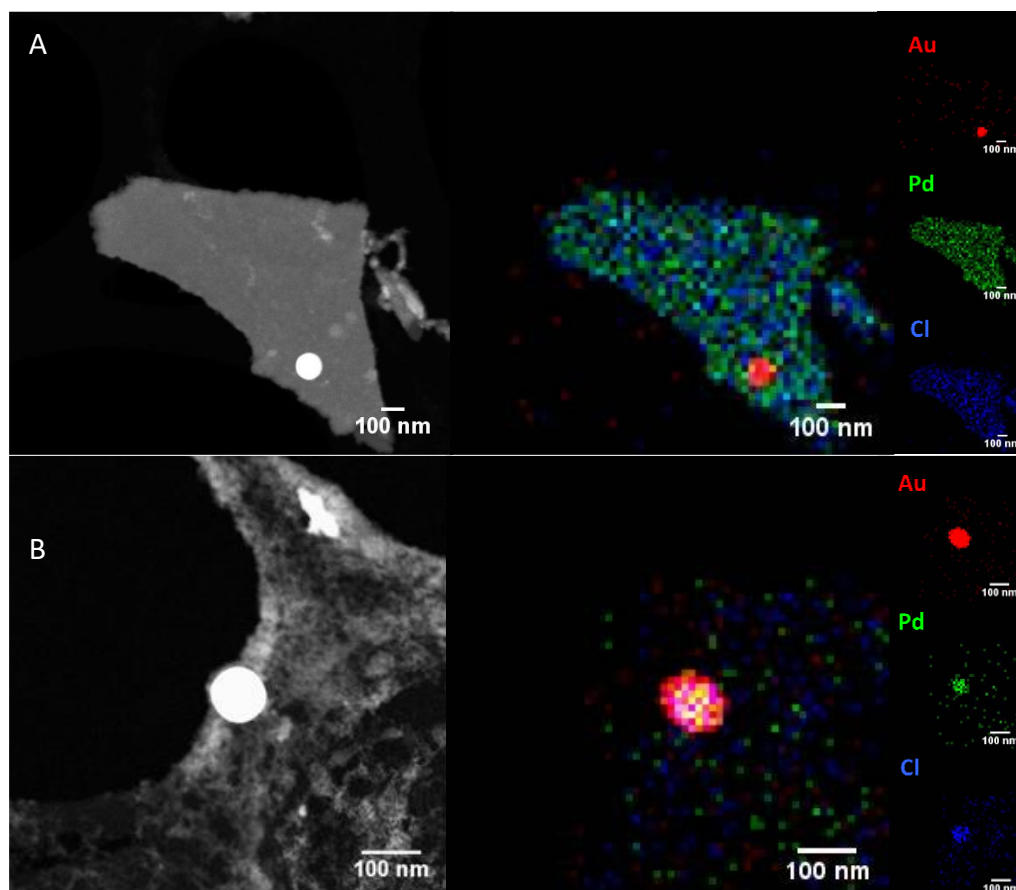


Figure 3-13 SEM images of Au NPs in the presence of PdCl₂, with (B) and without (A) electrical stimulation of 10 V for 10 minutes. Energy dispersive x-ray spectroscopy was used to create elemental maps of Au, Pd and Cl.

To visualise metal deposition with further detail, TEM imaging was performed. As seen in Figure 3-14:B electrical stimulation introduces a coating around the Au NPs that is mostly made up of Pd (Figure 3-14:D). When electrical stimulation is not present, this coating was not observed (Figure 3-14:A). This suggests that bipolar electrochemistry is taking place and that Pd^{0(s)} is being deposited on the Au NPs surface. Although the final control of Au NPs with electrical stimulation alone was not imaged (due to Covid-19), the

TEM images clearly show a coating is present and that a size increase is not due to electrostatic attraction alone.

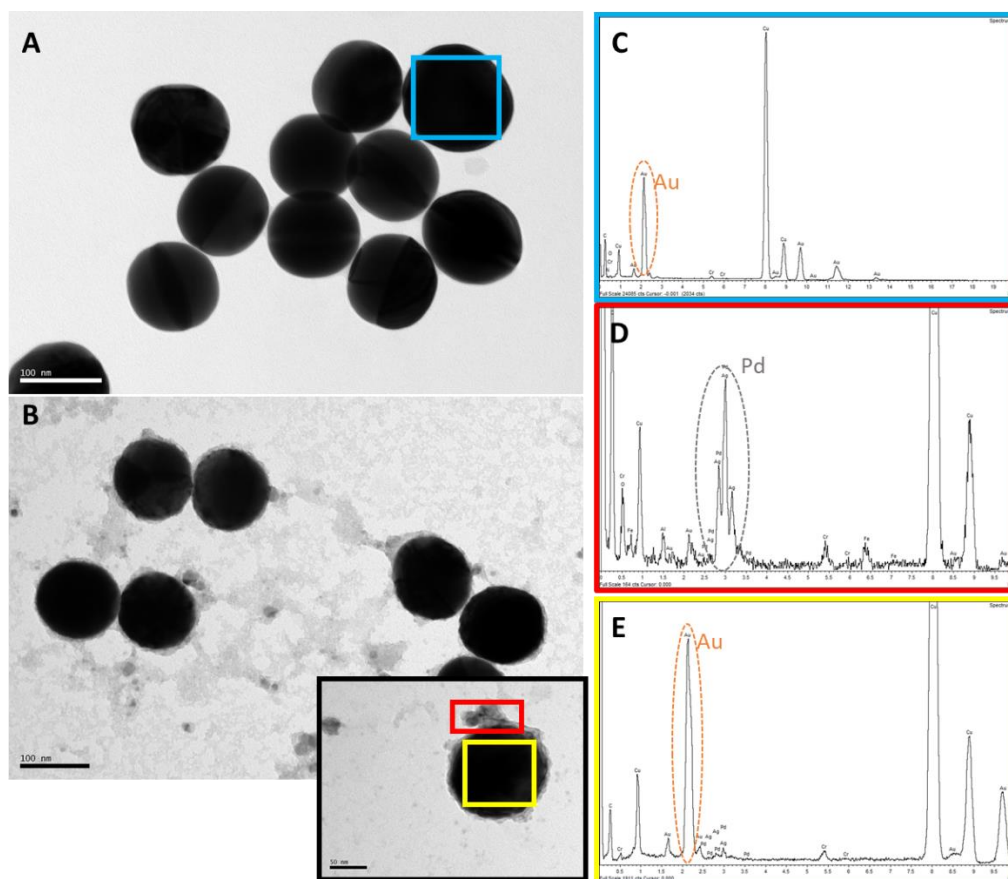


Figure 3-14 TEM images of single NPs (A/B) with corresponding energy dispersive x-ray (EDS) spectra (C/D/E). NPs were suspended in deionised water with 1mM PdCl₂, with sample B and inset also being subjected to 10 minutes of electrical stimulation at 10 V.

Similar experiments were carried out using PPy NPs; although this had to be undertaken by someone else due to Covid-19 and hence sample preparation is not consistent: leading to large areas of agglomerated NPs. Despite this, results still offer confidence that bipolar electrochemistry is taking place at the PPy NPs surface.

TEM with EDS was carried out to produce elemental maps similar to those produced with Au NPs. As seen in Figure 3-15, PPy NPs with PdCl₂ and electrical stimulation does appear to cause the deposition of Pd onto the PPy NP surface. Although there is a large Pd deposit without electrical stimulation (Figure 3-15:A), it does not follow the PPy NP shape and so does not appear to be on their surface. However, the Pd deposits in Figure 3-15:B do follow the size and shape of the PPy NPs, suggesting it is a coating on the PPy NP surface due to bipolar electrochemistry.

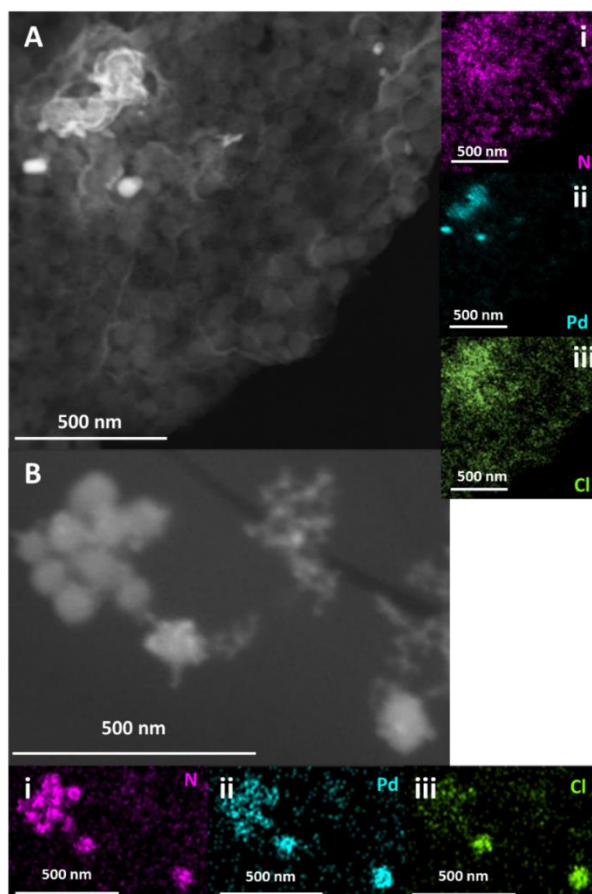


Figure 3-15 TEM with elemental mapping (EDS) of PPy NPs and PdCl₂ with (B) and without (A) electrical stimulation. Nitrogen, Palladium and Chlorine can be seen in i, ii, and iii respectively.

To further demonstrate this, we can view TEM images of PPy NPs and PdCl₂ with and without electrical stimulation, and PPy NPs with electrical stimulation alone. As seen in Figure 3-16:A/B, the application of electrical stimulation when PdCl₂ is present reveals visual differences when compared to PPy NPs and PdCl₂ with no electrical stimulation (Figure 3-16:C/D). Although apparently different to the coating present on Au NPs, the coating, when compared to the control samples, further suggests bipolar electrochemistry may be taking place. As seen in Figure 3-16:E/F, electrical stimulation alone does provide some alterations to the PPy NPs; however, it too appears visually different to PPy NPs and PdCl₂ with electrical stimulation. Again, this suggests that bipolar electrochemistry is taking place and that the alterations are not due to the electrical stimulation or salt addition alone.

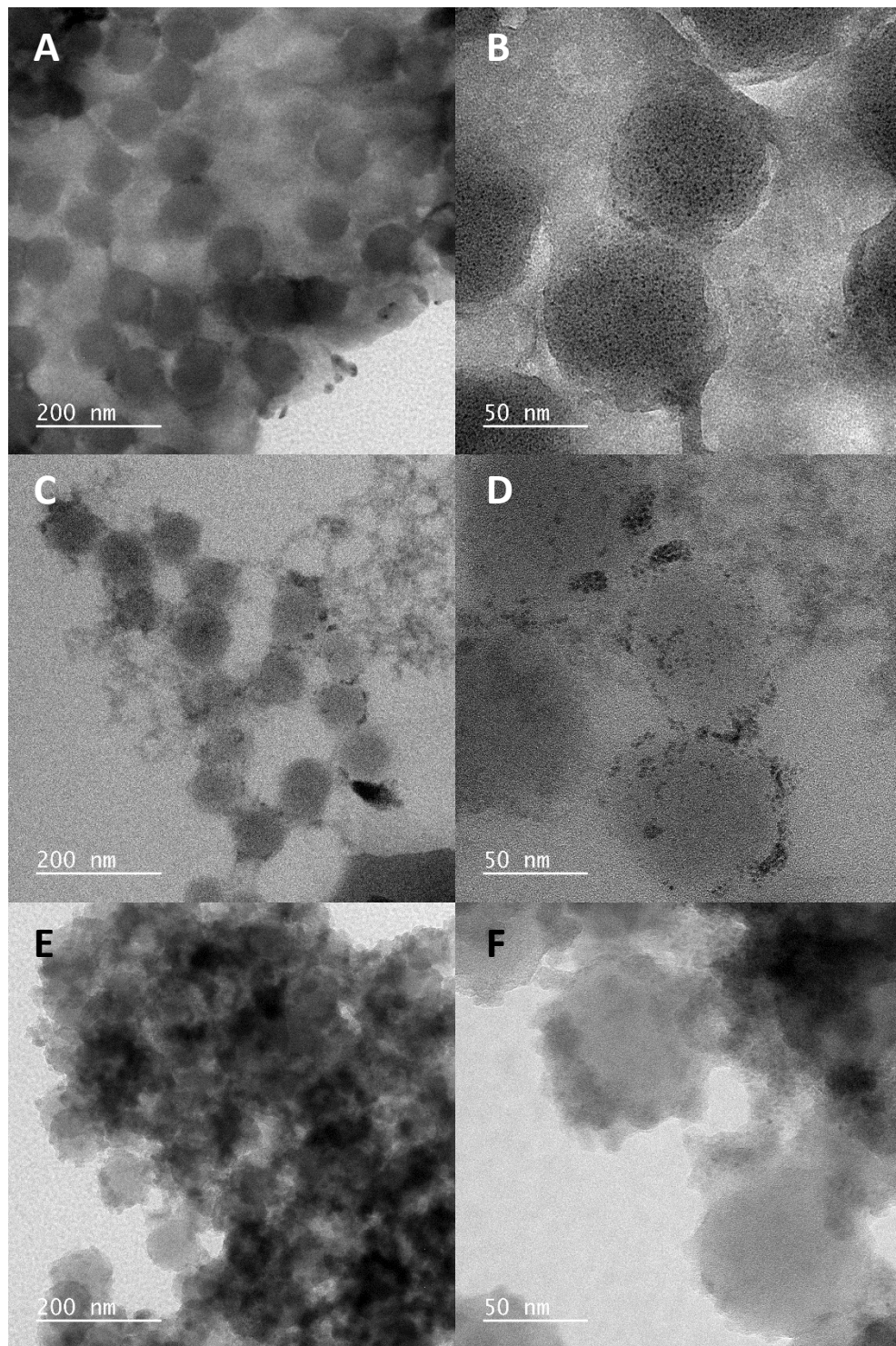


Figure 3-16 TEM images of PPy NPs in the presence of PdCl₂ with (C/D) and without (A/B) electrical stimulation. Control of PPy NPs with electrical stimulation alone can also be seen in (E/F).

As set out in section 1.2.3, BPEs of this size are thought to require large potentials in order to drive redox reactions. These results clearly refute this prediction, with redox reactions taking place under the application of just 20 V/cm. This new and compelling finding is hypothesised to be due to the behaviour of nanoelectrodes as discussed by Compton *et al*²¹². Nanoelectrodes, with radii less than 50 nm, are thought to behave differently to classical theory due to a marked curvature of the double layer. This curvature of the diffuse double layer leads to enhanced capacitance and therefore enhanced driving forces are expected for nanoelectrodes. This could explain why bipolar electrochemistry is taking place, where theory predicts an insufficient driving force.

To conclude, the above studies using a simple metal salt redox reaction with Au NPs and PPy NPs suggest that both are able to partake in the reaction as BPEs. This provides promise that both NPs could be used for wireless bioelectronic applications *in vivo*. Au NPs already have a wide range of biomedical applications, such as drug delivery, thermal ablation, biosensing and imaging enhancement, making them suitable to be translated to clinic²¹³. PPy was one of the earliest conductive polymers to be evaluated for use with mammalian cells²¹⁴, and has shown promise in biomedical applications such as eye conditions²¹⁵ and nerve restoration^{216–218}. However, previous biomedical applications include membranes and coatings rather than PPy in NP form. Although PPy NPs have previously been evaluated for their cytotoxicity, results

are conflicting^{208,209}; therefore a more thorough study of PPy NPs effect on biology would be required for these to be translated to clinical applications. PPy NPs have not been used in bipolar electrochemical applications before, as few NP applications exist. Au NPs have been shown to act as BPEs for intracellular sensing, although this used the application of high potentials (150 V, 7.5 kV/cm)¹³³. This work is the first proof of concept to suggest that Au NPs can be used as BPEs at much lower potentials (20 V/cm). Further investigation will determine whether this will allow for improved biocompatibility and therefore exciting applications *in vivo* (discussed further in section 5.2.2).

3.3.4. Application in Cancer Treatment

As discussed in section 1.1.3, the data presented in this thesis is aimed at applications in cancer treatment. The hypothesis is that wirelessly growing structures in and around tumours could potentiate the effects of Tumour Treating Fields (TTFs) therapy. As an initial step towards testing this prediction, NPs were incubated with U251 glioblastoma cells and incorporated in a TTFs device, the Inovitro™ laboratory research system. This evaluates whether conductive structures would enhance the effects of TTFs. As seen in Figure 3-17, with no TTFs, there is no significant difference between viability at 0-, 4- and 24-hour timepoints. This is also the case with TTFs alone. We hypothesise this is likely due to the timeframes not being long enough for the TTFs to have a cytotoxic effect²¹⁹. However, with the addition of both Au NPs and PPy NPs,

a significant difference is observed upon application of the TTFs. This suggests that the NPs are enhancing the electric fields and allowing for a cytotoxic effect to manifest at shorter timeframes. Due to Covid-19, controls without cells of NPs with Presto Blue metabolic substrate could not be completed. Hence, to confirm that this result is not due to NPs interfering with the assay, these would need to be performed.

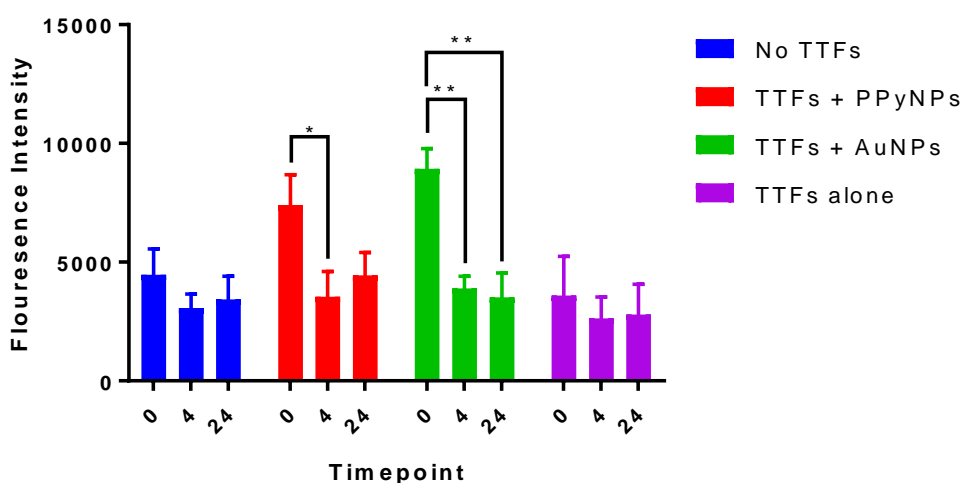


Figure 3-17 The effect of TTFs on cells with and without selected NPs. Fluorescence emitted from the conversion of a metabolic substrate using a Presto Blue assay is plotted to evaluate cell viability at 0-, 4- and 24-hours. Mean ($n = 3$) and SEMs are plotted. Statistical significance was determined using Tukey's multiple comparison test.

These results show promise that conductive structures may enhance TTFs and therefore lower therapy timeframes, electrical inputs, or costs. This work is discussed further in section 5.2.3.

3.4. Summary and Conclusions

In summary, four NPs were assessed for their application as BPEs. These included a conductive metal (Au NPs), a conductive polymer (PPy NPs), a semi-conductive NP (ScreenMag) and a non-conductive control (ScreenCore). Au and PPy NPs were synthesised in house and synthesis conditions optimised accordingly. Au NPs (125 nm), ScreenMag NPs and ScreenCore NPs were purchased commercially.

Au NPs were shown to be electrically conductive, and biocompatible at tested concentrations. They also successfully performed as BPEs as shown by DLS and TEM with EDS. The bipolar electrochemistry appeared to create a continuous thin layer of Pd on the surface of the Au NPs.

PPy NPs also raised no biocompatibility concerns, although conductivity was not confirmed using EIS as large variation was present, likely due to batch variation from in-house synthesised NPs. PPy NPs also performed as BPEs as shown by DLS and TEM with EDS. A layer of Pd appeared as small particles attached to the surface of the PPy NPs.

ScreenMag and ScreenCore NPs were shown to be non-conductive using EIS and raised concerns for biocompatibility at high concentrations. DLS also suggested that neither were behaving as BPEs and hence the particles were not taken forward for further study.

The chapter's aim of developing a BES that is compatible with biology was met, with two different NP BPEs showing biocompatibility and success in partaking in redox reactions: Au and PPy NPs.

Finally, Au NPs (125 nm) and PPy NPs (80 nm) were assessed in the presence of TTFs to determine if they could enhance cytotoxic effects. Initial studies suggest that both are capable of enhancing cytotoxicity, with significant difference in viability after just 4 hours of incubation with TTFs and NPs. This is the first evidence that conductive structures could enhance TTFs and shows great promise for improving this therapy to allow for wider uptake worldwide.

Chapter 4. Impedimetric Characterisation of Nano-Bipolar Electrodes

Aim: Further understand bipolar electrochemistry at the nanoscale, in order to be able to develop bipolar systems for use in novel biological applications

Merging of electronics with biology, defined as bioelectronics, at the nanoscale holds considerable promise for sensing and modulating cellular behaviour. Advancing our understanding of nano-bioelectronics will facilitate development and enable applications in biosensing, tissue engineering and bioelectronic medicine. However, studies investigating the electrical effects when merging wireless conductive nanoelectrodes with biology are lacking. Consequently, a tool is required to develop a greater understanding of merging conductive NPs with cells. Herein, this challenge is addressed by developing an impedimetric method to evaluate BESs that could report on electrical input. A theoretical framework is provided, using impedance to determine if conductive NPs can be polarized and used to drive current. It is then demonstrated that 125 nm Au NP BPEs could be sensed in the presence of cells when incorporated intracellularly at 500 $\mu\text{g/ml}$, using water and PBS as electrolytes. These results highlight how nanoscale BPEs act within biological systems. This research will impact the rational design of using BPE systems in cells for both sensing and actuating applications.

4.1. Introduction

We are entering a new era where bioelectronic tools enable us to harness and modulate cellular electricity. This allows us to control and sense cell behaviour for various applications, from biosensing, microbial fuel cells and to the treatment of disease^{1,2,220}. One of the remaining challenges to be overcome to further advance this area is to develop new nano-bioelectronics, capable of interfacing with cells at an equivalent spatial level of cellular electronic components, which can be operated remotely in a non-invasive manner. Also key, is the development of new sensing systems capable of measuring cellular bioelectronic inputs and outputs. In doing so, this will shed light on how bioelectricity underpins cell behaviour. To date, the rational design of wireless nano-bioelectronic systems has been limited due to the lack of label-free analytical techniques to study electrical effects on conductive nano-sized objects, when combined with biological cells. Therefore, the aim of this chapter was to address this particular scientific challenge and to further explore how electric fields interact with nanoscale bioelectronic systems (Figure 4-1).

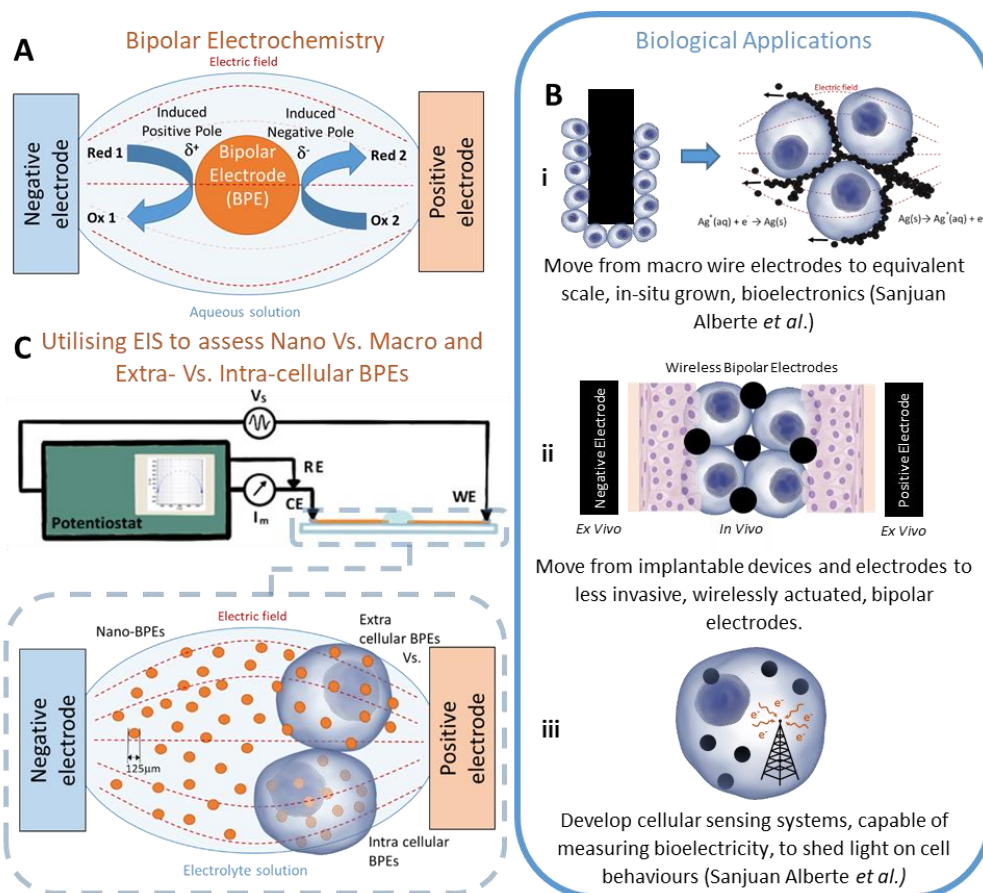


Figure 4-1: Interaction of electric fields with nanoscale bioelectronic systems. Schematic showing a bipolar electrochemical cell (A); applications of optimising bipolar electrochemistry in vivo (B) and the experimental set-up used herein to evaluate nano and nano-bioelectronic bipolar systems (C).

We have recently reported on the development of a nano-bioelectronic system that was based on using nano-BPEs in the presence of biological cells for the first time¹¹². This work was based on a BES which consists of BPEs and an aqueous electrolyte solution^{90,95–97}. Upon the application of an external electric field from FEs, the BPE becomes polarised. This means that the BPE has an induced positive and negative pole generating the thermodynamic driving force that can result in the ability to mediate redox reactions (Figure 4-1:A).

This ability to control redox reactions in cells has the potential for considerable therapeutic impact in diverse fields (Figure 4-1:B). We demonstrate in this work that Au NPs act as nano-antennae, due to an ability to sense external electric fields and then act as reporters via changes in electronic properties, which we sense by impedance spectroscopy (Figure 4-1:C).

The use of BPEs in electrochemistry is widespread^{98–104}. Over the last decade, new interest has revitalized the field with exciting applications at the micro/nanoscale^{108,221–223}. Bipolar electrochemistry is also a particularly attractive technique in electroanalysis applications due to its ability to wirelessly address multiple electrodes simultaneously. This allows for multiple detections to be carried out at once using a single pair of FEs. Such analytical applications make up a large area of the field and have been developed for both chemical and biological analytes. Examples have been recently reviewed^{105,117}.

Biological applications of BPEs have been used for the detection¹³⁵, imaging²²⁴, capture¹¹⁴ and lysis¹²³ of living cells. Many biological applications focus on the surface of cells or require cell lysis in order to analyse the intracellular content. One example of probing the intracellular space using bipolar electrochemistry involves piercing individual cells in order to sense hydrogen peroxide, glucose or SMase¹³². However, this does not fully exploit bipolar electrochemistry's wireless nature and high-throughput capabilities. By doing so, we may develop novel non-invasive intracellular bioelectronic

systems, that could create the new sensing paradigm needed to advance modern medicine and the field of bioelectronics¹³⁴. This may be possible through the use of nanoparticles as 'nano-BPEs'.

Nano-BPEs have been largely neglected for cellular applications due to the assertion that to polarize nano-BPEs a relatively high voltage was required (in the kV region, Equation (1-5))¹⁰⁷. This has been addressed by confining the BPEs within a nano- channel or pipette^{132,138,225}. However, most recent research, including the studies in Chapter 3, have indicated that BPEs are affected at much lower voltages (~ 20 V/cm)¹³³. These promising results suggest that nano-BPEs may be compatible with biology and therefore open up a wide range of possible applications (Figure 4-1:B). As discussed herein, *in vivo* nano bipolar electrochemistry could be used to grow in-situ bioelectronics¹¹², allowing for improved merging with individual cells. As nano-BPEs could be injected and wirelessly actuated, they may also bring new avenues of bioelectronic therapies to areas where implantable electrodes and devices are not possible. *In vitro* nano bipolar electrochemistry could be used to develop cellular sensing systems, particularly live cell, intracellular sensors that could shed light on the complexities of bioelectricity; This could add insight to the link between cell functions and bioelectricity, having great impacts on our understanding of the cancer phenotype⁴⁰.

Although our previous body of work demonstrated the use of direct current to wirelessly drive current at an intracellular BPE¹³³, we believe moving towards using alternating current could allow for better prospects of merging with biological systems due to the greater flexibility in tuning potentials by altering frequencies. Hence, the work herein aims to better understand the effect of alternating current on BESs, particularly those with intracellular nano-BPEs.

Other approaches exist to understand BPEs and optimize their use by facilitating carefully designed criteria to allow us to predict current flow through the BPEs. One approach includes equivalent circuit modelling using data from split BPEs or bespoke bipolar cells^{226–228}. Translating these methods to the nanoscale would be extremely difficult, due to the need to manufacture electronics to connect to individual nano-BPEs. Another possible method is electrochemically-modulated fluorescent probes¹³⁸. However, as this is an indirect method it is difficult to produce quantitative information and only BPEs are analysed, thus neglecting other cell elements (electrolyte/FEs). This approach also adds the process of fluorescently tagging electrodes and typical fluorescence imaging issues such as photobleaching and subsequent irreversibility. Hence, an alternative analytical method is required that can be easily applied to nano scale BESs. We hypothesized that Electrochemical Impedance Spectroscopy (EIS) would be suitable for studying the electrical components of nano-BPE systems as it allows for the assessment of a BES in

terms of its electrical circuit behaviour, without the need for physical connections to each component in the system.

EIS is a powerful tool capable of deconstructing total impedance into its capacitive, resistive and inductive contributions²²⁹ (section 1.2.4), and has been extensively used to study corrosion²³⁰. Other applications include material characterization^{231,232}, battery and fuel cell development^{233–235} and bipolar membrane characterization²³⁶. In more recent years the tool has drawn interest in the life sciences field due to its ability to reveal electrochemical properties such as diffusion coefficients, electron transfer rate constants, adsorption mechanisms and charge transfer resistances²³⁷. These applications are dominated by EIS based biosensors, for example for label-free sensing of DNA²³⁸, tuberculosis²³⁹, possible identification of osteoporosis²⁴⁰, and identification of thyroid cancer using 'EIS on a needle' (EON)^{241,242}. EIS has also been widely applied to living cells to non-invasively count, identify or monitor cellular functions²⁴³; state-of-the-art instrumentation is now available allowing the monitoring of cell adhesion, morphology, proliferation, and motion of cells (electrical cell-substrate impedance sensing – ECIS®)²⁴⁴. EIS is extremely practical and easy to carry out, whilst also being quickly repeatable. As seen by the wide array of applications, this makes EIS an attractive technique for analytical purposes. Importantly, to the best of our knowledge, it has not been used to study cellular BESs as proposed here and could be a highly valuable technique¹¹⁷ (Figure 4-1).

Herein, we report on a label-free EIS tool for direct modelling of the equivalent circuits of BESs. In our context here we refer to the NPs as BPEs, and we use them as capacitive sensors, as the BPEs will align in the field generating a potential difference across the particle. As seen in Figure 4-1:C, this was performed using 125 nm Au NP BPEs, in electrolytes including water and phosphate-buffered saline (PBS). These nano-BPEs were then combined with biological systems to establish if they could act as reporter BPEs within cells. These results indicate that electrical input parameters can be tuned to drive the electrical polarisation of NPs, which could be used to design systems to manipulate or sense cellular biochemistry wirelessly. As well as adding insight to the performance of nano-BPEs, this method also provides a wireless method for probing NPs that could have great sensing applications.

4.2. Methods

4.2.1. Electrode Manufacture

All electrodes were manufactured in house. FEs were fabricated using a Peltier cooled dual-target sputter coater (Emitech k575x) and 3D printed polylactic acid (PLA) masks (printed using an Ultimaker). As seen in Figure 4-2, electrodes were approximately 2 mm in width with a 1 mm gap between them. Sputter coating consisted of first coating with 20 nm of ITO (at 30 mA), as an adhesion layer, before coating with 100 nm (at 120 mA) of gold. Accurate™ spherical citrate stabilized Au NPs were purchased from Nano Partz™ with a \varnothing of 125 nm. Nano BPEs were prepared using an electrostatic coating of Au NPs in between the FEs at two concentrations: 50 and 12.5 $\mu\text{g}/\text{ml}$. Firstly, 20 μl of potassium hydroxide solution (1 M KOH in 60% ethanol) was pipetted between FEs and left for 1 hour. Following this step, two synthetic polymers with opposite charge, Poly (allylamine hydrochloride) (PAH) and Poly (sodium 4-styrenesulfonate) (PSS), were deposited for 30 minutes each. Polymer solutions were both 0.1 M in dH_2O . Finally, 20 μl of Au NPs was left to drop-coat overnight. Between all steps, and following Au NP modification, the electrodes were washed with dH_2O and dried with nitrogen.

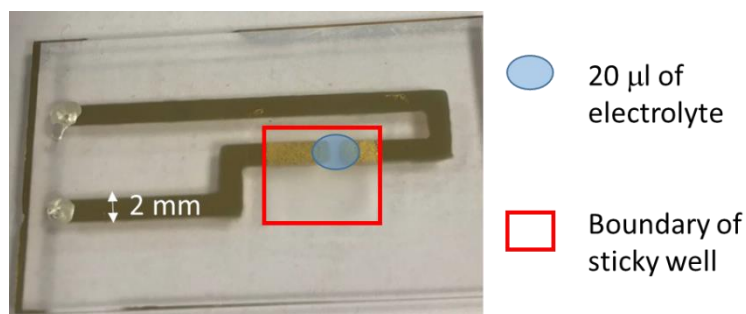


Figure 4-2 Au FE setup. FEs were approximately 2 mm in width, with a 1 mm gap between them. 20 µL of electrolyte was used to bridge the gap between electrodes, the approximate boundary of this droplet can be seen in blue. Samples with cells were produced using Ibidi® sticky slides, creating an approximate area of cell coverage of 1 cm², this can be seen in red. 20 µL of electrolyte was also added, however, this spread across the entire cell surface.

4.2.2. EIS Measurements

All impedance measurements were carried out using an Autolab potentiostat (Metrohm) with an applied AC amplitude of 0.01 V_{RMS} in potentiostatic mode. A two-electrode system was used, with a working electrode and reference/counter electrodes combined. Impedance was measured between 10 and 10,000 Hz, with a current limit set at 1mA. For high frequency measurements a high frequency module, attached to the potentiostat, was used (ECI10M). Ag conductive paint (RS components) was used to create larger contact areas to attach samples to the potentiostat via crocodile clips. A single droplet of 20 µL of electrolyte was used, as this was enough to just bridge the gap between FEs.

4.2.3. Surface Functionalization of Gold Nanoparticles:

Zinc(II) 5-(4-aminophenyl)-10,15,20-(tri-4-sulfonatophenyl)porphyrin triammonium (Zinc porphyrin) was covalently attached on gold nanoparticles (Au NPs) using an EDC/NHS coupling chemistry. In the first step, Au NPs were functionalized with 11-Mercaptoundecanoic acid (MUA) to introduce carboxylic groups. Briefly, 1 ml of MUA (100 μ M) in 1:9 ethanol/water was added to 5 ml of citrate capped Au NPs (100 μ g/ml). The solution was stirred overnight at room temperature under N₂ atmosphere. Later, the Au NPs were washed three times with water and centrifuged at 2500 rpm for 20 min to obtain MUA-capped Au NPs. In the second step, freshly prepared 1 ml EDC (100 mM) and 1 ml NHS (200 mM) were added to the MUA capped Au NPs to activate the carboxyl groups. The reaction was allowed to continue for 4 h under N₂. Then, 1 ml of zinc porphyrin (100 μ M) was added to this mixture and the solution was stirred at room temperature for 24 h under dark. Finally, the Au NPs were washed 3-4 times with water and centrifuged at 2500 rpm for 20 mins to obtain Au NPs conjugated with zinc porphyrin.

4.2.4. Cell Culture and Cell Experiments

Human glioblastoma cell line (U251s, ATCC) was cultured and expanded under standard cell culture conditions, antibiotic free, using culture medium (DMEM ThermoFisher Scientific) supplemented with 10% fetal bovine serum (FBS ThermoFisher Scientific) and 1% L-glutamine (ThermoFisher Scientific). The cells were passaged using trypsin. Cells were cultured onto microelectrode

samples using Ibidi sticky slides[®] at 500,000 cells and left for 4-6 hours to attach before running EIS measurements. For EIS measurements sticky slides were removed, all traces of media were first washed away by submerging samples in deionized water and then 20 μ l of electrolyte was added. During all experiments, deionized water (18.2 M Ω .cm) and sterile PBS (0.01 M, ThermoFisher Scientific) was used.

For cellular uptake analysis, 1.5×10^4 U251 cells were seeded on 13 mm glass viewing area of a 35 mm glass-bottom dish (ThermoFisher Scientific) and incubated at 37°C for 24 h. After 24 h, the culture medium was replaced with fresh medium containing 50 or 25 μ g/ml Au NPs (functionalized with zinc porphyrin) for 6 or 24 h. After each incubation period, the media containing the Au NPs was removed, and cells were washed thrice with PBS. The plasma membrane of the cells was stained using CellMask™ Green Plasma Membrane Stain (ThermoFisher Scientific) for 10 min. Later the cells were fixed with 4% formaldehyde for 5 min and subsequently washed 3 times with PBS. Afterward, cells were treated with DAPI for 5 min at RT under dark and washed again thrice with PBS. Finally, the cells were immersed in PBS and imaged using a Zeiss Elyra confocal microscope. Cellular uptake of Au NPs functionalized with zinc porphyrin was quantified by measuring the fluorescent intensity of at least 20 different cells using ImageJ. The fluorescent intensity values were normalized to the total number of cells per field and expressed as corrected total cell fluorescence (CTCF) obtained by applying Equation (4-1).

$$CTCF = \text{Integrated density} - (\text{Area of selected cell} \times \text{Mean fluorescence of background signal})$$

Equation (4-1)

To further study the cellular uptake of Au NPs, inductively coupled plasma mass spectroscopy (ICP-MS) was carried out (iCAPQ ThermoFisher Scientific with bare Au NPs. Using the same methods as described for confocal microscopy, ICP-MS samples were prepared by digesting samples in 5% aquaregia overnight, before then being diluted with milliQ water to reach a final acid concentration of 2%²⁴⁵.

Toxicity of Au NPs used in this work was analysed using membrane/membrane permeable dyes (Hoechst/Propodium Iodide) and a metabolic activity assay (WST-8). For membrane damage analysis, U251 glioblastoma cells were seeded at a density of 8×10^3 cells/well in a tissue culture-treated black glass-bottom 96-well plate. After 24 h incubation, media was replaced with fresh media containing Au NPs and further incubated at 37°C and 5% CO₂. After 24 h, the cells were gently washed thrice with PBS to remove any unbound Au NPs. Next, 100 µl of PI solution (0.5 mg/ml in PBS, Sigma) was added followed by incubation for 10 min at 37°C and 5% CO₂. Later, cells were washed twice with PBS and 100 µl of Hoechst 33342 (ThermoFisher Scientific) was added to each well and incubated for 30 min at room temperature. Finally, the cells were washed thrice with PBS and the cells were imaged using Nikon

Eclipse Ti with DAPI and mCherry filter. Corrected total cell fluorescence as a function of PI fluorescence (membrane damaged cells) was calculated using ImageJ. The statistical significance was calculated by using a one-way ANOVA test on at least 100 cells per sample on GraphPad Prism 7.01. For metabolic analysis, U251 cells were seeded into a 96-well plate at a density of 10×10^3 cells/well and incubated for 24 h at 37 °C and 5% CO₂. Afterwards, culture media was replaced with fresh media containing Au NPs at different concentrations (12.5, 25, 50, 100, and 500 µg/ml) and incubated for 24 h. Next, the media was replaced with a mixture of DMEM containing 10 % WST-8 and incubated for another 1 h at 37 °C and 5% CO₂. Finally, the absorbance of the plate was read at 450 nm using a Tecan microplate reader. All the experiments were performed in triplicate.

4.3. Results and Discussion

4.3.1. Theoretical Framework

Our first step in designing an analytical tool, that could be used to help us understand how BPEs behave under an electric field, was to model them using a simplified equivalent circuit with three circuit elements. These elements are the impedance of the FEs (Z_F), the impedance of the BPEs (Z_B) and the 'bypass impedance' of the electrolyte (Z_E). Figure 4-3 (inset) shows the configuration of these components for samples with BPEs, without cells.

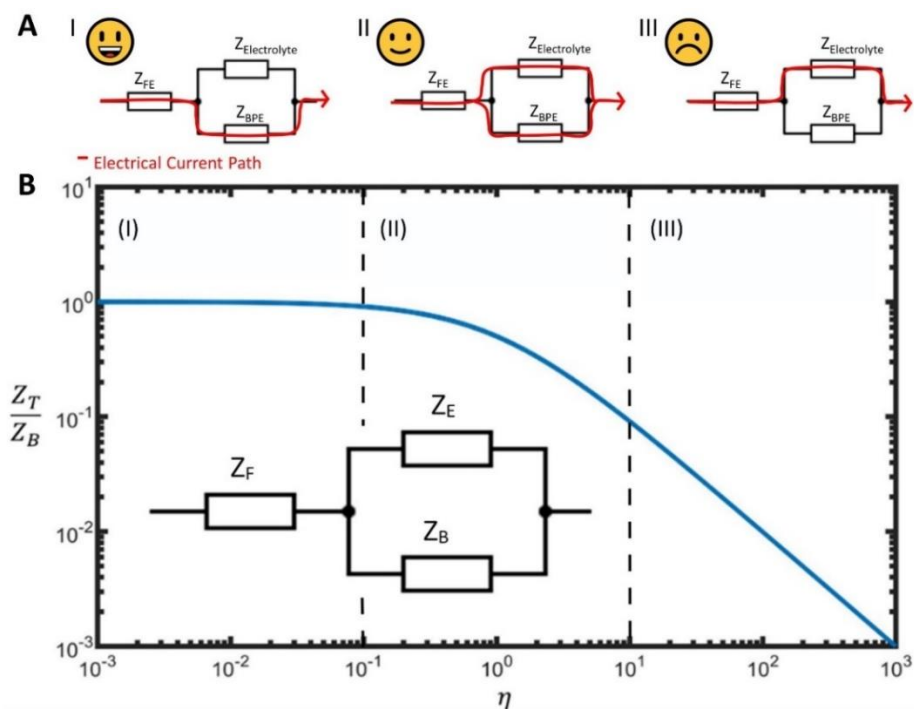


Figure 4-3 Basis of EIS method to evaluate BESs, by evaluating the ratio of BPE impedance and electrolyte impedance. Total BES impedance (Z_T), normalized by BPE impedance (Z_B), is plotted against efficiency parameter η (defined in Equation (4-2)) (B). An equivalent circuit can be seen in the inset, with impedance components relating to the FEs Z_F , the electrolyte Z_E , and the BPEs Z_B . Dotted lines show the three distinct areas (I – III) where current flows mostly through the BPEs, is split between BPE and electrolyte, and mostly flows through the electrolyte (A).

An impedance-based parameter was then introduced with the ability to quantitatively-describe the efficiency of these BESs in driving current. The efficiency parameter (η) is defined as the ratio of the impedance of the BPEs (Z_B) to the bypass impedance of the electrolyte (Z_E), as described by (Equation (4-2)). This parameter does not include the FE (Z_F) as its effect on the overall cell impedance is negligible, exerting an impedance in series with the overall impedance of the bipolar system.

$$\eta = \frac{Z_B}{Z_E}$$

Equation (4-2)

$$Z_T = \frac{Z_E Z_B}{Z_E + Z_B}$$

Equation (4-3)

To investigate the influence of the efficiency parameter on the total cell impedance, we can model a BES with a fixed Z_B and varying Z_E . As seen in Figure 4-3, by calculating total impedance (Z_T), using Equation (4-3), and normalizing using Z_B , we can plot normalized total impedance against the efficiency parameter, giving three distinct regions of η . The equation can be described in a simple manner: if the electrolyte impedance is significantly lower than the BPE impedance then current flows through the electrolyte and vice versa.

In the range where $\eta \geq 10$, Z_T is dominated by Z_E ; this case occurs when a highly conductive electrolyte is used (Figure 4-3:A and B III). Here current will favour the electrolyte, meaning little to no current would pass through the

BPEs, therefore being undesirable in driving electrochemical reactions. As Z_E increases the electrolyte becomes more resistive, falling within the range of $0.1 < \eta < 10$, Z_T begins to reflect both Z_E and Z_B (Figure 4-3:A and B: II). This is due to impedance values becoming more similar and hence current tends towards equally splitting between the two components. Finally, when η falls below 0.1, the overall impedance is then limited only by Z_B (Figure 4-3:A and B: I). This shows that when a highly resistive electrolyte is used, current would then favour the BPEs with little to no current passing through the electrolyte. In order to drive electrochemical reactions at the BPE, and to probe any changes in the BPEs, current is required to pass through the BPEs. Hence, we can conclude that $\eta \leq 10$ must be satisfied when using this analytical method. A similar concept has previously been described, though not using impedance spectroscopy as in this study¹⁰⁷. Previous studies required physical connection or labelling of the BPEs to assess electrical behavior^{138,226,228}. Utilizing impedance spectroscopy provides a much simpler, label-free, wireless method that allows the analysis of nano-BPEs for the first time.

4.3.2. Nano BPE systems

Before exploring how BESs behave in the presence of cells, we first validated the above theoretical framework by varying electrolytes only. The BES consisted of gold FEs with spherical Au NP BPEs placed in between. Au NPs are commonly used for *in vivo* applications²¹³; furthermore, we have recently developed bioelectronic systems using Au NPs in which we observed that they

could act as electrical antennae within cells¹³³. They would therefore be suitable for establishing an EIS analytical protocol to study the effects of nano sized BPEs in biological systems. A larger diameter particle is used herein (125 nm) to allow for higher charge density and compatibility with other techniques, such as assessing plasmonic effects¹³³.

In order to test the effect of varying Z_E and hence experimentally validate the above model (Figure 4-3), samples were tested in high and low impedance electrolytes: deionized water and PBS respectively. A range of concentrations of PBS were also studied to further test the hypothesis that increasing Z_E allows for the increased efficiency of the system (η) (Figure 4-4). It is important to note that this is not to simulate *in vivo* conditions, but to assess how these nano BESs behave in high and low impedance electrolyte examples. When looking at samples without BPEs, we saw no change in shape of the Nyquist plot. All concentrations exhibiting a 45° slope which is characteristic of Warburg impedance due to diffusion limits. When BPEs are present we saw a change in the graph's shapes at high frequencies as you approach low PBS concentrations and deionized water. This semicircle that begins to form is due to a capacitance being introduced from the BPEs. This validates the theoretical framework showing that increasing impedance of electrolyte allows for increasing current driven through the BPEs shown by the increasing semicircle size.

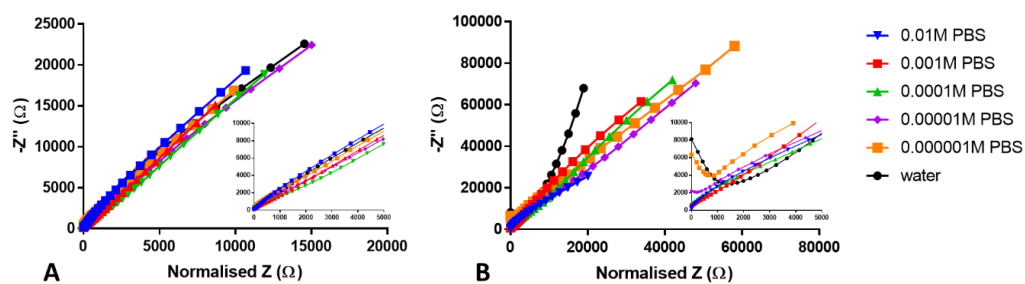


Figure 4-4 Varying PBS concentrations were tested in systems with (B) and without (A) Au NP BPEs.

Real impedance was normalized to allow Nyquist plots to be overlaid. Insets show expanded lower frequency portion of graphs.

Subsequently, we then analysed the resulting frequency impedance plots by least squared fitting to construct equivalent circuits (Figure 4-5). Warburg impedance was also included in series with the FE to account for diffusion in the system and to allow for better fitting. However, it was found that these values were not significantly different between repeats and hence are not discussed. All results satisfied the Kronig-Kramer's test, showing that the system is linear and stable with time, which is a prerequisite for modelling. Both FEs and BPEs are adequately described by a capacitor which represents the electrochemical double layer, in the absence of charge transfer across the interface, and therefore $Z_{F/B}$ are modelled as $C_{F/B}$. When deionized water is used as an electrolyte, the impedance of Au NPs is lower in comparison to Z_E , resulting in current flow through the BPEs. As the current passes through BPEs capacitively, an additional capacitor appears in the equivalent circuit accounting for this effect (Figure 4-5:A). In contrast to deionized water, when PBS is used most current flows through the electrolyte, the impedance of BPEs is relatively high and therefore behaves as an open circuit (Figure 4-5:B). As PBS

is more physiologically relevant to intracellular space than deionized water, BPE concentration will be extremely important to drive current in the presence of cells, which we describe later in the text. Due to the practicality of this method, equivalent circuits are much easier to produce when compared to previous methods for probing BPEs^{226–228}.

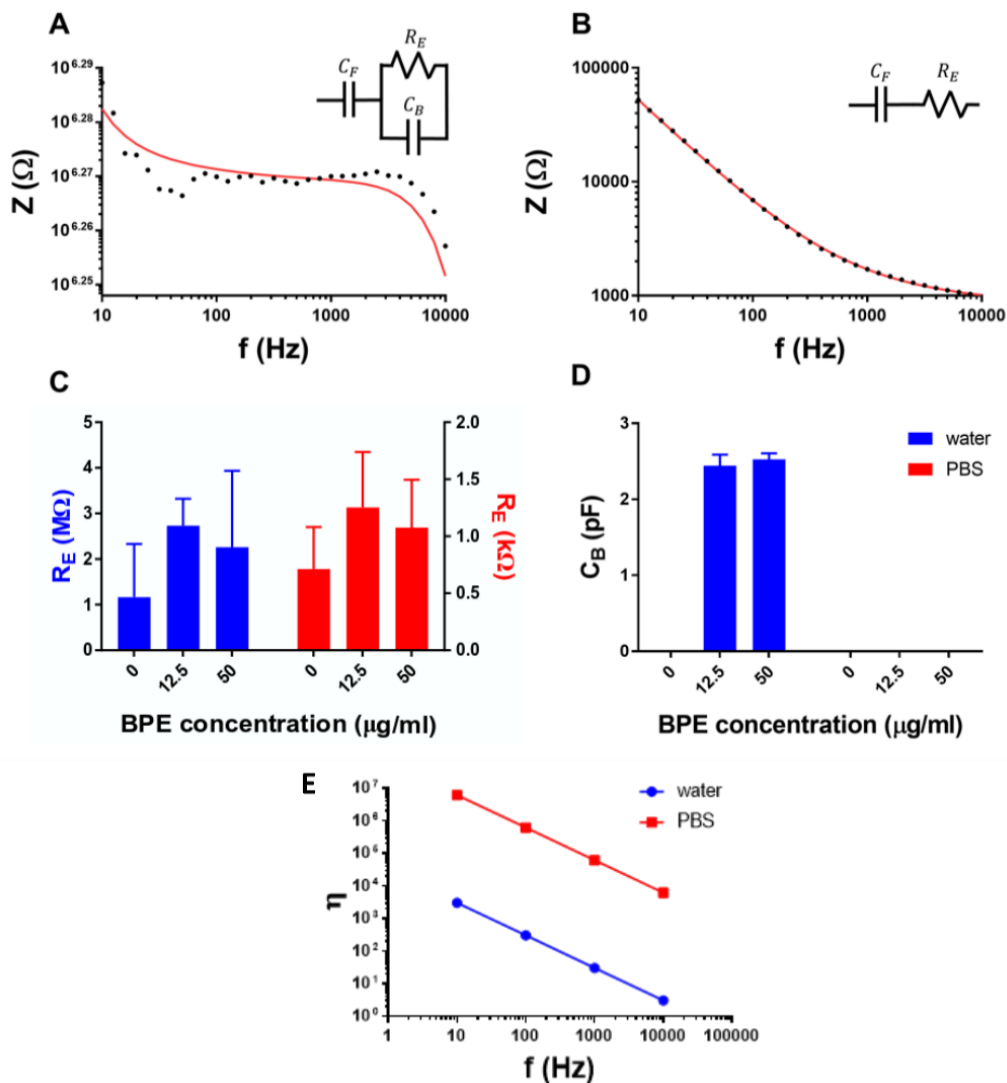


Figure 4-5 Electrical characterization plots and example circuit fittings of Au FEs with Au NP BPEs in water (A) and PBS (B). Circuit diagrams can be seen in the inset. Warburg impedance was included in series with FEs to account for diffusion in the system and allow for better fitting. With Z_E being modelled as a resistor (R_E) and Z_B modelled as a capacitor (C_B), (C) and (D) show the average magnitudes of R_E and

C_B respectively in samples using water (blue) and PBS (red). C_F averages can be seen in Figure 4-6. Error bars show standard error of mean ($n = 3$). Efficiency parameter (η) of 125 nm Au NP BPEs in PBS (blue) and deionized water (red) can be seen in (E).

Bode plots shown in Figure 4-5:A and B for deionized water and PBS respectively, confirm that the BESs do behave differently with varying electrolyte impedance. In water, there are three distinct sections of the impedance spectrum. At low frequencies, the impedance is limited by the capacitive nature of the FEs. This shows a typical frequency dependent behaviour, described in Equation (4-4), where impedance drops by increasing frequency. The second region is characterized by a constant impedance occurring within the frequency range 100 - 3000 Hz. This component arises from the resistance of charge flow (i.e., Z_E , electrolyte impedance). When this is described in terms of the theoretical framework, previously described in Figure 4-3, the parameter $\eta \geq 10$ for this region. This means, within this region, the electrolyte impedance is still relatively lower than the BPE impedance and therefore is limiting the overall impedance. As the BPE is also behaving as a capacitor, its impedance is also frequency-dependent; hence, the impedance of the BPEs becomes less than the impedance of the electrolyte for the frequency range $\sim 3000 - 10,000$ Hz. This means current flows through the BPE when $\eta \leq 10$ is satisfied. It can therefore be concluded that to probe these nano-BPEs using impedance spectroscopy within deionized water, measurements should be performed at frequencies higher than ~ 3000 Hz when

relatively low voltages are applied. Although the reported frequency band is only suited to the BES described above, the concept can be adapted to probe remotely induced electrochemical reactions. To achieve this, a suitable frequency region should be identified since the electrochemical impedance of BPE-electrolyte interface changes with redox charge transfer. It is worth noting that there is a possibility of driving current at low frequencies if higher voltages are applied, as we have observed previously¹³³. Within PBS, Figure 4-5:B, we only observe two disparate sections of the curve relating to: (i) the capacitive effect of the FEs at lower frequencies; and (ii) plateauing to the resistive effect of the electrolyte at high frequencies. As expected, the addition of BPEs does not significantly change the impedance spectra, indicating we are working within the region of $\eta \geq 10$ with little to no current flowing through the BPEs. As within deionized water, it is expected that at much higher frequencies the BPEs may then be able to be sensed due to their decreasing impedance.

$$Z = \frac{1}{j\omega c}$$

Where $j = \sqrt{-1}$, ω = angular frequency or $2\pi f$ and c = capacitance

Equation (4-4)

We were then interested in determining how the different BES components are behaving, which would yield knowledge to better understand and design systems. The average of the equivalent circuit components from

three independent repeats is plotted in Figure 4-5:C and D. These plots present the electrolyte resistance (R_E) and the BPE capacitance (C_B) respectively. FE behaviour is not discussed here as it has low impedance in series with the BES and does not greatly affect the BPEs, however results can be seen in Figure 4-6 below.

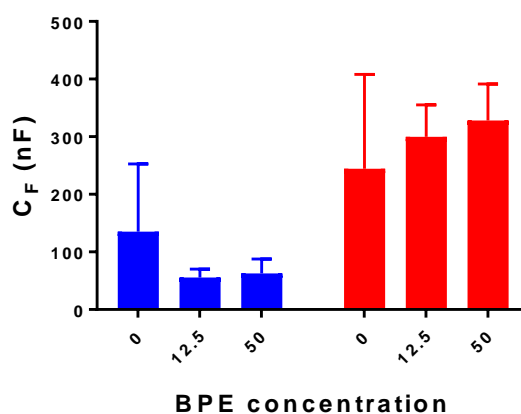


Figure 4-6 Average magnitudes of FE capacitance in water (blue) and PBS (red), from circuit fittings used in Figure 4-5.

As seen in Figure 4-5:C, the resistance of deionized water is in the order of M Ω , as expected due to the low concentration of ions; values are reasonable as the dH₂O resistance is rated at 18.2 M Ω .cm and there is a 1 mm gap between electrodes. PBS impedance is in the order of k Ω , also reasonable for this electrolyte concentration²⁴⁶. The results presented show that the electrolyte impedance is not affected by the presence or absence of the BPEs, as no significant difference in resistance is witnessed. This observation further confirms the robustness of the technique in extracting the components of the BES. As anticipated from the theoretical framework in Figure 4-3, the BPEs are

detected in the deionized water, rather than in PBS as presented in Figure 4-5:D. The BPE component was not included when modelling samples in PBS and with no nano-BPEs, due to markedly better fitting being achieved (this can be seen in Figure 4-7). Au NP BPEs were used in 2 concentrations to determine if the method was sensitive to such differences: 50 $\mu\text{g/ml}$ and 12.5 $\mu\text{g/ml}$. No difference was seen between these two concentrations, which we believe to be due to the signal to noise ratio. We later use a concentration of 500 $\mu\text{g/ml}$ as we expected a higher magnitude in concentration would show a change in capacitance values allowing for intracellular experiments.

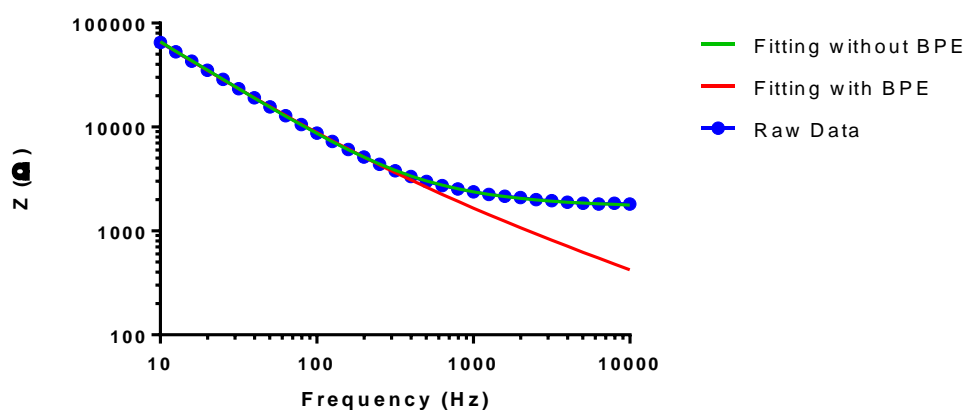


Figure 4-7 Raw data of bipolar system with Au NP BPEs in PBS. Fitting lines show fitting with (red) and without (green) the BPE component.

Given the capacitance of BPEs calculated from equivalent circuits in Figure 4-5:D (~ 2.5 pF), we then calculated the efficiency of these BPEs in different electrolyte systems by calculating η (using Equation (4-2) and Equation (4-4)). It is important to note that the capacitance of the BPEs would

change in PBS and an estimate of this value was not possible due to no current flowing through the BPEs. However, when applying Equation (4-2) and Equation (4-4), even a magnitude difference in capacitance will have little effect on η , therefore this will allow a rudimentary comparison between water and PBS. This comparison, seen in Figure 4-5E, shows that η falls below 10 when in the water at frequencies higher than ~ 3000 Hz, again suggesting that we can drive current through these BPEs under these conditions and not when using PBS. As expected, this highlights the need for a high impedance electrolyte for these Au NP BPEs to be addressed by EIS in sensing applications.

4.3.3. Living Cells with Nano BPEs

The development of bioelectronic systems that use conductive NPs to sense and actuate cellular behaviour would be an extremely important advancement for cancer diagnosis and treatment^{59,247}. Consequently, we used the assay to study how Au NP BPEs behave when placed within U251 malignant brain cancer cells. To determine whether current would flow through BPEs when cells are present, U251 cells were seeded onto samples without nano-BPEs, as well as with intracellular nano-BPEs. Again, high and low impedance electrolytes of water and PBS respectively, were used. We have previously shown that the short time frame of these experiments (< 1 min) using water does not affect cell viability¹¹².

To provide intracellular nano-BPEs, cells were incubated with Au NPs, before seeding cells onto FEs. Cellular uptake was expected to be via endocytosis²⁴⁸. As seen in Figure 4-8, the cellular uptake of Au NPs was confirmed using confocal microscopy. To achieve this, we covalently conjugated fluorescent Zinc(II) 5-(4-aminophenyl)-10,15,20-(tri-4-sulfonatophenyl)porphyrin triammonium (zinc porphyrin) to these Au NPs (Figure 4-9). For comparison purposes, two concentrations of Au NPs were tested along with two incubation times: 50 or 25 $\mu\text{g}/\text{ml}$ and 6 or 24 hours. Both the higher concentration (50 $\mu\text{g}/\text{ml}$) and the longer time frame (24 h) showed significantly higher Au NPs inside cells and hence, 50 $\mu\text{g}/\text{ml}$ for 24 hours was used for experiments herein. It is important to note that zinc porphyrin is not intended for use in the final concept as it may be cytotoxic²⁴⁹; as seen in Figure 4-8 cytotoxicity was not significant using these functionalised NPs.

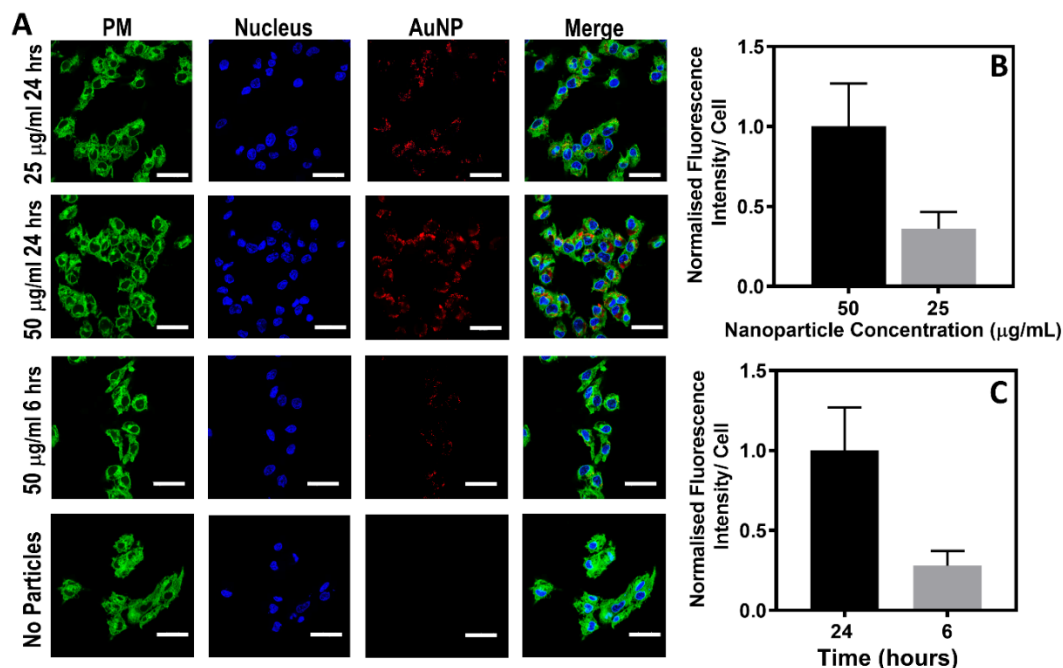


Figure 4-8 Cellular uptake analysis of Au NP BPEs comparing two concentrations of Au NPs and two incubation times. Confocal microscopy was used to image U251 cells incubated with Au NPs conjugated with Zn porphyrin (A). All scale bars represent 50 μm . Mean cell fluorescent intensity as a function of cellular uptake and SD was plotted for at least 20 cells (B) & (C). All the values were normalized with fluorescent intensity obtained with Au NP concentration of 50 $\mu\text{g/ml}$ (B) or Au NP incubation time of 24 hours (C). 50 $\mu\text{g/ml}$ Au NP concentration was taken forward from B to perform the incubation time study in C.

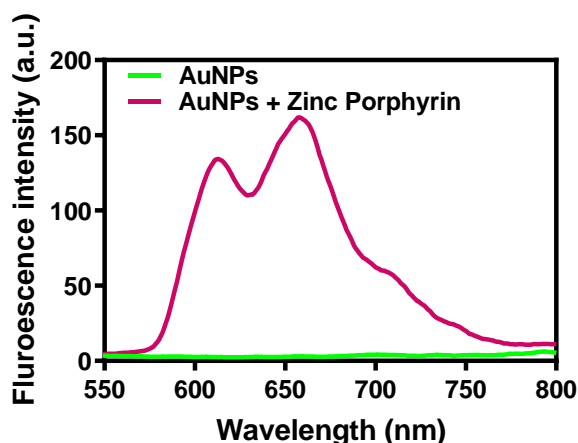


Figure 4-9 Fluorescent emission spectrum of Au NPs functionalized with zinc porphyrin monitored upon excitation with a wavelength of 422 nm.

We also performed inductively coupled plasma mass spectroscopy (ICP-MS) for cellular uptake analysis of Au NPs, to support the obtained confocal data (Figure 4-10). Considering both confocal imaging and ICP-MS results, using porphyrin functionalized and bare Au NPs respectively, we can be confident that Au NPs are being taken up by the cells.

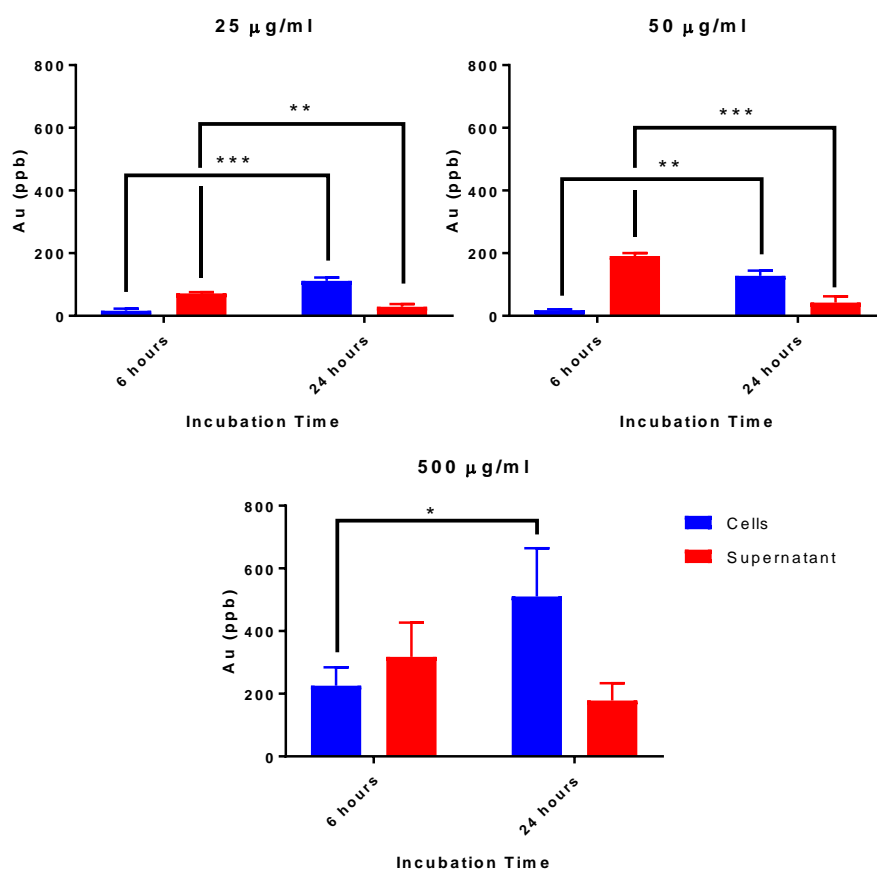


Figure 4-10 Inductively coupled plasma mass spectrometry (ICP-MS) results for 25, 50 and 500 µg/ml of Au NPs incubated with U251 cells for 6 or 24 hours.

To ensure any effects were not as a result of impedance changes associated with the Au NPs toxicity, toxicity was analysed using a membrane dye (Hoechst/Propidium Iodide) and a WST-8 metabolic activity assay. All used

concentrations of Au NPs had no significant effect on viability and little effect on metabolism, with metabolic activity not dropping below 80% (Figure 4-11), and this agrees with others who have shown high Au NPs concentrations do not significantly affect cell metabolism²⁵⁰.

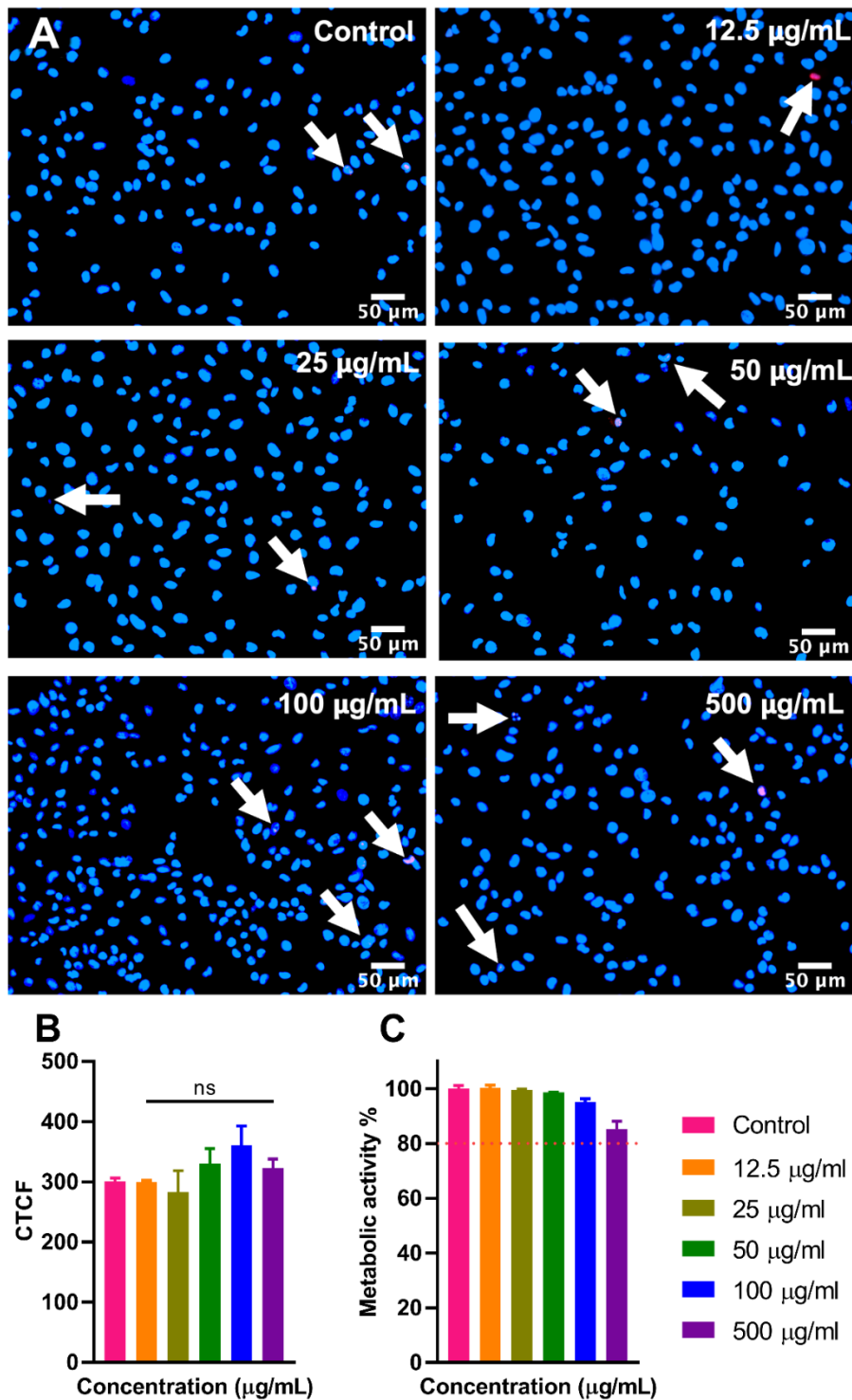


Figure 4-11 Analysis of toxicity effects of varying concentrations of Au NPs (from 12.5 µg/ml to 500 µg/ml) on U251 cells. Fluorescence microscopy images of U251 cells treated with Au NPs at different concentrations. Blue: represents Hoechst staining (blue, all cells); White arrows: represent PI staining (red, membrane damaged cells). Scale bar is 50 µm (A). Corrected total cell fluorescence of red PI

fluorescence (membrane damaged cells) quantified in the area of the cells using imageJ. Statistical significance was calculated using a one-way ANOVA test ($n = 100$; error bar represents SD; triplicate) (B). Metabolism of U251 using WST-8 assay (Cell Counting Kit Sigma Aldrich). Metabolic activity was normalized as a percentage of a control well without Au NPs (C).

Despite EIS being applied to many biological applications, to the best of our knowledge, only one previous study exists comparing the impedance of tissue with and without the presence of conductive objects (Au NPs)²⁵¹. Measurements are taken at low frequencies and circuits are not fitted, so the behaviour of such Au NPs cannot be quantified. Here-in, impedance measurements were taken covering a higher frequency range of $0.1 - 10 \times 10^7$ Hz. This fully covers the range of frequencies usually used to study cells using EIS and allowed us to fit circuits to better explain the systems²⁵². High frequency impedance has previously been shown to be able to be used to study nonlinear systems, which is likely to be the case when cells are present²⁵³. Furthermore, the higher frequencies are believed to be more affected by cell membranes, whereas lower frequencies are more affected by solution channels under and between adjacent cells²⁵². It is also reported that the impedance of the cell membrane drops significantly at MHz frequencies and it effectively acts as a short circuit⁶⁶. Therefore, there is a better scope to probe intracellular BPEs at these higher frequencies. Moreover, unlike raw spectra, resistance, and capacitance values from fitting, are normally distributed, passing a Shapiro-Wilk normality test ($p > 0.01$), allowing us to discern significant differences more easily. The higher concentration was chosen to be

studied at high frequencies (50 $\mu\text{g/ml}$), as well as a ten-fold higher concentration, to maximize the chance of sensing intracellular BPEs (500 $\mu\text{g/ml}$).

As performed with samples without cells, circuit fittings were carried out to better understand how the systems are behaving. These were approximated fits representing the components of the plots that were indicative of the cells and nanoparticles. Upon analysis of the samples in water, we elucidate that we have two-time constants, represented by the two semi-circles in the Nyquist plots, and an increase in the phase angle at higher frequencies (Figure 4-12:A and B). These phenomena are not present in the PBS data and hence a different circuit was required for the different electrolyte samples. However, both setups are sensitive to the presence of the BPEs inside cells, as demonstrated in Figure 4-13A. As seen in Figure 4-12:C and D, these circuits included FE capacitance (C_F), in series with an RC circuit with electrolyte resistance R_1 , and capacitance we believe to be linked to the cells C_1 . Water samples included a second RC circuit with a second resistance and capacitance (R_2 and C_2).

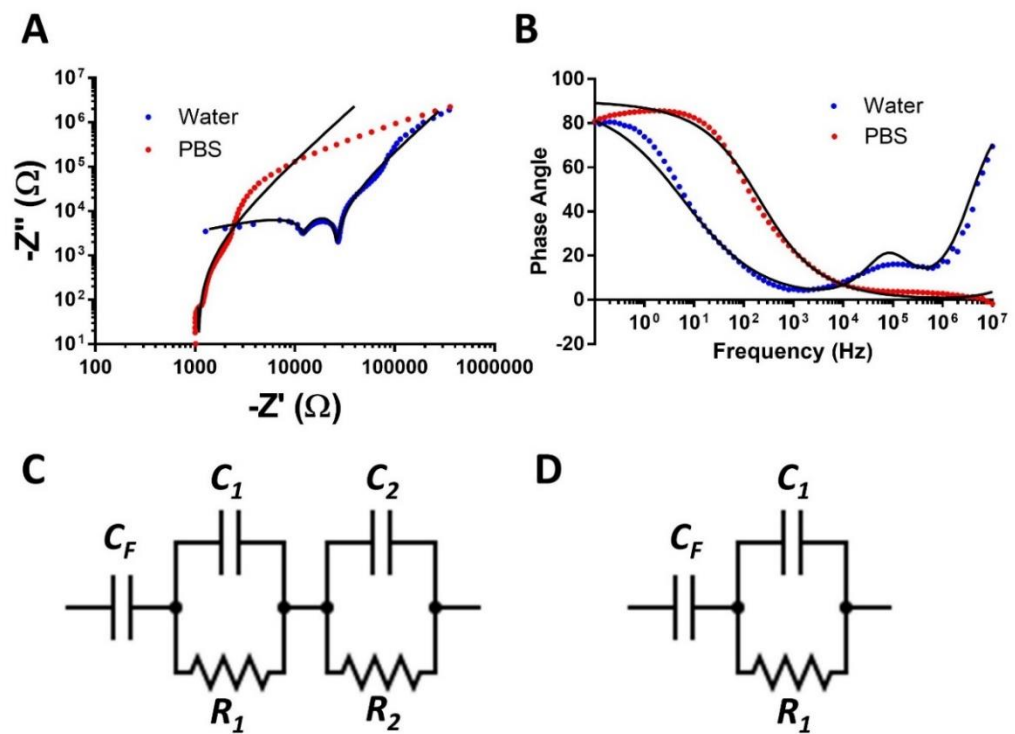


Figure 4-12 Example data of samples with Au NPs and cells present, using water as an electrolyte. Nyquist plots (A) and Phase angle (B) are plotted, with fitting data overlaid in black. (C) and (D) show circuits fitted to water and PBS respectively.

The above simple circuits were fitted to the experimental data and the circuit components are presented in Figure 4-13. Sample fitting can be seen in Figure 4-14. As expected, C_F values were not significantly different across all samples and hence will not be discussed (values can be seen in Figure 4-15). R_1 values were also not significantly different within the electrolytes, suggesting the main contributor to this is the resistance of the electrolyte used. We do however observe a significant difference in C_1 values when comparing the highest concentration of Au NPs to the case of low concentration or absence of Au NPs. Due to this, we can conclude that the capacitance C_1 is associated with the intracellular ionic differences and therefore the reported analytical method

is sensitive to the presence of Au NPs in the intracellular space. This is supported by the evidence we provided that Au NPs are inside the cells, which was demonstrated using ICP-MS and fluorescent studies. If the capacitor was linked to the cellular component alone then the Au NP concentration would have no effect; therefore, this importantly indicates that we can sense Au NPs inside the cells in both water and PBS. These findings show that measurements can be performed in PBS, which will provide a better mimic of physiological conditions and allow for longer-term studies. We predict that the lower capacitance at higher Au NP concentrations is due to Au NPs agglomerating inside cells. This agglomeration would provide BPEs with a smaller surface area and therefore lower capacitance.

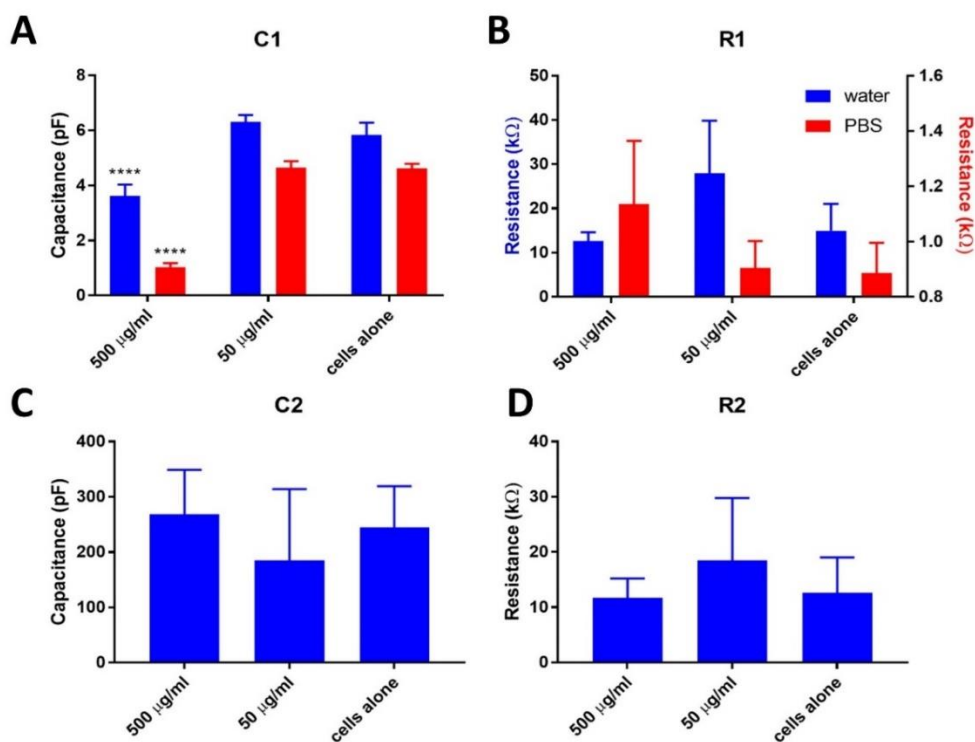


Figure 4-13 Comparison of fitting values from samples with cells and Au NPs at two concentrations: 50 and 500 µg/ml. Capacitance (C) and resistance (R) values from circuit fittings can be seen using water (blue) and PBS (red) as electrolytes. FE capacitance values can be found in Figure 4-15. Circuits used can be seen in Figure 4-12. Error bars show standard error of the mean (n = 3). Significant differences (*) were assessed using two-way ANOVA and Tukey's multiple comparison test.

This is the first evidence that Au NPs can act as BPEs to sense electrical input as previously suggested by us¹³³. This exciting finding suggests that the proposed impedimetric characterization can be used to detect cell-NP interfacing and probe the flow of therapeutic current through these BPEs. This could provide a well needed new sensing paradigm, whereby functionalized NPs can be used to probe intracellular bioelectricity.

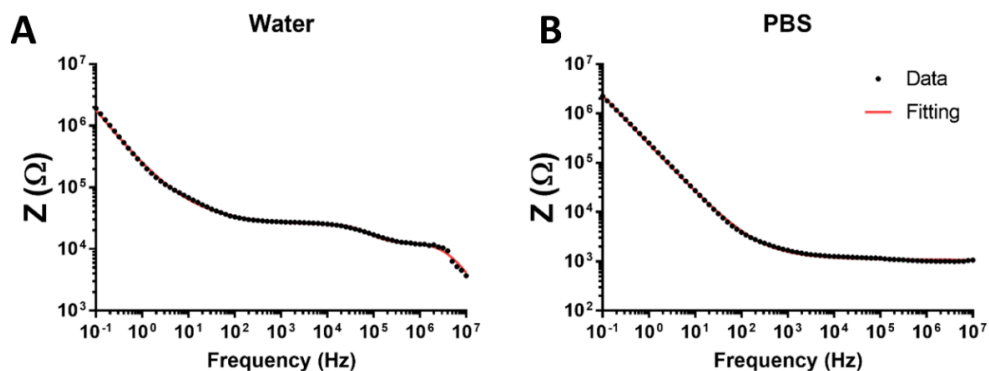


Figure 4-14 Graphs showing sample fitting of raw data of systems with living cells, in water (A) and PBS (B). Such fitting was used to determine resistance and capacitance values seen in Figure 4-13.

Considering water samples only, we witness a second RC circuit. Again, R_2 is similar in magnitude to the electrolyte resistance and so this is likely to be the main contributor. As for C_2 , we believe this to be linked to the cells themselves acting as BPEs, due to the presence of the Au NPs having no effect on the capacitance.

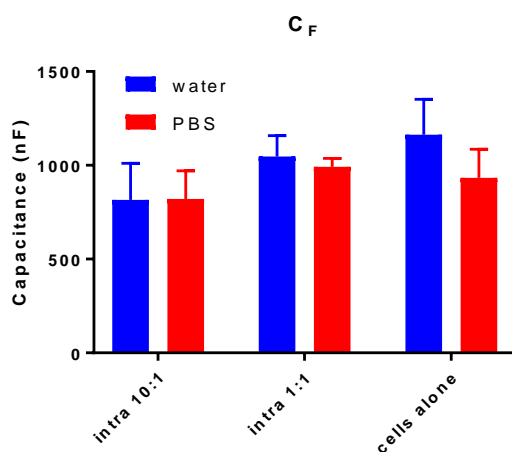


Figure 4-15 Average magnitudes of FE capacitance in water (blue) and PBS (red), from circuit fittings used in Figure 4-13.

These results show that within these conditions, nano-BPEs can be used as electrical sensors when in the intracellular space. Coupled with the ease of

functionalisation on NPs, this could have great intracellular sensing application. Previous BPE-based biosensors often require cell lysis with analytes then placed onto BPEs²⁵⁴, or the piercing of individual cells with a nanopipette¹³² whereas the use of EIS as shown here-in would allow for non-invasive live monitoring of intracellular BPEs for the first time. Further optimization could allow the generation of useful currents at the BPEs for actuation applications. This could then allow for the use of nano-BPEs in targeting or enhancing electric fields, growing *in vivo* electronics and actuating cellular functions (Figure 4-1B). This could therefore provide an exciting new sensing and actuation paradigm, that is needed to progress the field of bioelectronics¹³⁴.

4.4. Summary and Conclusions

This work provides advancing knowledge on the application of nanoscale BPE systems in cells, which until now was lacking. As applied herein, EIS allows a simple way to evaluate a BPE system and model its equivalent circuit. Such a method is both simpler than existing methods^{138,226–228} as well as being possible with nano-BPEs for the first time.

Here we propose an impedimetric method of evaluating the efficiency of a BPE and electrolyte combination. By modelling total impedance in relation to BPE and electrolyte impedance, we propose the efficiency parameter η . We then validate this model experimentally using Au NP BPEs and high and low impedance electrolytes: deionized water and PBS respectively. This confirms that within these conditions, these BPEs can be probed in water at high frequencies, but not in PBS.

Further to this, we introduced cells to the system to aid in determining if Au NP BPEs can be used as bioelectronics for sensing electrical input. High frequency measurements were taken to allow for circuit fittings. Within this system, intracellular BPEs at a concentration of 500 $\mu\text{g/ml}$ show a significant difference from cells alone, in both water and PBS. This suggests that current is being driven through them. This is a key finding suggesting that nano-BPEs could be used as electrical sensors within the intracellular space, and also

highlights the efficacy of EIS as a non-invasive technique for probing nano-BPEs, both with and without biological systems.

Chapter 5. Conclusions and Future Work

5.1. Final Discussion and Conclusions

Bioelectronic medicine is an exciting field of study, capable of bringing novel therapies and diagnostics to some of today's most challenging health burdens. A shift is needed to fully exploit electroceuticals, whereby flexible electronics with 3D interfaces are manufactured to seamlessly merge with biological systems. As discussed herein, this may be possible through the in-situ growth of bioelectronics using bipolar electrochemistry. Such novel bioelectronics could have implications in a wide range of therapies, particularly cancer.

To develop in-situ grown bioelectronics with bipolar electrochemistry, the first aim herein was to further understand and control the growth of MWs. BESs are first optimised without biology. Varying geometries and orientations are investigated to show that designs of BPEs can be precisely created to direct wire growth without having detrimental effects on wire function. This was shown by characterising MW diameter and resistance. It is then demonstrated that MW diameter can be controlled by using AC stimulation to elicit MW growth. This allows for wire diameters as low as 0.5 μm , which could prove useful in bioelectronic applications as this is a similar size to cellular components such as organelles²⁵⁵. In the final sections of Chapter 2, proof of

concept studies are shown that show promise for utilising bipolar electrochemically grown MWs for the *in vivo* growth of bioelectronics. The growth of MWs in a 3D cellular environment is shown for the first time. Following this, MWs are then grown wirelessly using the addition of a metal salt for the first time, suggesting that an injected metal salt may provide the source of MWs grown using *ex vivo* FEs. The aims set out in this chapter were met, with the work herein now allowing for improved control of MW growth in terms of direction and MW characteristics.

Other outcomes that are expected from the body of work included in Chapter 2 are to improve the information processing density and cellular integration of bioelectronics. 2D planar bioelectronics show exciting possibilities in sensing and actuating biology²⁵⁶; however, in general, they are limited to only analysing the surface of a sample. 3D electronics remove this limitation and penetrate tissue to collect a wider range of signals. Examples of such 3D bioelectronics have been recently extensively reviewed²⁵⁷; these mostly include microelectrode arrays that are pre-made before interfacing with biology, using standard manufacturing methods such as photolithography and 3D printing. 3D bioelectronics are thought to improve information processing by having a large surface area and complete coupling of the biointerface²⁵⁷. Although not directly studied, the alternative micro-fabrication method optimised in Chapter 2 is capable of doing just this. The structure of the MWs, made up of many NPs, provides the MWs with a relatively large surface area.

Furthermore, by growing the MWs into tissue they may penetrate further and may better conform to the heterogenous, irregular structure present within biological systems. An interesting future study could be to use these structures to record bioelectricity and compare readings relative to those generated from 2D bioelectronics and 3D pre-manufactured bioelectronics. It is hypothesised that this 3D in situ grown bioelectronics could provide superior performance.

A final consideration for merging bipolar electrochemically grown MWs with biological systems is to limit the cytotoxic effects associated with the MW growth. As shown previously¹¹², AC stimulation may allow for reduced cytotoxicity, although herein AC stimulation was not capable of growing MWs in the presence of cells. As earlier discussed, using higher frequency AC inputs may allow for the increased impedances imposed by cells to be overcome. Further studies are necessary to find optimal inputs for growing MWs and these inputs will likely vary for differing cell types. With diverse cell types having different structures, sizes, membrane potentials etc. it is understandable that varying tissues exhibit specific bioimpedance. This impedance will directly affect the electrical inputs needed to grow MWs and hence optimisation for all possible applications would be required. This means cytotoxicity studies will also be needed for multiple cell types. An additional concern to cytotoxicity is the MWs themselves; they may elicit unwanted immune responses or damage cells during their growth. It is hypothesised that within a tissue environment, MWs would grow through the path of least resistance. This is expected to be

through the extracellular matrix; however, some MWs may penetrate into the intracellular space. Further 3D wire growth studies are required to determine this. This may be possible using similar methods described herein with 3D cell spheroids. FEs should be placed inside the spheroids to assure that MWs grow through the spheroids rather than around them. Cross-sections of spheroids could then be analysed to visualise whether MWs damage cells. If MWs do penetrate cells, this would also be an extremely impactful finding as this would suggest that wirelessly grown MWs could be used for high-throughput intracellular recording and stimulation – something quite challenging with existing methods such as patch-clamp and microinjection²⁵⁷.

The second aim herein is to develop an appropriate BES for use in biology, as proof of concept systems with 3D printed Ag BPEs are not translatable to *in vivo* applications. Four NPs were evaluated for their use as BPEs. With PPy and Au NPs showing the most promise, due to their conductivity and low cytotoxicity, they were taken forward to assess as BPEs. Both PPy and Au NPs allowed for the reduction of Pd onto the NPs surface, as characterised using DLS and TEM. Although NPs have previously been used in BESs to create Janus particles, the results herein are important as they allow the reduction of a species at the NP surface at a low potential (20 V/cm). This shows promise that BESs may be compatible with biological systems.

Although bipolar electrochemistry was successful at the NP BPEs, the deposition presented very differently to the MWs grown in Chapter 2. This was to be expected as NP BPEs were in suspension during electrical stimulation. This meant that their orientation was continuously changing and hence the anode and cathode on each NP continuously varied, as well as the NPs position in comparison to other NPs. This meant that material was deposited on different areas of the NP BPEs and ultimately created a coating of material rather than material from BPE to BPE. In order to further study whether NP BPEs could be used to grow MWs, it is necessary to assess them when supported in a fixed position, as they would be somewhat supported when in tissue. It is hypothesised that when supported the NPs would behave similarly to 3D printed micro-BPEs and allow for the growth of MWs between them.

NPs were chosen for use as BPEs for their biocompatibility and ability to be injected into a target site. As was discussed, another benefit is that they also allow for fine-tuning of properties or site-specific targeting through functionalisation of the NPs. Hence, further investigations using functionalised NPs would be interesting. This could allow for wires to be grown from specific cells, or for NP BPEs to be visualised *in vivo* using fluorescent tagging.

Working towards growing conductive structures at tumour sites for use with TTFs, NP BPEs were then incorporated in a TTF research device. This will determine whether the hypothesis is accepted, that conductive structures

would enhance TTFs. Initial studies suggest that NP BPEs are improving the cytotoxic effects of TTFs, although further studies are necessary to confirm this hypothesis.

The final experimental chapter herein is aimed at improving the understanding of BESs at the nanoscale, specifically those in the presence of biology. Utilising EIS, a novel method is described, allowing for nano-BPEs to be analysed for the first time in a simple label-free method. It is shown that Au NP BPEs can be sensed when in a high impedance electrolyte (dH_2O) but are masked when suspended in a low impedance electrolyte (PBS). This highlights design constraints for BESs, and the need for tailored bypass impedances to probe the BPEs.

Following proof of the method to probe nano-BPEs without cells, Au NPs are then incorporated intracellularly to test the method with biological systems. Circuit fittings show that NP BPEs can be addressed using this method, adding a capacitance to the system. This suggests Au NP BPEs can report changes in electronic properties, which could be exploited to develop novel sensing paradigms. As mentioned above, NP BPEs are beneficial as they allow for ease of functionalisation and therefore precise properties. Pairing uniquely designed NP BPEs with this method could provide a novel sensing method to aid in the understanding of intracellular bioelectricity. By binding NPs to specific cell sites, changes in electronic properties may then be sensed using

EIS. Similarly, these NP BPEs could be optimised for actuation purposes, allowing the precise electrical stimulation of intracellular components.

Herein this EIS method is used to probe BPEs that are not partaking in electrochemical reactions. The next step would be to perform this method during the reduction and oxidation of species. This method could also likely provide a way of confirming that bipolar electrochemistry has taken place, i.e., confirm the presence of wire growth (Chapter 2) or metal deposition (Chapter 3); this is discussed further in sections 5.2.1.3 and 5.2.4.

The combination of bipolar electrochemistry and biology, as discussed within this thesis, is an exciting and novel area of research that has been scarcely explored. Many of the results presented show promise that it is possible to perform bipolar electrochemistry with biology, without using high potentials and causing cytotoxicity. Although there is still a large amount of work necessary before a bipolar electrochemistry-based technique is translated to a clinical application, strong evidence is provided herein to show that this may be possible. A multi-disciplinary approach is needed, as well as a further understanding of bipolar electrochemistry at the nanoscale. As it is widely accepted that high potentials are required when using nano-BPES, a greater amount of evidence is likely needed to convince electrochemists otherwise. Providing this evidence to raise questions, will then allow for the greatest minds in the field to form a new understanding of how bipolar

electrochemistry at the nanoscale behaves differently to the macroscale. In turn, this will allow for novel applications, such as the wireless growth on *in vivo* bioelectronics, to be established.

Novel applications of bipolar electrochemistry are a hot topic, with multiple high impact reviews being recently published^{105,117}. Despite the field being very accessible, many in the research community are still not aware of bipolar electrochemistry, with the phenomenon lacking a descriptive mention in the very publications detailing its performance. A number of published high impact applications with biology, such as the growth of conductive structures to enhance TTFs as detailed herein, is what is required to highlight the exciting possibilities which nano bipolar electrochemistry can bring to diverse research fields. Further development of these novel wireless methods will have great impacts in bioelectronic medicine and may bring us closer to the reality of truly harnessing electricity for therapeutic benefit.

As stated within the introduction, what if electricity could be used to coax insulin from cells to treat diabetes, regulate food intake to treat obesity, correct balances in smooth-muscle tone to treat hypertension and pulmonary diseases⁵, or target tumour cells and program their cell death? By wirelessly sensing and actuating electrodes of an equivalent scale to cellular components, the addition of nano-bipolar electrochemistry-based techniques to bioelectronic medicine may have the power to do all of this. It is therefore

hoped that the initial studies herein, combining bipolar electrochemistry with biological systems, will inspire others to question what bipolar electrochemistry could bring to their field in order to improve the prospects of bioelectronic medicine.

5.2. Future work

As discussed, the optimisation of bipolar electrochemistry for use with biology could bring innovative applications in bioelectronic medicine. Whilst the aims set out above have been achieved, there is still a vast amount of work required to reach the end goal of translating bipolar electrochemical nano-systems into clinical use. This section outlines such work including specific avenues of research that were pursued and unable to be completed due to the Covid-19 pandemic, as well as longer term studies required.

5.2.1. *In Vivo* Wire growth proof of concept

The ability to grow conductive structures *in vivo* could have great applications in bioelectronic medicine. Although Ag MWs have been grown in the presence of biology before, this was only in 2D cultures and only includes one study¹¹². As shown in Chapter 2, Ag MWs can also be wirelessly grown in the presence of 3D cell cultures. This shows promise for developing an *in vivo* proof of concept for growing Ag MWs within a tissue. To reach this goal, several avenues of research must be pursued. This includes optimising wire growth in 3D environments, optimising wire growth in the presence of biology by using alternating current and developing a method capable of monitoring the success of *in vivo* wire growth. Although these further aims could not be reached due to the Covid-19 pandemic, a number of initial studies were performed to reach these aims as discussed below.

5.2.1.1. 3D wire growth

The first step towards growing MWs in tissues, is to optimise the control of MWs in a 3D space. Similar to a previous study investigating Ag MW growth in 2D settings¹¹², investigation of how systems behave in 3D is needed. This will include investigating how MW growth behaves in 3D without cells, before then further investigating the growth of MWs in the presence of 3D cell cultures, as per the proof-of-concept shown in Chapter 2. Further analysis of varying BPE and FE geometries in 3D systems and their effect on Ag MW resistance and \varnothing would also be beneficial, to compare 3D and 2D¹¹² grown Ag MWs.

Initial studies were performed whereby large numbers of layers of an insulator (TPGDA) were printed below conductive BPEs (AgNP ink), to create varying height BPEs (Figure 5-1). This created 3D structures that could be used to assess whether wire growth could be directed in multiple directions and multiple planes. As seen in Figure 5-2, wire growth was possible using standard DC methods at 90 V (~ 130 V/cm). Ag MWs grew between varying height BPEs, suggesting that wire growth would be possible in 3D spaces. More complex setups are required to confirm this.

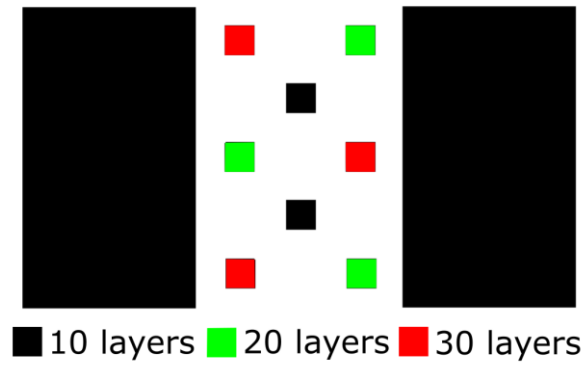


Figure 5-1 Pattern for inkjet printing of 3D structures showing varying height BPEs, produced by printing 10, 20 or 30 layers of TPGDA, followed by three layers of Ag.

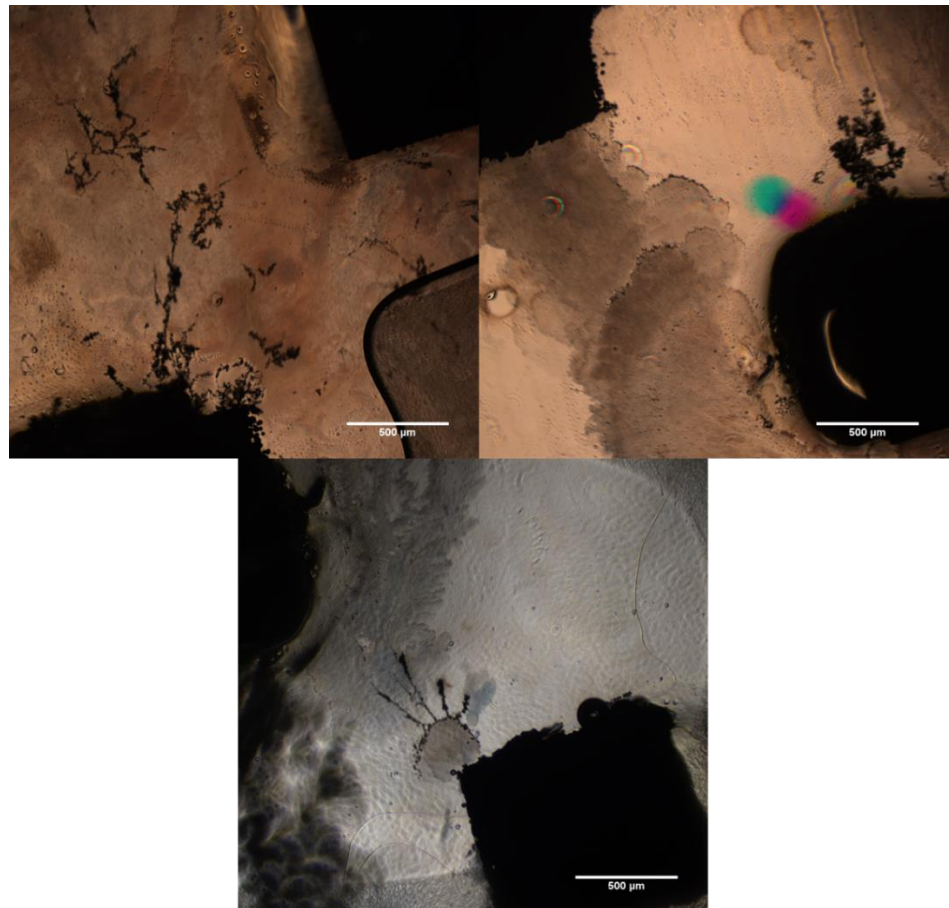


Figure 5-2 Ag MW growth using 3D structures.

Electrochemistry can be used to wirelessly grow MWs in a variety of materials, as reported in the literature^{109,111,176,258}; however, these examples are all in 2D settings. Hence, optimising MW growth in a 3D setting would not just aid in merging in-situ grown MWs with biology, but may also impact other areas, such as manufacturing micro-scale integrated electronics.

5.2.1.2. AC Wire Growth

As discussed in Chapter 2, growing MWs with alternating current, rather than direct current, could allow for improved merging with biology. Not only do high frequencies allow for the cell membrane to be bypassed⁶⁶, but the introduction of frequency could allow for lower potentials to be applied to promote higher cell viability. As shown in Chapter 2, it is possible to grow Ag MWs using bipolar electrochemistry under the application of AC electrical stimulation. Other examples exist using AC such as with Pd and PPy¹⁷⁶. However, no examples of merging AC grown MWs with biological systems exist. Enabling this could have great impacts in the area of bioelectronic medicine⁵ and biosensing¹³⁴, allowing the in-situ growth of devices and sensors to innovatively treat and diagnose diseases.

Initial studies were carried out involving 2D monolayers of U251 glioblastoma cells. Experiments carried out without cells were repeated with cells cultured over the FEs and BPEs. The electrical inputs used in section 2.3.5 were repeated with samples with cells (10, 50 and 100 V, at 1, 10, 100, 1k, 10k,

100k Hz, and 10 and 50 V at 1M Hz). As seen in Figure 5-3:C and D, wire growth was possible at the extremities of these inputs, using 50 V and 1 MHz. It is likely wires did not grow at lower inputs due to the impedance being too high when cells are present. To overcome this impedance, higher frequencies are required, outside of the capabilities of the equipment available during the Covid-19 pandemic.

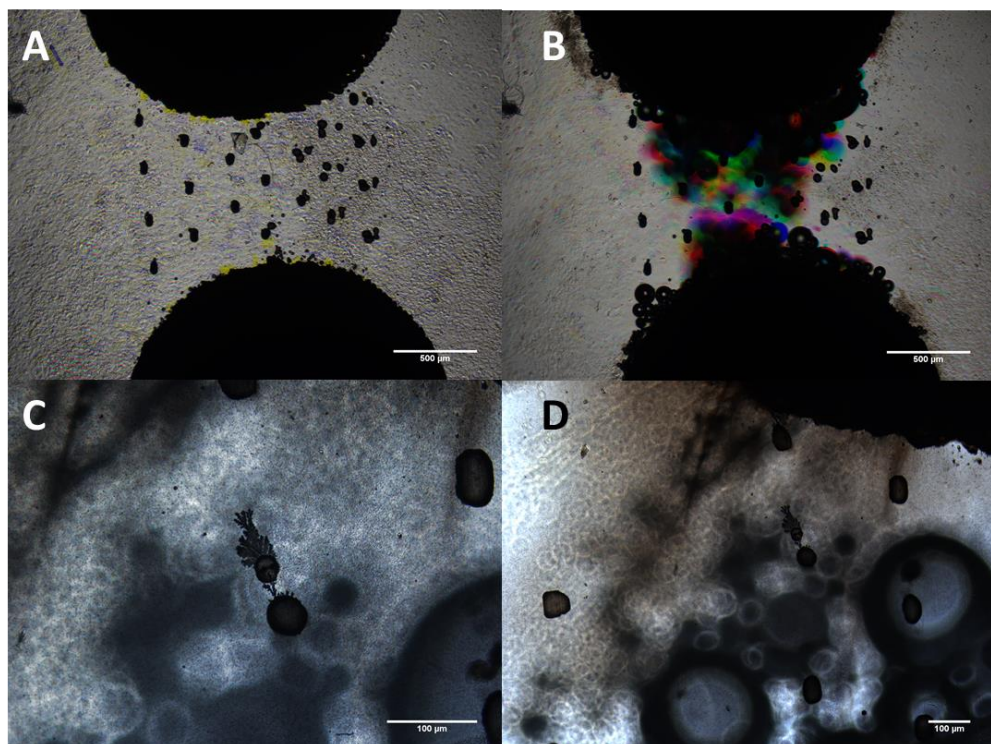


Figure 5-3 Attempted AC wire growth with cells, images showing BES before (A), during (B) and after (C and D) electrical stimulation.

As seen in Figure 5-3:A and B, the application of AC stimulation to monolayers causes the cells to detach from the surface. Therefore, it would also be beneficial, and more representative of *in vivo* behaviour, to repeat experiments in a 3D model, or within a tissue *ex vivo*. AC wire growth was

attempted with 3D spheroids; however, wire growth was unsuccessful. It is possible that utilising higher frequencies could allow for the success of wire growth in the presence of 3D spheroids in order to bypass the increased impedance when spheroids are present. Alternative equipment with higher frequency capabilities could not be sourced due to the Covid-19 pandemic. Further studies would include performing these experiments and optimising electrical inputs for MW growth in and around 3D spheroids. Following on from the success of this, wire growth in tissue *ex vivo* and then animal models should be pursued. This will then allow for studies growing bioelectronics at tumour sites, followed by the application of TTFs to determine if conductive structures enhance their effects (discussed further in section 5.2.3).

As discussed in Chapter 3, 3D printed BPEs on a substrate are not suitable for use to grow *in vivo* bioelectronics as they only provide a 2D structure. Due to this, NP BPEs have been developed herein. Hence a logical next step is to pursue a proof of concept of growing MWs with NP BPEs. This would initially include 2D monolayer structures with NP BPEs attached to a surface, prior to moving to 3D models with NPs injected along with the MW monomer/metal salt.

Furthermore, moving to conductive biomaterials that are more flexible and which therefore better mimic biology is crucial. Electrochemical growth of conductive polymers is possible without the presence of cells^{111,258}, hence

growing conductive structures using conductive polymers *in vivo* may be feasible. Further experiments could include developing *in vivo* proof of concepts using alternative biomaterials such as PEDOT or the one discussed here-in: Polypyrrole.

5.2.1.3. Impedance Analysis of Wire Growth

A final step towards being able to grow MWs *in vivo* is developing a method of non-invasively determining whether wire growth has taken place. As shown in Chapter 2, visualising wire growth with 3D cell cultures is a challenge, and this may become even more difficult when using *ex vivo* tissue samples (e.g. organotypic slice) and animal models. Due to this, a method that allows for the wireless monitoring of wire growth would be extremely beneficial.

As discussed in Chapter 4, EIS is a useful tool for probing nano-BPEs and hence, could provide a useful tool for this application. Initial studies were performed without the presence of cells, measuring BES impedance before and after wire growth. A potentiostat was attached using two electrodes attached to two BPEs, as seen in Figure 5-4. EIS was performed in galvanostatic mode during MW growth, providing bode plots as shown in Figure 5-4. Due to Covid-19 equipment was not available to simultaneously visualise the MW growth; hence, it was difficult to correlate measurements to MW growth behaviour. Thus, EIS was instead used to measure the impedance of the entire BES before and after MW growth. As seen in Figure 5-5, MW growth consistently reduced

the impedance of the BES. This shows that the method is capable of highlighting when MW growth has taken place, which could also be translatable to BESs with biology present.

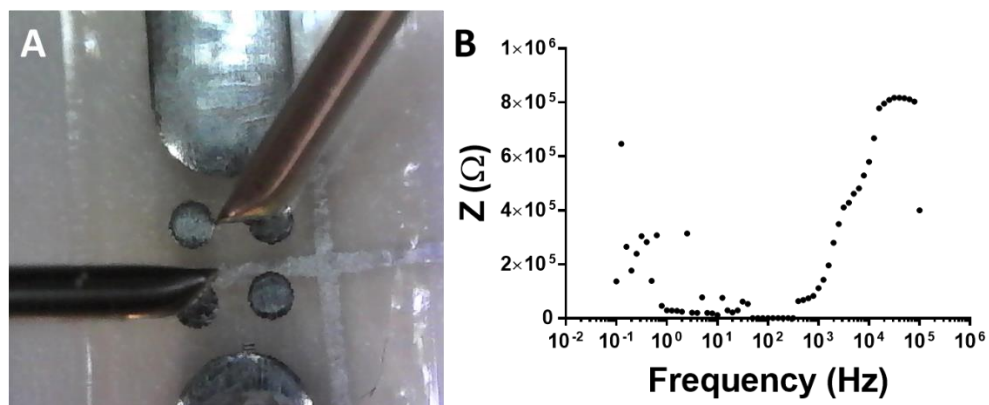


Figure 5-4 Impedance measurements during wire growth, set up (A) and example bode plot in galvanostatic mode (B).

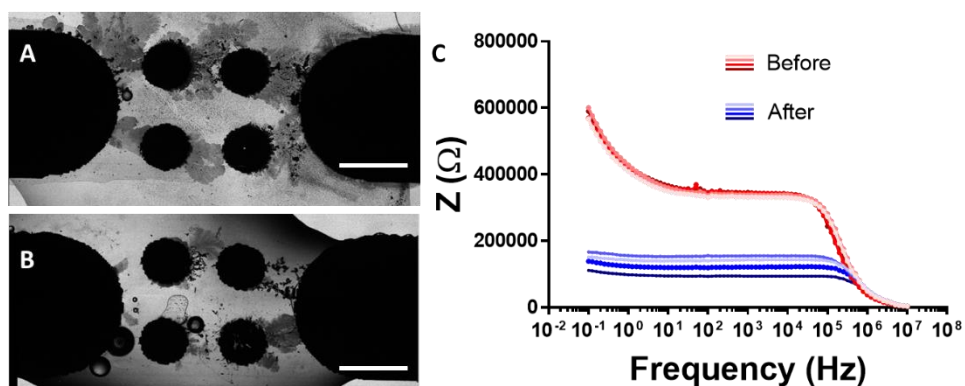


Figure 5-5 Impedance measurements before and after wire growth (C). Example wire growth samples can be seen in A and B, scale bars show 100 μm .

5.2.2. *In Vivo* bipolar electrochemistry proof of concept

As discussed in section 1.2.3, bipolar electrochemistry has few biomedical applications due to the high potentials thought to be needed to drive reactions

at the nanoscale, which would not be biocompatible. Results from Chapter 3 suggest that bipolar electrochemistry can be performed at the surface of NPs using lower potentials than those predicted (20 V/cm). This suggests that bipolar electrochemistry may be possible within biological systems, and hence *in vivo* testing would be extremely interesting. As a proof of concept study, *Caenorhabditis elegans* (*C. elegans*) were chosen to provide the first *in vivo* example of bipolar electrochemistry. *C. elegans* are a convenient animal model due to their small size, short life span, large progeny production, and a completely sequenced and well-annotated genome²⁵⁹. They also do not require approval by the institutional animal care and use committees, therefore being a more feasible animal model in the time frame of this thesis.

As seen in Figure 5-6, the *in vivo* proof of concept consisted of internalising PdCl₂ and Au NP BPEs in *C. elegans*, before applying an external electric field to reduce the Pd onto the Au NP surface. Similar to experiments in section 3.3.3, samples would then be evaluated with TEM and EDS to determine whether a redox reaction has taken place.



Figure 5-6 Schematic of bipolar electrochemical deposition of a metal onto the surface of NPs, whilst incorporated in *C. elegans*.

C. elegans (Minnesota University, Caenorhabditis Genetics Center) were cultured using standard methods, on *E. coli* coated agar plates, as described in the wormbook²⁶⁰. *C. elegans* at stage L2 were used for all experiments. NPs and PdCl₂ were added to plates when *C. elegans* had reached this growth stage. NPs and metal salt were incorporated inside *C. elegans* by adding salt/NP solutions to plates containing nematodes and waiting 24 hours to allow ingestion to take place. As seen in Figure 5-6, nematodes were then placed between FEs and electrically stimulated to allow for metal salt redox reactions to take place. Nematodes were then immediately sacrificed for imaging.

C. elegans were imaged using TEM (FEI Tecnai G2 12 Biotwin). Sample preparation consisted of fixing samples in 4% paraformaldehyde for 1 hour, fixing in glutaraldehyde for 24 hours, suspending fixed samples into an agar droplet and embedding the agar droplet into resin. A standard tissue resin embedding protocol was used. A number of samples were sectioned and imaged as test samples, to determine whether the sample preparation was adequate. These produced high-resolution images that allow for the visualisation of NP agglomerates if present (Figure 5-7). Samples with Au NPs and PPy NPs, with and without PdCl₂, with and without electrical stimulation were also prepared; however, these were not able to be imaged before the Covid-19 pandemic.

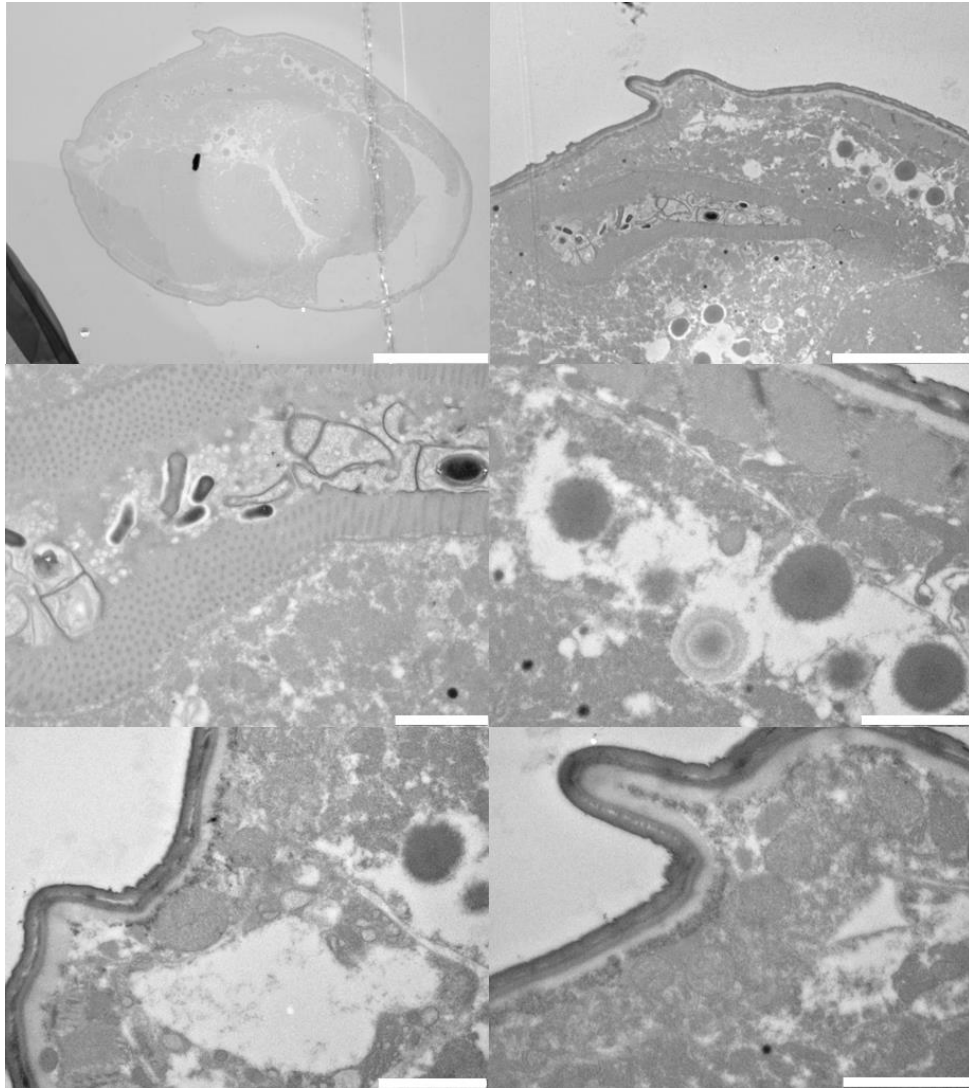


Figure 5-7 TEM images of *C. elegans* cross-sections. Scale bars represent 2 μm .

The above test samples were coated for imaging, and therefore could not be assessed using EDS. Experimental samples were going to be imaged and analysed using EDS to provide elemental maps to determine whether Pd deposition had taken place. Test samples were imaged by a technician and hence areas were selected at random. For experimental samples, imaging would be focused on the intestine, as this is likely where the NPs would be due

to them being introduced to the *C. elegans* as food. As seen in Figure 5-8, the intestine of a *C. elegans* spans its entire body, therefore making a small number of NPs difficult to find. Further optimisation of sample preparation will be required in order to gather cross-sections of the entire nematode to be imaged, to allow for a maximum chance of visualising NPs.

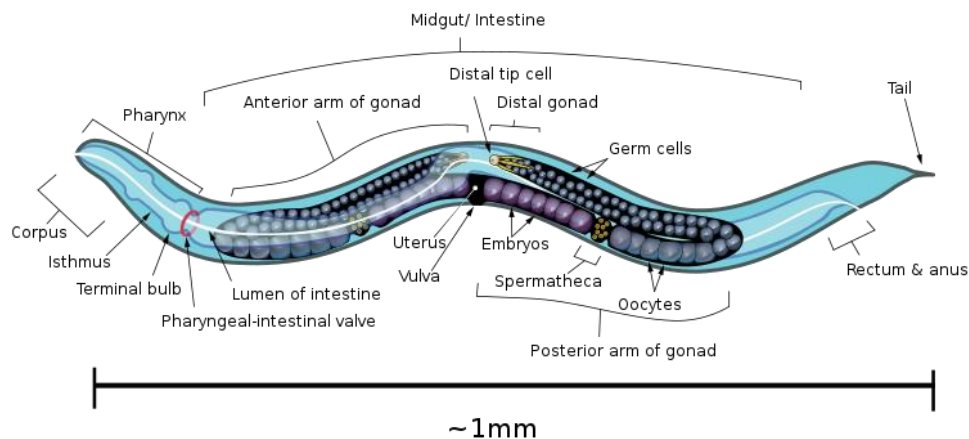


Figure 5-8 Anatomy of an adult *C. elegans* Image created by K.D. Schroeder.

An alternative method to allow for more precise location of NPs for evaluation was attempted, involving micro-injection of fluorescent NP solutions into individual nematodes. However, equipment at the University of Nottingham proved to be unsuitable for this, and the Covid-19 pandemic did not allow for alternative equipment to be sourced. Additionally, as seen in Figure 5-9:B, *C. elegans* possesses autofluorescence which interferes with the use of fluorescent NPs. Another alternative method that was pursued was dissolving the worm after the reaction had taken place, so that NPs could then be analysed using simpler methods, not requiring tissue embedding. However,

these too were unable to be completed in the time-frame due to the Covid-19 pandemic.

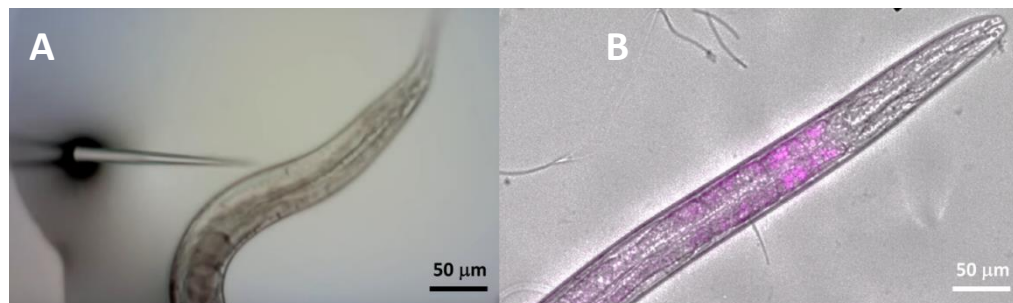


Figure 5-9 Micro-injection of *C. elegans* (A) and fluorescent image of *C. elegans* with fluorescent nanoparticles (B).

5.2.2.1. *In Vitro* bipolar electrochemistry

Due to complications with method optimisation using whole organisms, another avenue of future work would be providing an *in vitro* proof of concept of bipolar electrochemistry with biology. Although this has been witnessed once before¹³³, many within the bipolar electrochemistry community still believe that BPEs cannot be successfully combined with biology. Hence this would be an important addition to the literature. Similar to whole organism studies, PdCl₂ and NP BPEs would be incubated with cells, before applying an external electric field. The success of the reduction of Pd would then be evaluated, as well as the effect of the required electric field on the viability of the cells. To simplify visualisation within cells, an alternative redox reaction could be pursued with NPs being functionalised to provide

electrochemiluminescence upon the success of the reaction. Due to the Covid-19 pandemic, these studies could not be completed in the timeframe.

5.2.3. Electric Field Enhancement for Tumour Treating Fields (TTFs)

As outlined in section 1.1.3.1, this thesis is working towards improving the capabilities of TTFs. Despite TTFs improving brain tumour patient survival rates in comparison to chemotherapies alone^{261,262}, the therapy is only licensed in a few countries worldwide. Improving patients' outcomes further could allow for wider uptake, and hence many clinical trials exist combining TTFs with other treatment modalities, such as radiotherapy²⁶³ and pharmaceuticals²⁶⁴. Similar trials are required to determine whether conductive structures may improve TTFs; however, several pre-clinical trial studies are required first. Although initial studies, shown in Chapter 3, suggest that conductive structures will have an improved effect on the TTFs, these studies could not be fully completed due to the Covid-19 pandemic and hence further investigations are required as detailed below.

5.2.3.1. *In vitro* Studies

Initial studies, shown in Chapter 3, show that the introduction of conductive NPs improves the cytotoxic effects of TTFs. More rigorous investigations are required to confirm this *in vitro*. Additionally, studies using other cell types would be beneficial to determine whether improved TTFs could be licensed for cancers other than those of the brain. Further studies, using a more tuneable

device than the Innovitro, are required to determine whether electrical inputs can be altered to reduce costs or therapy timeframes.

Given that conductive structures continue to show promise at enhancing TTFs effects, further studies linked to those discussed above in section 3.3.4 are required. Conductive structures would be grown wirelessly around tumour models and then exposed to TTFs, followed by analysis to determine the effects of the conductive structures on the cell population.

Furthermore, there are still conflicting views around the mechanism of TTFs. Although it is widely accepted that TTFs halt cell proliferation during mitosis⁶³, it is also believed that electric fields at TTFs intensity should not bypass the cell membrane⁶⁶. If the latter is true, then TTFs would not be capable of affecting the intracellular organelles involved in cell division, as so many publications claim. A possible explanation is that cells are sensing an electric field on their surface, which is then causing downstream intracellular effects. This theory is discussed with regards to electric field effects and cell motility²⁶⁵. The theory posits that cells sense electric fields at the glycocalyx, and the force is then transferred to the cytoskeleton. Further investigations are required to determine whether this theory predicts what occurs upon the application of TTFs. This phenomenon may also be responsible for why varying cell types have shown to prefer different frequencies of TTFs: i.e., because their glycocalyx is different. Understanding the exact mechanism of TTFs may allow further

optimisation of the therapy for a wide variety of cancer types. Understanding how cells sense and behave in electric fields would also have great impact on the rest of the bioelectronic medicine field.

5.2.3.2. *In vivo Studies*

Following the success of *in vitro* studies, *in vivo* studies are required. This will initially involve no electrochemistry, rather conductive NPs alone are injected into tumour sites, combined with TTFs. Animal studies comparing TTFs with TTFs and conductive NPs will show whether introducing bioelectronics at tumour sites will improve TTFs. Next, studies to determine whether conductive structures will allow for reduced electrical inputs or therapy timeframes should be carried out. This will help to determine whether conductive structures at the tumour site are capable of improving the cost-benefit of the therapy to aid in wider uptake. In parallel, upon the success of *in vitro* studies, *in vivo* studies growing conductive structures between NP BPEs should also be performed, to determine the efficacy and safety of doing so in living organisms.

After the successful development of a method to grow conductive structures safely at tumour sites, further animal studies and clinical trials should be performed to determine whether this method enhances the survival rates of cancer patients further or improves the cost-benefit ratio. TTFs have been shown to significantly improve survival of recurrent and newly diagnosed GBM patients, over chemotherapy alone²⁶¹. Due to this, initial studies should

also be tested with GBM. Subsequent studies may be performed testing conductive structures at other tumour sites such as breast or skin.

5.2.4. Impedimetric Characterisation of Bipolar Electrochemistry

As discussed in Chapter 4, EIS is a useful tool for probing nano-BPEs. Results included here-in use EIS as a non-invasive method of probing nano-BPEs intracellularly. Hence, once the above work is carried out to develop an *in vitro* proof of concept of bipolar electrochemistry with nano-BPEs, further work may include utilising EIS to probe these BPEs. The application of EIS to BESs with cells, before and after electrical stimulation, could be used as a method to non-invasively sense whether a reaction has taken place. This could be very useful for quality control to easily determine the success of redox reactions at intracellular BPEs.

5.2.5. Understanding Nano-Bipolar Electrochemistry

Finally, one of the most crucial findings in this body of work is the behaviour of nano-BPEs at low voltages. As discussed, theory suggests that high voltages, in the kV region, are required to drive redox reactions at nano-BPEs¹⁰⁷. Multiple results within this thesis, suggest this to not be the case. Studies exist that evaluate the behaviour of nano-electrodes in comparison to macro-electrodes. One important study, by Compton et al²¹², involves analysing solutions of the Poisson-Boltzmann equation in a spherical space. They conclude that the diffuse double layer at a nano-electrode differs from predictions made by

classical Guoy-Chapman theory. These effects are due to the electrode radius becoming large compared to the Debye length. They predict that this would cause increased charging current and electrochemical driving forces. This could also be a factor contributing to the behaviour of nano-BPEs.

Further investigations are required, involving the experimental analysis and mathematical modelling to determine whether this enhanced double layer may also be present in nano-BPEs. This greater understanding will improve prospects of merging bipolar electrochemistry with biology, as well as enabling novel sensing applications.

References

1. Rabaey, K. & Verstraete, W. Microbial fuel cells: Novel biotechnology for energy generation. *Trends Biotechnol.* **23**, 291–298 (2005).
2. Mehrotra, P. Biosensors and their applications - A review. *J. Oral Biol. Craniofacial Res.* **6**, 153–159 (2016).
3. Ong, J. M. & da Cruz, L. The bionic eye: A review. *Clin. Exp. Ophthalmol.* **40**, 6–17 (2012).
4. Soboyejo, W. O. *et al.* 3D Printed Bionic Ears. *Nano Lett.* **13**, 2634–2639 (2013).
5. Famm, K., Litt, B., Tracey, K. J., Boyden, E. S. & Slaoui, M. A jump-start for electroceuticals. *Nature* **496**, 159–161 (2013).
6. Kalinowsky, L. B. History of Convulsive Therapy. *Ann. N. Y. Acad. Sci.* **462**, 1–4 (1986).
7. Fink, M. Meduna and the origins of convulsive therapy. *Am. J. Psychiatry* **141**, 1034–1041 (1984).
8. van Hemel, N, M. & van der Wall, E, E. 8 October 1958, D Day for the implantable pacemaker. *Netherlands Hear. J.* **16**, 3–4 (2008).
9. Lozano, A. M., Dostrovsky, J., Chen, R. & Ashby, P. Deep brain stimulation for Parkinson's disease: Disrupting the disruption. *Lancet Neurology* **1**, 225–231 (2002).
10. Pereira, E. A., Green, A. L., Nandi, D. & Aziz, T. Z. Deep brain stimulation: Indications and evidence. in *Expert Review of Medical Devices* **4**, 591–603 (2007).
11. Farrand, S. *et al.* Deep brain stimulation for severe treatment-resistant obsessive-compulsive disorder: An open-label case series. *Aust. N. Z. J. Psychiatry* **52**, 699–708 (2018).
12. Dandekar, M. P., Fenoy, A. J., Carvalho, A. F., Soares, J. C. & Quevedo, J. Deep brain stimulation for treatment-resistant depression: An integrative review of preclinical and clinical findings and translational implications. *Mol. Psychiatry* **23**, 1094–1112 (2018).

13. Slopsema, J. P. & Johnson, M. D. Deep brain stimulation. in *Neuroprosthetics: Theory and Practice: Second Edition* 762–789 (2017). doi:10.1142/9789813207158_0023
14. Hariz, M., Blomstedt, P. & Zrinzo, L. Future of brain stimulation: New targets, new indications, new technology. *Mov. Disord.* **28**, 1784–1792 (2013).
15. Zeng, F. G. Trends in Cochlear Implants. *Trends Amplif.* **8**, 1–34 (2004).
16. Cohen, N. L. & Hoffman, R. A. Complications of cochlear implant surgery in children. in *Annals of Otolaryngology, Rhinology & Laryngology* **100**, 708–711 (1991).
17. Farinetti, A. *et al.* Cochlear implant complications in 403 patients: Comparative study of adults and children and review of the literature. *Eur. Ann. Otorhinolaryngol. Head Neck Dis.* **131**, 177–182 (2014).
18. Chuang, A. T., Margo, C. E. & Greenberg, P. B. Retinal implants: A systematic review. *Br. J. Ophthalmol.* **0**, 1–5 (2014).
19. Son, M. & Park, T. H. The bioelectronic nose and tongue using olfactory and taste receptors: Analytical tools for food quality and safety assessment. *Biotechnol. Adv.* **36**, 371–379 (2018).
20. Wasilewski, T., Gębicki, J. & Kamysz, W. Bioelectronic nose: Current status and perspectives. *Biosens. Bioelectron.* **87**, 480–494 (2017).
21. Oh, E. H., Song, H. S. & Park, T. H. Recent advances in electronic and bioelectronic noses and their biomedical applications. *Enzyme Microb. Technol.* **48**, 427–437 (2011).
22. Schaller, R. R. Moore’s Law: past , present , future. *IEEE Spectr.* **34**, 52–59 (1997).
23. Shaw, J., McConnell, T. H. & Hull., K. L. Communication: Chemical and Electrical Signaling. in *Human Form, Human Function: Essential of Anatomy & Physiology* 110–137 (2011).
24. Harding, J. L. & Reynolds, M. M. Combating medical device fouling. *Trends Biotechnol.* **32**, 140–146 (2014).
25. Lewis, J. A. & Ahn, B. Y. Device fabrication: Three-dimensional printed electronics. *Nature* **518**, 42–43 (2015).
26. Levin, M., Selberg, J. & Rolandi, M. Endogenous Bioelectrics in

- Development, Cancer, and Regeneration: Drugs and Bioelectronic Devices as Electroceuticals for Regenerative Medicine. *iScience* **22**, 519–533 (2019).
27. Liu, J. *et al.* Multifunctional three-dimensional macroporous nanoelectronic networks for smart materials. *Proc. Natl. Acad. Sci. U. S. A.* **110**, 6694–6699 (2013).
 28. Zavanelli, N., Kim, J. & Yeo, W. Recent Advances in High-Throughput Nanomaterial Manufacturing for Hybrid Flexible Bioelectronics. *Materials (Basel)*. **14**, 1–35 (2021).
 29. Bandodkar, A. J. *et al.* Tattoo-based noninvasive glucose monitoring: A proof-of-concept study. *Anal. Chem.* **87**, 394–398 (2015).
 30. Mannoor, M. S. *et al.* Graphene-based wireless bacteria detection on tooth enamel. *Nat. Commun.* **3**, 1–8 (2012).
 31. Kim, J. *et al.* Wearable temporary tattoo sensor for real-time trace metal monitoring in human sweat. *Electrochem. commun.* **51**, 41–45 (2015).
 32. Mineev, I. R. *et al.* Electronic dura mater for long-term multimodal neural interfaces. *Science (80-.)*. **347**, 159–163 (2015).
 33. Choi, H. K., Lee, J. H., Lee, T., Lee, S. N. & Choi, J. W. Flexible Electronics for Monitoring in vivo Electrophysiology and Metabolite Signals. *Front. Chem.* **8**, (2020).
 34. Li, S., Sun, Y. & Gao, D. Role of the nervous system in cancer metastasis. *Oncology Lett.* **5**, 1101–1111 (2013).
 35. Venkatesh, H. & Monje, M. Neuronal Activity in Ontogeny and Oncology. *Trends Cancer* **3**, 89–112 (2017).
 36. Lang, F. & Stournaras, C. Ion channels in cancer: future perspectives and clinical potential. *Philos. Trans. R. Soc. B Biol. Sci.* **369**, 20130108 (2014).
 37. Prevarskaya, N., Skryma, R. & Shuba, Y. Ion channels and the hallmarks of cancer. *Trends Mol. Med.* **16**, 107–121 (2010).
 38. Ko, J.-H. *et al.* Expression profiling of ion channel genes predicts clinical outcome in breast cancer. *Mol. Cancer* **12**, (2013).
 39. Fraser, S. P. *et al.* Voltage-gated sodium channel expression and potentiation of human breast cancer metastasis. *Clin. Cancer Res.* **11**, 5381–5389 (2005).

40. Robinson, A. J. *et al.* Toward Hijacking Bioelectricity in Cancer to Develop New Bioelectronic Medicine. *Advanced Therapeutics* **4**, (2021).
41. Payne, S. L., Levin, M. & Oudin, M. J. Bioelectric Control of Metastasis in Solid Tumors. *Bioelectricity* **1**, 114–130 (2019).
42. Turner, K. L. & Sontheimer, H. Cl⁻ and K⁺ channels and their role in primary brain tumour biology. *Philos. Trans. R. Soc. B Biol. Sci.* **369**, (2014).
43. Becchetti, A. Ion channels and transporters in cancer. 1. Ion channels and cell proliferation in cancer. *Am. J. Physiol. Physiol.* **301**, 255–265 (2011).
44. Schwab, A. & Stock, C. Ion channels and transporters in tumour cell migration and invasion. *Philos. Trans. R. Soc. B Biol. Sci.* **369**, (2014).
45. Fiorio Pla, A. & Munaron, L. Functional properties of ion channels and transporters in tumour vascularization. *Philos. Trans. R. Soc. B Biol. Sci.* **369**, (2014).
46. Djamgoz, M. B., Coombes, R. C. & Schwab, A. Ion transport and cancer: from initiation to metastasis. *Philos. Trans. R. Soc. B Biol. Sci.* **369**, (2014).
47. Byrne, J. D. *et al.* Local iontophoretic administration of cytotoxic therapies to solid tumors. *Sci. Transl. Med.* **7**, (2015).
48. Proctor, C. M. *et al.* Electrophoretic drug delivery for seizure control. *Sci. Adv.* **4**, 1–8 (2018).
49. Venkataramani, V. *et al.* Glutamatergic synaptic input to glioma cells drives brain tumour progression. *Nature* **573**, 532–538 (2019).
50. Venkatesh, H. S. *et al.* Electrical and synaptic integration of glioma into neural circuits. *Nature* **573**, 539–545 (2019).
51. Zeng, Q. *et al.* Synaptic proximity enables NMDAR signalling to promote brain metastasis. *Nature* **573**, 526–531 (2019).
52. Esmaili, N. & Friebe, M. Electrochemotherapy: A review of current status, alternative IGP approaches, and future perspectives. *J. Healthc. Eng.* **2019**, (2019).
53. Pichi, B., Pellini, R., De Virgilio, A. & Spriano, G. Electrochemotherapy: a well-accepted palliative treatment by patients with head and neck tumours. *Acta Otorhinolaryngol. Ital.* **38**, 181–187 (2018).

54. Wichtowski, M. & Murawa, D. Electrochemotherapy in the treatment of melanoma. *Contemp. Oncol.* **22**, 8–13 (2018).
55. Racioppi, M. *et al.* ElectroMotive drug administration (EMDA) of Mitomycin C as first-line salvage therapy in high risk “BCG failure” non muscle invasive bladder cancer: 3 years follow-up outcomes. *BMC Cancer* **18**, (2018).
56. Kos, B., Vásquez, J. L., Miklavčič, D., Hermann, G. G. G. & Gehl, J. Investigation of the mechanisms of action behind Electromotive Drug Administration (EMDA). *PeerJ* **4**, (2016).
57. Fabian, D. *et al.* Treatment of Glioblastoma (GBM) with the addition of Tumor-Treating Fields (TTF): A review. *Cancers (Basel)*. **11**, 1–12 (2019).
58. Levin, M. Molecular bioelectricity: how endogenous voltage potentials control cell behavior and instruct pattern regulation in vivo. *Mol. Biol. Cell* **25**, 3835–3850 (2014).
59. Sanjuan-Alberte, P., Alexander, M. R., Hague, R. J. M. & Rawson, F. J. Electrochemically stimulating developments in bioelectronic medicine. *Bioelectron. Med.* **4**, 1–7 (2018).
60. Sherman, H. G. *et al.* Mechanistic insight into heterogeneity of trans-plasma membrane electron transport in cancer cell types. *Biochim. Biophys. Acta (BBA)-Bioenergetics* **1860**, 628–639 (2019).
61. Kirson, E. D. *et al.* Disruption of cancer cell replication by alternating electric fields. *Cancer Res.* **64**, 3288–3295 (2004).
62. ClinicalTrials.gov. Feasibility Trial of Optune for Children With Recurrent or Progressive Supratentorial High-Grade Glioma and Ependymoma. (2017). Available at: <https://clinicaltrials.gov/ct2/show/study/NCT03033992>. (Accessed: 12th October 2021)
63. Gera, N. *et al.* Tumor treating fields perturb the localization of septins and cause aberrant mitotic exit. *PLoS One* **10**, (2015).
64. Giladi, M. *et al.* Mitotic Spindle Disruption by Alternating Electric Fields Leads to Improper Chromosome Segregation and Mitotic Catastrophe in Cancer Cells. *Sci. Rep.* **5**, (2015).
65. Berkelmann, L. *et al.* Tumour-treating fields (TTFields): Investigations on the mechanism of action by electromagnetic exposure of cells in

- telophase/cytokinesis. *Sci. Rep.* **9**, (2019).
66. Hart, F. X. & Palisano, J. R. The Application of Electric Fields in Biology and Medicine. in *Electric Field* 161–186 (InTech, 2018).
 67. Guzauskas, G. F., Salzberg, M. & Wang, B. C. Estimated lifetime survival benefit of tumor treating fields and temozolomide for newly diagnosed glioblastoma patients. *CNS Oncol.* **7**, CNS23 (2018).
 68. Mehta, M., Wen, P., Nishikawa, R., Reardon, D. & Peters, K. Critical review of the addition of tumor treating fields (TTFields) to the existing standard of care for newly diagnosed glioblastoma patients. *Crit. Rev. Oncol. Hematol.* **111**, 60–65 (2017).
 69. Rivera, F. *et al.* PANOVA: A pilot study of TTFields concomitant with gemcitabine for front-line therapy in patients with advanced pancreatic adenocarcinoma. *J. Clin. Oncol.* **34**, 269–269 (2016).
 70. Pless, M., Droege, C., von Moos, R., Salzberg, M. & Betticher, D. A phase I/II trial of Tumor Treating Fields (TTFields) therapy in combination with pemetrexed for advanced non-small cell lung cancer. *Lung Cancer* **81**, 445–450 (2013).
 71. Giladi, M. *et al.* Alternating electric fields (tumor-treating fields therapy) can improve chemotherapy treatment efficacy in non-small cell lung cancer both in vitro and in vivo. *Semin. Oncol.* **41**, S35–S41 (2014).
 72. Kirson, E. D. *et al.* Chemotherapeutic treatment efficacy and sensitivity are increased by adjuvant alternating electric fields (TTFields). *BMC Med. Phys.* **9**, (2009).
 73. Gebhardt, A. Basics, Definitions, and Application Levels. in *Understanding Additive Manufacturing* 1–29 (Carl Hanser Verlag GmbH & Co. KG, 2011). doi:10.3139/9783446431621.001
 74. Ligon, S. C., Liska, R., Stampfl, J., Gurr, M. & Mülhaupt, R. Polymers for 3D Printing and Customized Additive Manufacturing. *Chem. Rev.* **117**, 10212–10290 (2017).
 75. Frazier, W. E. Metal additive manufacturing: A review. *J. Mater. Eng. Perform.* **23**, 1917–1928 (2014).
 76. Chen, Z. *et al.* 3D printing of ceramics: A review. *J. Eur. Ceram. Soc.* **39**, 661–687 (2019).
 77. Chung, J. H. Y. *et al.* Bio-ink properties and printability for extrusion

- printing living cells. *Biomater. Sci.* **7**, 763–773 (2013).
78. Joshi, S. C. & Sheikh, A. A. 3D printing in aerospace and its long-term sustainability. *Virtual Phys. Prototyp.* **10**, 175–185 (2015).
 79. Savastano, M., Amendola, C., D'Ascenzo, F. & Massaroni, E. 3-D printing in the spare parts supply chain: An explorative study in the automotive industry. in *Lecture Notes in Information Systems and Organisation* **18**, 153–170 (Springer Heidelberg, 2016).
 80. Giannatsis, J. & Dedoussis, V. Additive fabrication technologies applied to medicine and health care: A review. *Int. J. Adv. Manuf. Technol.* **40**, 116–127 (2009).
 81. Shen, X., Chu, M., Hariri, F., Vedula, G. & Naguib, H. E. Binder Jetting Fabrication of Highly Flexible and Electrically Conductive Graphene/PVOH Composites. *Addit. Manuf.* **36**, 101565 (2020).
 82. Juhasz, M. *et al.* Hybrid directed energy deposition for fabricating metal structures with embedded sensors. *Addit. Manuf.* **35**, (2020).
 83. Binder, M. *et al.* Design concepts for the integration of electronic components into metal laser-based powder bed fusion parts. in *Procedia CIRP* **81**, 992–997 (Elsevier, 2019).
 84. Kong, Y. L. *et al.* 3D printed quantum dot light-emitting diodes. *Nano Lett.* **14**, 7017–7023 (2014).
 85. Glisic, B. *et al.* Strain Sensing Sheets for Structural Health Monitoring Based on Large-Area Electronics and Integrated Circuits. *Proc. IEEE* **104**, 1513–1528 (2016).
 86. Nayak, L., Mohanty, S., Nayak, S. K. & Ramadoss, A. A review on inkjet printing of nanoparticle inks for flexible electronics. *J. Mater. Chem. C* **7**, 8771–8795 (2019).
 87. Zhao, W. *et al.* Vat Photopolymerization 3D Printing of Advanced Soft Sensors and Actuators: From Architecture to Function. *Adv. Mater. Technol.* **6**, (2021).
 88. Bard, A. J. & Faulkner, L. R. *Electrochemical Methods: Fundamentals and Applications, 2nd edition. Electrochemical Methods: Fundamentals and Applications, 2nd Edition* (2008).
 89. Compton, R. G. & Banks, C. E. *Understanding voltammetry, 2nd edition. Understanding Voltammetry, 2nd Edition* (2010). doi:10.1142/P726

90. Fosdick, S. E., Knust, K. N., Scida, K. & Crooks, R. M. Bipolar electrochemistry. *Angew. Chemie - Int. Ed.* **52**, 10438–10456 (2013).
91. Duval, J., Kleijn, J. M. & Van Leeuwen, H. P. Bipolar electrode behaviour of the aluminium surface in a lateral electric field. *J. Electroanal. Chem.* **505**, 1–11 (2001).
92. Mavr , F. *et al.* A theoretical and experimental framework for understanding electrogenerated chemiluminescence (ECL) emission at bipolar electrodes. *Anal. Chem.* **81**, 6218–6225 (2009).
93. Arora, A., Eijkel, J. C. T., Morf, W. E. & Manz, A. A wireless electrochemiluminescence detector applied to direct and indirect detection for electrophoresis on a microfabricated glass device. *Anal. Chem.* **73**, 3282–3288 (2001).
94. Hasheminejad, M. *et al.* Plasmonic Imaging of the Interfacial Potential Distribution on Bipolar Electrodes. *Angew. Chemie* **129**, 1651–1655 (2017).
95. Loget, G., Zigah, D., Bouffier, L., Sojic, N. & Kuhn, A. Bipolar Electrochemistry: From Materials Science to Motion and Beyond. *Acc. Chem. Res.* **46**, 2513–2523 (2013).
96. Koefoed, L., Pedersen, S. U. & Daasbjerg, K. Bipolar Electrochemistry - A wireless approach for electrode reactions. *Curr. Opin. Electrochem.* **2**, 13–17 (2017).
97. Karimian, N., Hashemi, P., Afkhami, A. & Bagheri, H. The principles of bipolar electrochemistry and its electroanalysis applications. *Curr. Opin. Electrochem.* **17**, 30–37 (2019).
98. Backhurst, J. R., Coulson, J. M., Goodridge, F., Plimley, R. E. & Fleischmann, M. A Preliminary Investigation of Fluidized Bed Electrodes. *J. Electrochem. Soc.* **116**, 1600–1607 (1969).
99. Ellis, K. G. & Jansson, R. E. W. W. Further studies on the epoxidation of propylene in a bipolar trickle bed. *J. Appl. Electrochem.* **11**, 531–535 (1981).
100. Manji, A. & Oloman, C. W. Electrosynthesis of propylene oxide in a bipolar trickle-bed reactor. *J. Appl. Electrochem.* **17**, 532–544 (1987).
101. Lee, J. K., Shemilt, L. W. & Chun, H. S. Studies of bipolarity in fluidized bed electrodes. *J. Appl. Electrochem.* **19**, 877–881 (1989).

102. Smotkin, E. *et al.* Bipolar TiO₂/Pt semiconductor photoelectrodes and multielectrode arrays for unassisted photolytic water splitting. *J. Phys. Chem.* **90**, 4604–4607 (1986).
103. Cervera-March, S. *et al.* Modeling of Bipolar Semiconductor Photoelectrode Arrays for Electrolytic Processes. *J. Electrochem. Soc.* **135**, 567–573 (1988).
104. Wiesener, K., Ohms, D., Benczúr-Ürmössy, G., Berthold, M. & Haschka, F. High power metal hydride bipolar battery. *J. Power Sources* **84**, 248–258 (1999).
105. Bouffier, L., Zigah, D., Sojic, N. & Kuhn, A. Bipolar (Bio)electroanalysis. *Annu. Rev. Anal. Chem.* **14**, 65–86 (2021).
106. Loget, G. & Kuhn, A. Bipolar electrochemistry in the nanosciences. *Electrochemistry* **11**, 71–103 (2013).
107. Loget, G. & Kuhn, A. Shaping and exploring the micro- and nanoworld using bipolar electrochemistry. *Anal. Bioanal. Chem.* **400**, 1691–1704 (2011).
108. Loget, G., Roche, J. J. & Kuhn, A. True bulk synthesis of Janus objects by bipolar electrochemistry. *Adv. Mater.* **24**, 5111–5116 (2012).
109. Bradley, J. C., Crawford, J., Ernazarova, K., McGee, M. & Stephen, S. G. Wire Formation on Circuit Boards Using Spatially Coupled Bipolar Electrochemistry. *Adv. Mater.* **9**, 1168–1171 (1997).
110. Bradley, J. C., Crawford, J., McGee, M. & Stephens, S. G. A contactless method for the directed formation of submicrometer copper wires. *J. Electrochem. Soc.* **145**, 45–47 (1998).
111. Koizumi, Y. *et al.* Electropolymerization on wireless electrodes towards conducting polymer microfibre networks. *Nat. Commun.* **7**, (2016).
112. Sanjuan-Alberte, P. *et al.* Remotely Controlled in Situ Growth of Silver Microwires Forming Bioelectronic Interfaces. *ACS Appl. Mater. Interfaces* **11**, 8928–8936 (2019).
113. Bouchet, A. *et al.* Contactless electrofunctionalization of a single pore. *Small* **5**, 2297–2303 (2009).
114. Li, M. & Anand, R. K. High-Throughput Selective Capture of Single Circulating Tumor Cells by Dielectrophoresis at a Wireless Electrode Array. *J. Am. Chem. Soc.* **139**, 8950–8959 (2017).

115. Wang, Y. *et al.* Bipolar electrochemical mechanism for the propulsion of catalytic nanomotors in hydrogen peroxide solutions. *Langmuir* **22**, 10451–10456 (2006).
116. Loget, G. & Kuhn, A. Propulsion of microobjects by dynamic bipolar self-regeneration. *J. Am. Chem. Soc.* **132**, 15918–15919 (2010).
117. Rahn, K. L. & Anand, R. K. Recent Advancements in Bipolar Electrochemical Methods of Analysis. *Analytical Chemistry* **93**, 103–123 (2021).
118. Zhai, Q., Zhang, X., Xia, Y., Li, J. & Wang, E. Electrochromic sensing platform based on steric hindrance effects for CEA detection. *Analyst* **141**, 3985–3988 (2016).
119. Zhang, X., Lazenby, R. A., Wu, Y. & White, R. J. Electrochromic, Closed-Bipolar Electrodes Employing Aptamer-Based Recognition for Direct Colorimetric Sensing Visualization. *Anal. Chem.* **91**, 11467–11473 (2019).
120. Ying, Y. L. *et al.* Asymmetric Nanopore Electrode-Based Amplification for Electron Transfer Imaging in Live Cells. *J. Am. Chem. Soc.* **140**, 5385–5392 (2018).
121. Anand, R. K., Johnson, E. S. & Chiu, D. T. Negative dielectrophoretic capture and repulsion of single cells at a bipolar electrode: The impact of faradaic ion enrichment and depletion. *J. Am. Chem. Soc.* **137**, 776–783 (2015).
122. Wu, Y., Ren, Y., Tao, Y., Hou, L. & Jiang, H. High-Throughput Separation, Trapping, and Manipulation of Single Cells and Particles by Combined Dielectrophoresis at a Bipolar Electrode Array. *Anal. Chem.* **90**, 11461–11469 (2018).
123. Li, M. & Anand, R. K. Integration of marker-free selection of single cells at a wireless electrode array with parallel fluidic isolation and electrical lysis. *Chem. Sci.* **10**, 1506–1513 (2019).
124. De Poulpiquet, A. *et al.* Dual Enzymatic Detection by Bulk Electrogenerated Chemiluminescence. *Anal. Chem.* **88**, 6585–6592 (2016).
125. Xiao, Y., Xu, L. & Qi, L. W. Electrochemiluminescence bipolar electrode array for the multiplexed detection of glucose, lactate and choline based on a versatile enzymatic approach. *Talanta* **165**, 577–583 (2017).

126. Xu, W., Fu, K. & Bohn, P. W. Electrochromic sensor for multiplex detection of metabolites enabled by closed bipolar electrode coupling. *ACS Sensors* **2**, 1020–1026 (2017).
127. Chow, K. F., Mavr e, F. & Crooks, R. M. Wireless electrochemical DNA microarray sensor. *J. Am. Chem. Soc.* **130**, 7544–7545 (2008).
128. Shi, H. W. *et al.* Joint enhancement strategy applied in ECL biosensor based on closed bipolar electrodes for the detection of PSA. *Talanta* **154**, 169–174 (2016).
129. Shi, H. W. *et al.* Temporal Sensing Platform Based on Bipolar Electrode for the Ultrasensitive Detection of Cancer Cells. *Anal. Chem.* **88**, 8795–8801 (2016).
130. Bouffier, L., Arbault, S., Kuhn, A. & Sojic, N. Generation of electrochemiluminescence at bipolar electrodes: concepts and applications. *Anal. Bioanal. Chem.* **408**, 7003–7011 (2016).
131. Mavr e, F. *et al.* Bipolar electrodes: A useful tool for concentration, separation, and detection of analytes in microelectrochemical systems. *Anal. Chem.* **82**, 8766–8774 (2010).
132. Wang, Y., Jin, R., Sojic, N., Jiang, D. & Chen, H.-Y. Y. Intracellular Wireless Analysis of Single Cells by Bipolar Electrochemiluminescence Confined in a Nanopipette. *Angew. Chemie - Int. Ed.* **59**, 10416–10420 (2020).
133. Sanjuan-Alberte, P. *et al.* Wireless Nanobioelectronics for Electrical Intracellular Sensing. *ACS Appl. Nano Mater.* **2**, 6397–6408 (2019).
134. Rolandi, M., Noy, A., Inal, S. & Rivnay, J. Advances in bioelectronics: Materials, devices, and translational applications. *APL Mater.* **9**, (2021).
135. Zhang, H. R., Wang, Y. Z., Zhao, W., Xu, J. J. & Chen, H. Y. Visual Color-Switch Electrochemiluminescence Biosensing of Cancer Cell Based on Multichannel Bipolar Electrode Chip. *Anal. Chem.* **88**, 2884–2890 (2016).
136. Li, H. *et al.* Spatially-resolved multicolor bipolar electrochemiluminescence. *Electrochem. commun.* **77**, 10–13 (2017).
137. Xu, W., Ma, C. & Bohn, P. W. Coupling of Independent Electrochemical Reactions and Fluorescence at Closed Bipolar Interdigitated Electrode Arrays. *ChemElectroChem* **3**, 422–428 (2016).
138. Scida, K. *et al.* Fluorescence-Based Observation of Transient Electrochemical and Electrokinetic Effects at Nanoconfined Bipolar

- Electrodes. *ACS Appl. Mater. Interfaces* **11**, 13777–13786 (2019).
139. Seo, M., Yeon, S. Y., Yun, J. & Chung, T. D. Nanoporous ITO implemented bipolar electrode sensor for enhanced electrochemiluminescence. *Electrochim. Acta* **314**, 89–95 (2019).
 140. Yuan, F. *et al.* Regenerable bipolar electrochemiluminescence device using glassy carbon bipolar electrode, stainless steel driving electrode and cold patch. *Electrochim. Acta* **262**, 182–186 (2018).
 141. Rahn, K. L., Rhoades, T. D. & Anand, R. K. Alternating Current Voltammetry at a Bipolar Electrode with Smartphone Luminescence Imaging for Point-of-Need Sensing. *ChemElectroChem* **7**, 1172–1181 (2020).
 142. Xu, W., Fu, K., Ma, C. & Bohn, P. W. Closed bipolar electrode-enabled dual-cell electrochromic detectors for chemical sensing. *Analyst* **141**, 6018–6024 (2016).
 143. Eßmann, V., Barwe, S., Masa, J. & Schuhmann, W. Bipolar Electrochemistry for Concurrently Evaluating the Stability of Anode and Cathode Electrocatalysts and the Overall Cell Performance during Long-Term Water Electrolysis. *Anal. Chem.* **88**, 8835–8840 (2016).
 144. Takano, S. *et al.* Liquid-junction-free system for substitutional stripping voltammetry using a closed bipolar electrode system. *Electrochem. commun.* **66**, 34–37 (2016).
 145. Zhang, J. D., Zhao, W. W., Xu, J. J. & Chen, H. Y. Electrochemical behaviors in closed bipolar system with three-electrode driving mode. *J. Electroanal. Chem.* **781**, 56–61 (2016).
 146. Zhang, L., Gupta, B., Goudeau, B., Mano, N. & Kuhn, A. Wireless Electromechanical Readout of Chemical Information. *J. Am. Chem. Soc.* **140**, 15501–15506 (2018).
 147. Assavapanumat, S. *et al.* Chiral platinum-polypyrrole hybrid films as efficient enantioselective actuators. *Chem. Commun.* **55**, 10956–10959 (2019).
 148. Arnaboldi, S. *et al.* Absolute Chiral Recognition with Hybrid Wireless Electrochemical Actuators. *Anal. Chem.* **92**, 10042–10047 (2020).
 149. Fosdick, S. E. & Crooks, R. M. Bipolar electrodes for rapid screening of electrocatalysts. *J. Am. Chem. Soc.* **134**, 863–866 (2012).

150. Fosdick, S. E., Berglund, S. P., Mullins, C. B. & Crooks, R. M. Parallel screening of electrocatalyst candidates using bipolar electrochemistry. *Anal. Chem.* **85**, 2493–2499 (2013).
151. Naser-Sadrabadi, A. & Zare, H. R. A highly-sensitive electrocatalytic measurement of nitrate ions in soil and different fruit vegetables at the surface of palladium nanoparticles modified DVD using the open bipolar system. *Microchem. J.* **148**, 206–213 (2019).
152. Crouch, G. M., Oh, C., Fu, K. & Bohn, P. W. Tunable optical metamaterial-based sensors enabled by closed bipolar electrochemistry. *Analyst* **144**, 6240–6246 (2019).
153. Zhang, X., Zhai, Q., Xu, L., Li, J. & Wang, E. Paper-based electrochemiluminescence bipolar conductivity sensing mechanism: A critical supplement for the bipolar system. *J. Electroanal. Chem.* **781**, 15–19 (2016).
154. Chen, L., Zhang, C. & Xing, D. Paper-based bipolar electrode-electrochemiluminescence (BPE-ECL) device with battery energy supply and smartphone read-out: A handheld ECL system for biochemical analysis at the point-of-care level. *Sensors Actuators B Chem.* **237**, 308–317 (2016).
155. Seamus Higson. *Analytical Chemistry*. (Oxford University Press, 2004).
156. Carvalho, P. M., Felício, M. R., Santos, N. C., Gonçalves, S. & Domingues, M. M. Application of light scattering techniques to nanoparticle characterization and development. *Front. Chem.* **6**, (2018).
157. Stetefeld, J., McKenna, S. A. & Patel, T. R. Dynamic light scattering: a practical guide and applications in biomedical sciences. *Biophys. Rev.* **8**, 409–427 (2016).
158. Thomas, R. *Practical Guide to ICP-MS. Practical Guide to ICP-MS* (CRC Press, 2008). doi:10.1201/9781420067873
159. Goodhew, P. J., Humphreys, J. & Humphreys, J. *Electron Microscopy and Analysis. Electron Microscopy and Analysis* (CRC Press, 2000). doi:10.1201/9781482289343
160. Vernon-Parry, K. D. Scanning electron microscopy: An introduction. *III-Vs Rev.* **13**, 40–44 (2000).
161. Schatten, H. The role of scanning electron microscopy in cell and

- molecular biology: Sem basics, past accomplishments, and new frontiers. in *Scanning Electron Microscopy for the Life Sciences* **9780521195**, 1–15 (2010).
162. Vernon-Parry, K. D. TEM: an introduction. *III-Vs Rev.* **13**, 36–40 (2000).
 163. Gibney, S. *et al.* Toward nanobioelectronic medicine: Unlocking new applications using nanotechnology. *Wiley Interdisciplinary Reviews: Nanomedicine and Nanobiotechnology* **13**, (2021).
 164. Sochol, R. D. *et al.* 3D printed microfluidics and microelectronics. *Microelectron. Eng.* **189**, 52–68 (2018).
 165. Rogers, J. A. Electronics for the human body. *J. Am. Med. Assoc.* **313**, 561–562 (2015).
 166. Li, Q. *et al.* Cyborg Organoids: Implantation of Nanoelectronics via Organogenesis for Tissue-Wide Electrophysiology. *Nano Lett.* **19**, 5781–5789 (2019).
 167. Hermanson, K. D., Lumsdon, S. O., Williams, J. P., Kaler, E. W. & Velez, O. D. Dielectrophoretic assembly of electrically functional microwires from nanoparticle suspensions. *Science (80-.)*. **294**, 1082–1086 (2001).
 168. Yuan, Y. J., Andrews, M. K. & Marlow, B. K. Chaining and dendrite formation of gold particles. *Appl. Phys. Lett.* **85**, 130–132 (2004).
 169. Lumsdon, S. O. & Scott, D. M. Assembly of colloidal particles into microwires using an alternating electric field. *Langmuir* **21**, 4874–4880 (2005).
 170. Huang, Y., Duan, X., Wei, Q. & Lieber, C. M. Directed assembly of one-dimensional nanostructures into functional networks. *Science (80-.)*. **291**, 630–633 (2001).
 171. Curtis, C. L., Ritchie, J. E. & Sailor, M. J. Fabrication of conducting polymer interconnects. *Science (80-.)*. **262**, 2014–2016 (1993).
 172. Cheng, C., Gonela, R. K., Gu, Q. & Haynie, D. T. Self-assembly of metallic nanowires from aqueous solution. *Nano Lett.* **5**, 175–178 (2005).
 173. Ranjan, N., Vinzelberg, H. & Mertig, M. Growing one-dimensional metallic nanowires by dielectrophoresis. *Small* **2**, 1490–1496 (2006).
 174. Ranjan, N., Mertig, M., Cuniberti, G. & Pompe, W. Dielectrophoretic growth of metallic nanowires and microwires: Theory and experiments.

- Langmuir* **26**, 552–559 (2010).
175. Kawasaki, J. K. & Arnold, C. B. Synthesis of platinum dendrites and nanowires via directed electrochemical nanowire assembly. *Nano Lett.* **11**, 781–785 (2011).
 176. Nerowski, A., Opitz, J., Baraban, L. & Cuniberti, G. Bottom-up synthesis of ultrathin straight platinum nanowires: Electric field impact. *Nano Res.* **6**, 303–311 (2013).
 177. Thapa, P. S. *et al.* Directional growth of polypyrrole and polythiophene wires. *Appl. Phys. Lett.* **94**, (2009).
 178. He, Y. *et al.* A Tripropylene Glycol Diacrylate-based Polymeric Support Ink for Material Jetting. *Addit. Manuf.* **16**, 153–161 (2017).
 179. Kamyshny, A., Steinke, J. & Magdassi, S. Metal-based Inkjet Inks for Printed Electronics. *Open Appl. Phys. J.* **4**, 19–36 (2011).
 180. Abbas, A. & Bajwa, I. Inkjet Printing of Ag Nanoparticles using Dimatix Inkjet Printer, No 1. (2017).
 181. Chuang, M. Y. & Chuang, M.-Y. *Inkjet Printing of Ag Nanoparticles using Dimatix Inkjet Printer, No 2.* (2017).
 182. Fricker, H. S. Why does charge concentrate on points? *Phys. Educ.* **24**, 157–161 (1989).
 183. Cogan, S. F., Ludwig, K. A., Welle, C. G. & Takmakov, P. Tissue damage thresholds during therapeutic electrical stimulation. *J. Neural Eng.* **13**, (2016).
 184. Costa, E. C. *et al.* 3D tumor spheroids: an overview on the tools and techniques used for their analysis. *Biotechnol. Adv.* **34**, 1427–1441 (2016).
 185. McNeil, S. E. Nanoparticle therapeutics: A personal perspective. *Wiley Interdiscip. Rev. Nanomedicine Nanobiotechnology* **1**, 264–271 (2009).
 186. Amreddy, N. *et al.* Recent Advances in Nanoparticle-Based Cancer Drug and Gene Delivery. in *Advances in Cancer Research* **137**, 115–170 (Adv Cancer Res, 2018).
 187. Yao, Y. *et al.* Nanoparticle-Based Drug Delivery in Cancer Therapy and Its Role in Overcoming Drug Resistance. *Front. Mol. Biosci.* **7**, (2020).

188. Toy, R., Bauer, L., Hoimes, C., Ghaghada, K. B. & Karathanasis, E. Targeted nanotechnology for cancer imaging. *Adv. Drug Deliv. Rev.* **76**, 79–97 (2014).
189. Vines, J. B., Yoon, J.-H., Ryu, N.-E., Lim, D.-J. & Park, H. Gold Nanoparticles for Photothermal Cancer Therapy. *Front. Chem.* **7**, (2019).
190. Davis, M. E., Chen, Z. & Shin, D. M. Nanoparticle therapeutics: An emerging treatment modality for cancer. *Nature Reviews Drug Discovery* **7**, 771–782 (2008).
191. Lasa-Saracibar, B., Estella-Hermoso De Mendoza, A., Guada, M., Dios-Vieitez, C. & Blanco-Prieto, M. J. Lipid nanoparticles for cancer therapy: State of the art and future prospects. *Expert Opinion on Drug Delivery* **9**, 1245–1261 (2012).
192. Jain, S., Hirst, D. G. & O’Sullivan, J. M. Gold nanoparticles as novel agents for cancer therapy. *Br. J. Radiol.* **85**, 101–113 (2012).
193. Wu, M. & Huang, S. Magnetic nanoparticles in cancer diagnosis, drug delivery and treatment (Review). *Mol. Clin. Oncol.* **7**, 738–746 (2017).
194. Liu, C. M. *et al.* Cancer cell membrane-cloaked mesoporous silica nanoparticles with a pH-sensitive gatekeeper for cancer treatment. *Colloids Surfaces B Biointerfaces* **175**, 477–486 (2019).
195. Hicks, J. M. *et al.* Electric Field Induced Biomimetic Transmembrane Electron Transport Using Carbon Nanotube Porins. *Small* **17**, 2102517 (2021).
196. Connor, E. E., Mwamuka, J., Gole, A., Murphy, C. J. & Wyatt, M. D. Gold nanoparticles are taken up by human cells but do not cause acute cytotoxicity. *Small* **1**, 325–327 (2005).
197. Balint, R., Cassidy, N. J. & Cartmell, S. H. Conductive polymers: Towards a smart biomaterial for tissue engineering. *Acta Biomaterialia* **10**, 2341–2353 (2014).
198. Dallet, L., Stanicki, D., Voisin, P., Miraux, S. & Ribot, E. J. Micron-sized iron oxide particles for both MRI cell tracking and magnetic fluid hyperthermia treatment. *Sci. Rep.* **11**, (2021).
199. Hadji, H. & Bouchemal, K. Effect of micro- and nanoparticle shape on biological processes. *J. Control. Release* **342**, 93–110 (2022).
200. Luo, X. *et al.* Leakage-free polypyrrole-Au nanostructures for combined

- Raman detection and photothermal cancer therapy. *J. Mater. Chem. B* **5**, 7949–7962 (2017).
201. Shao, Q. *et al.* Electrochemical and spectroscopic studies on the conformational structure of hemoglobin assembled on gold nanoparticles. *J. Phys. Chem. B* **115**, 8627–8637 (2011).
 202. He, Y. Q., Liu, S. P., Kong, L. & Liu, Z. F. A study on the sizes and concentrations of gold nanoparticles by spectra of absorption, resonance Rayleigh scattering and resonance non-linear scattering. *Spectrochim. Acta - Part A Mol. Biomol. Spectrosc.* **61**, 2861–2866 (2005).
 203. Fissan, H., Ristig, S., Kaminski, H., Asbach, C. & Epple, M. Comparison of different characterization methods for nanoparticle dispersions before and after aerosolization. *Anal. Methods* **6**, 7324–7334 (2014).
 204. De Jong, W. H. *et al.* Particle size-dependent organ distribution of gold nanoparticles after intravenous administration. *Biomaterials* **29**, 1912–1919 (2008).
 205. Othman, N., Talib, Z. A., Kassim, A., Shaari, A. H. & Liew, J. Y. C. Electrical Properties of Polypyrrole Conducting Polymer at Various Dopant Concentrations. *J. Fundam. Appl. Sci.* **5**, 29–33 (2009).
 206. Hong, J. Y., Yoon, H. & Jang, J. Kinetic study of the formation of polypyrrole nanoparticles in water-soluble polymer/metal cation systems: A light-scattering analysis. *Small* **6**, 679–686 (2010).
 207. Savage, D. T., Hilt, J. Z. & Dziubla, T. D. In vitro methods for assessing nanoparticle toxicity. in *Methods in Molecular Biology* **1894**, 1–29 (2019).
 208. Kim, S. *et al.* Cytotoxicity of, and innate immune response to, size-controlled polypyrrole nanoparticles in mammalian cells. *Biomaterials* **32**, 2342–2350 (2011).
 209. Vaitkuvienė, A. *et al.* Evaluation of cytotoxicity of polypyrrole nanoparticles synthesized by oxidative polymerization. *J. Hazard. Mater.* **250–251**, 167–174 (2013).
 210. Alkilany, A. M. & Murphy, C. J. Toxicity and cellular uptake of gold nanoparticles: What we have learned so far? *J. Nanoparticle Res.* **12**, 2313–2333 (2010).
 211. Christau, S., Moeller, T., Genzer, J., Koehler, R. & Von Klitzing, R. Salt-

- Induced Aggregation of Negatively Charged Gold Nanoparticles Confined in a Polymer Brush Matrix. *Macromolecules* **50**, 7333–7343 (2017).
212. Dickinson, E. J. F. & Compton, R. G. Diffuse double layer at nanoelectrodes. *J. Phys. Chem. C* **113**, 17585–17589 (2009).
213. Cabuzu, D., Cirja, A., Puiu, R. & Grumezescu, A. Biomedical Applications of Gold Nanoparticles. *Curr. Top. Med. Chem.* **15**, 1605–1613 (2015).
214. Huang, Z. B., Yin, G. F., Liao, X. M. & Gu, J. W. Conducting polypyrrole in tissue engineering applications. *Front. Mater. Sci.* **8**, 39–45 (2014).
215. Ramtin, A. *et al.* Cytotoxicity considerations and electrically tunable release of dexamethasone from polypyrrole for the treatment of back-of-the-eye conditions. *Drug Deliv. Transl. Res.* **6**, 793–799 (2016).
216. Williams, R. L. & Doherty, P. J. A preliminary assessment of poly(pyrrole) in nerve guide studies. *J. Mater. Sci. Mater. Med.* **5**, 429–433 (1994).
217. Chen, S. J. *et al.* Template synthesis of the polypyrrole tube and its bridging in vivo sciatic nerve regeneration. *J. Mater. Sci. Lett.* **19**, 2157–2159 (2000).
218. Wang, X. *et al.* Evaluation of biocompatibility of polypyrrole in vitro and in vivo. *J. Biomed. Mater. Res. - Part A* **68**, 411–422 (2004).
219. Kirson, E. D. *et al.* Alternating electric fields arrest cell proliferation in animal tumor models and human brain tumors. *Proc. Natl. Acad. Sci. U. S. A.* **104**, 10152–10157 (2007).
220. Olofsson, P. S. & Tracey, K. J. Bioelectronic medicine: technology targeting molecular mechanisms for therapy. *J. Intern. Med.* **282**, 3–4 (2017).
221. Bradley, J. C. *et al.* Creating electrical contacts between metal particles using directed electrochemical growth. *Nature* **389**, 268–271 (1997).
222. Loget, G. & Kuhn, A. Electric field-induced chemical locomotion of conducting objects. *Nat. Commun.* **2**, (2011).
223. Perro, A., Reculosa, S., Ravaine, S., Bourgeat-Lami, E. & Duguet, E. Design and synthesis of Janus micro- and nanoparticles. *J. Mater. Chem.* **15**, 3745–3760 (2005).
224. Cao, J. T. *et al.* Immuno-Electrochemiluminescent Imaging of a Single Cell Based on Functional Nanoprobes of Heterogeneous

- Ru(bpy)₃²⁺@SiO₂/Au Nanoparticles. *Anal. Chem.* **90**, 10334–10339 (2018).
225. Han, C. *et al.* Observing Transient Bipolar Electrochemical Coupling on Single Nanoparticles Translocating through a Nanopore. *Langmuir* **35**, 7180–7190 (2019).
226. Kusakabe, K., Morooka, S. & Kato, Y. Current paths and electrolysis efficiency in bipolar packed-bed electrodes. *J. Chem. Eng. Japan* **15**, 45–50 (1982).
227. Kusakabe, K., Morooka, S. & Kato, Y. Equivalent resistances for current pathways in a bipolar packed-bed electrode cell. *J. Chem. Eng. Japan* **19**, 43–47 (1986).
228. Sudoh, M., Kodera, T., Hino, H. & Shimamura, H. Oxidative Degradation Rate of Phenol in An Undivided Bipolar Electrolyzer. *J. Chem. Eng. Japan* **21**, 536–538 (1988).
229. MacDonald, D. D. Reflections on the history of electrochemical impedance spectroscopy. *Electrochim. Acta* **51**, 1376–1388 (2006).
230. Epelboin, I., Keddam, M. & Takenouti, H. Use of impedance measurements for the determination of the instant rate of metal corrosion. *J. Appl. Electrochem.* **2**, 71–79 (1972).
231. Chen, Z., He, C., Yu, F. & Wang, Y. Study and application of electrochemical impedance spectroscopy for quickly evaluating the performance of coatings and predicting the failure time in the development of waterborne epoxy micaceous iron oxide coatings. *Int. J. Electrochem. Sci.* **12**, 2798–2812 (2017).
232. Loveday, D., Peterspm, P. & Rodgers, B. Evaluation of organic coatings with electrochemical impedance spectroscopy part 2: Application of EIS to coatings. *CoatingsTech* **1**, 88–93 (2004).
233. Gomadam, P. M. & Weidner, J. W. Analysis of electrochemical impedance spectroscopy in proton exchange membrane fuel cells. *Int. J. Energy Res.* **29**, 1133–1151 (2005).
234. He, Z. & Mansfeld, F. Exploring the use of electrochemical impedance spectroscopy (EIS) in microbial fuel cell studies. *Energy Environ. Sci.* **2**, 215–219 (2009).
235. Selman, J. R. & Lin, Y. P. Application of ac impedance in fuel cell research

- and development. *Electrochim. Acta* **38**, 2063–2073 (1993).
236. Blommaert, M. A., Vermaas, D. A., Izelaar, B., In't Veen, B. & Smith, W. A. Electrochemical impedance spectroscopy as a performance indicator of water dissociation in bipolar membranes. *J. Mater. Chem. A* **7**, 19060–19069 (2019).
237. Randviir, E. P. & Banks, C. E. Electrochemical impedance spectroscopy: An overview of bioanalytical applications. *Anal. Methods* **5**, 1098–1115 (2013).
238. Kafka, J., Pänke, O., Abendroth, B. & Lisdat, F. A label-free DNA sensor based on impedance spectroscopy. *Electrochim. Acta* **53**, 7467–7474 (2008).
239. Teengam, P. *et al.* Electrochemical impedance-based DNA sensor using pyrrolidinyl peptide nucleic acids for tuberculosis detection. *Anal. Chim. Acta* **1044**, 102–109 (2018).
240. Bhardwaj, P., Rai, D. V., Garg, M. L. & Mohanty, B. P. Potential of electrical impedance spectroscopy to differentiate between healthy and osteopenic bone. *Clin. Biomech.* **57**, 81–88 (2018).
241. Yun, J. *et al.* Electrochemical impedance spectroscopy with interdigitated electrodes at the end of hypodermic needle for depth profiling of biotissues. *Sensors Actuators, B Chem.* **237**, 984–991 (2016).
242. Yun, J., Hong, Y. T., Hong, K. H. & Lee, J. H. Ex vivo identification of thyroid cancer tissue using electrical impedance spectroscopy on a needle. *Sensors Actuators, B Chem.* **261**, 537–544 (2018).
243. Sun, T. & Morgan, H. Single-cell microfluidic Impedance cytometry: A review. *Microfluidics and Nanofluidics* **8**, 423–443 (2010).
244. Lukic, S. & Wegener, J. Impedimetric Monitoring of Cell-Based Assays. in *eLS* 1–8 (2015). doi:10.1002/9780470015902.a0025710
245. Jiang, Y. *et al.* The Interplay of Size and Surface Functionality on the Cellular Uptake of Sub-10 nm Gold Nanoparticles. *ACS Nano* **9**, 9986–9993 (2015).
246. Ribeiro, M. *et al.* Human Breast Cancer Cells Demonstrate Electrical Excitability. *Front. Neurosci.* **14**, (2020).
247. Sanjuan-Alberte, P. & Rawson, F. J. Engineering the spark into bioelectronic medicine. *Therapeutic Delivery* **10**, 139–142 (2019).

248. Oh, N. & Park, J. H. Endocytosis and exocytosis of nanoparticles in mammalian cells. *Int. J. Nanomedicine* **9**, 51 (2014).
249. Lutton, J. D., Abraham, N. G., Drummond, G. S., Levere, R. D. & Kappas, A. Zinc porphyrins: Potent inhibitors of hematopoieses in animal and human bone marrow. *Proc. Natl. Acad. Sci. U. S. A.* **94**, 1432–1436 (1997).
250. Mioc, M. *et al.* The cytotoxic effects of betulin-conjugated gold nanoparticles as stable formulations in normal and melanoma cells. *Front. Pharmacol.* **9**, (2018).
251. Ostovari, M., Riahi Alam, N., Zabihzadeh, M., Gharib-Vand, M. M. & Hoseini-Ghahfarokhi, M. The effect of gold nanoparticles on electrical impedance of tissue on low frequency ranges. *J. Biomed. Phys. Eng.* **8**, 241–250 (2018).
252. Wegener, J., Keese, C. R. & Giaever, I. Electric cell-substrate impedance sensing (ECIS) as a noninvasive means to monitor the kinetics of cell spreading to artificial surfaces. *Exp. Cell Res.* **259**, 158–166 (2000).
253. Hirschorn, B., Tribollet, B. & Orazem, M. E. On Selection of the Perturbation Amplitude Required to Avoid Nonlinear Effects in Impedance Measurements. *Isr. J. Chem.* **48**, 133–142 (2008).
254. Masturah binti Fakhruddin, S., Ino, K., Inoue, K. Y., Nashimoto, Y. & Shiku, H. Bipolar Electrode-based Electrochromic Devices for Analytical Applications – a Review. *Electroanalysis* **33**, 1–16 (2021).
255. Adams, J. U. & Fairman, J. E. What is a Cell? What are the Essential Components? in *Essential cell biology* (ed. O'Connor, C.) 1–10 (NPG Education, 2010).
256. Yang, Y., Yang, X., Tan, Y. & Yuan, Q. Recent progress in flexible and wearable bio-electronics based on nanomaterials. *Nano Research* **10**, 1560–1583 (2017).
257. Cho, Y. H., Park, Y. G., Kim, S. & Park, J. U. 3D Electrodes for Bioelectronics. *Adv. Mater.* (2021). doi:10.1002/adma.202005805
258. Yun, M. *et al.* Electrochemically grown wires for individually addressable sensor arrays. *Nano Lett.* **4**, 419–422 (2004).
259. Shen, P., Yue, Y., Zheng, J. & Park, Y. *Caenorhabditis elegans*: A Convenient In Vivo Model for Assessing the Impact of Food Bioactive

- Compounds on Obesity, Aging, and Alzheimer's Disease. *Annu. Rev. Food Sci. Technol.* **9**, 1–22 (2018).
260. Stiernagle, T. Maintenance of *C. elegans*. *WormBook : the online review of C. elegans biology* 1–11 (2006). doi:10.1895/wormbook.1.101.1
261. Hottinger, A. F., Pacheco, P. & Stupp, R. Tumor treating fields: a novel treatment modality and its use in brain tumors. *Neuro. Oncol.* **18**, 1338–1349 (2016).
262. Stupp, R. *et al.* Maintenance therapy with tumor-Treating fields plus temozolomide vs temozolomide alone for glioblastoma a randomized clinical trial. *J. Am. Med. Assoc.* **314**, 2535–2543 (2015).
263. Jo, Y. *et al.* Tumor treating fields (TTF) treatment enhances radiation-induced apoptosis in pancreatic cancer cells. *Int. J. Radiat. Biol.* **96**, 1528–1533 (2020).
264. O'Connell, D., Shen, V., Loudon, W. & Bota, D. A. First report of tumor treating fields use in combination with bevacizumab in a pediatric patient: a case report. *CNS Oncol.* **6**, 11–18 (2017).
265. Hart, F. X. & Palisano, J. R. Glycocalyx bending by an electric field increases cell motility. *Bioelectromagnetics* **38**, 482–493 (2017).